ABSTRACT

Title of Dissertation:	STUDY OF OPTICAL PROPERTIES AND CURRENT EMISSION PROCESSES OF GAS PHASE FIELD IONIZATION SOURCES
	Xuefeng Liu, Doctor of Philosophy, 2004
Dissertation Directed By:	Professor Jon Orloff Department of Electrical and Computer Engineering

Field emission ion sources are extremely important for producing high-resolution ion beams essential for several fields of research and especially for semiconductor manufacturing. Although most sources used are based on liquid metals they cannot produce beams of H, He or other noble gases, so that gas field ionization sources (GFIS) could have great utility for microscopy or applications sensitive to metal contamination (such as in-line processing). This dissertation explores the properties of the gas field ionization source with the goal of providing a resource to the ion column designer. For the first time a detailed treatment of the optics of the gas field ionization source is derived. Also, the first theoretical analysis of the current generation mechanism is presented that explains both the current-voltage characteristic and the total current of the GFIS with reasonable agreement with experiment.

The optical properties in the emission diode region are derived from the ray equation. For the evaluation of the spherical and chromatic aberrations, two new aberration integrals are derived, which are applicable to the diode region and are appropriate for numerical calculations. The results show that, regarding the aberration

coefficients, essential differences exist between the field ionization and field electron emission.

The virtual source size is evaluated in two ways. First, by the algorithm of addition in quadrature (A.I.Q.) of the contributions from the Gaussian source size, the spherical and chromatic aberrations, and the diffraction effect. The dependence of the virtual source size on the emitter radius, the beam limiting aperture and the tip temperature are analyzed. As an alternative, the method of direct ray tracing is used, taking into account the energy distribution of ions. The results from these two methods are compared.

The current emission process of GFIS is studied using a relatively simple model based on the mechanism of gas material supply into the ionization zone. Although a complete solution from the first principle was not possible due to the complexity of the gas-surface interactions, the results obtained agree reasonably well with experimental values both in magnitude and in the shape of the current-voltage characteristic.

A STUDY OF OPTICAL PROPERTIES AND CURRENT EMISSION
PROCESSES OF GAS PHASE FIELD IONIZATION SOURCES

By

Xuefeng Liu

Dissertation submitted to the Faculty of the Graduate School of the
University of Maryland, College Park, in partial fulfillment
of the requirements for the degree of
Doctor of Philosophy
2004

Advisory Committee:
Professor Jon Orloff, Advisor / Chair
Professor John Melngailis
Professor Patrick O'Shea
Professor Mario Dagenais
Professor Edward Redish

Dedication

To my parents

Acknowledgements

First, I would like to thank my advisor, Professor Jon Orloff, for his great support and enormous enthusiasm in guiding me through the study of my dissertation and carefully reviewing the draft, and for his great suggestions in the progress. He is the best advisor as well as a best friend one could have. Without his continuing encouragement, this work would definitely not be as it appears today.

I am grateful to Mr. John Barry for his technical assistance in the lab of Ion Beam Lithography, and to Mr. Nolan Ballew for his great help in the machine shop. Also, thanks to Mr. Edward Condon for his support in computer resources.

I am indebted to Professor John Melngailis, Professor Patrick O'Shea, Professor Mario Dagenais and Professor Edward Redish for their patient review of the thesis and kind service as the committee members.

Thanks to all my colleagues whose names I missed above but ever helped me one way or another.

Last but not least, I would like to thank my wife, Xiaorui, for her heart-warming love, whose mere existence gives me the strength to proceed.

Table Of Contents

List of Tables

List of Symbols

A   magnetic vector potential (Equation (2.6))

C_{ch} chromatic aberration coefficient for the emission diode region referred to the image plane (Equation (2.35), (2.36), Table (2.6))

C_{si} spherical aberration coefficient for the emission diode region referred to the image plane (Equation (2.40), (2.41), Table (2.5))

$D(x)$ electron tunneling probability (Chapter 3)

E   electric field intensity

E_a electric field intensity at the emitter apex (Chapter 2 and Chapter 3)

E_r the radial component (in spherical coordinates) of the electric field strength (Chapter 2 and Chapter 3)

E_θ the angular component (in spherical coordinates) of the electric field strength (Chapter 2 and Chapter 3)

E_ρ the radial component (in cylindrical coordinates) of the electric field strength (Section 2.3.3.3)

E_z the axial component (in cylindrical coordinates) of the electric field strength (Section 2.3.3.3)

f focal length of the emission diode region (Equation (2.17) and (2.21))

$f_E(x)$ energy distribution (Section 2.3.3.1)

$F(f)$ spatial frequency response (Equation (2.70))

F_r the radial component (in spherical coordinates) of the dipole force on a gas molecule (Section 3.1)

F_θ the angular component (in spherical coordinates) of the dipole force on a gas molecule (Section 3.1)

$g(z)$ paraxial ray solution (Section 2.3.1)

h Planck's constant (Equation (2.42))

$h(z)$ paraxial ray solution (Section 2.3.1)

h_c average hopping height of gas molecule (Equation (3.27) and (3.28))

i emission current (Chapter 3)

I ionization potential energy

J current density distribution (Section 2.3.3.2 and 2.3.3.4)

k Boltzmann constant (Chapter 3)

k_d diffusion rate constant (Section 3.2.2)

k_i ionization rate constant (Section 3.2.2)

K_θ $K_\theta = \tan\alpha/\tan\theta$ (Section 2.3.1.2, 2.3.2 and 2.3.3)

KE_c kinetic energy of a gas molecule with maximum hopping height equal to x_c (Section 3.2)

KE_e initial kinetic energy of electron (Equation (2.27), (2.28) and (2.29))

KE_i initial kinetic energy of ion (Equation (2.23))

m ion mass

M linear magnification of the emission diode region (Chapter 2)

M_A Angular magnification of the emission diode region (Equation (2.17))

n the cone index (Chapter 2 and Chapter 3)

n_{eff} effective gas density of gas molecules (Equation (3.29))

n_f the parameter describing the electric field distribution near emitter (Equation (2.56), Section 3.2)

n_g gas density (Chapter 3)

P_g gas pressure (Chapter 3)

q charge of ion

r_a the distance from the SOC core center to the emitter apex (Chapter 2 and 3)

r_G Gaussian image size of the emitter (Equation (2.48))

r_s virtual source size (Section 2.3.2 and 2.3.3)

r_{sp} radius of the circle of confusion due to the spherical aberration (Equation (2.49))

r_t the radius of curvature of the emitter apex (Equation (2.3))

R reduced ray coordinate (Section 2.3.1.2)

t_d flight time of a gas molecule between two consecutive collisions with the emitter (Equation (3.12) and (3.13))

T_g gas temperature (Chapter 3)

T_t emitter temperature (Chapter 2 and 3)

υ_0 velocity of a gas molecule rebound from emitter surface (Chapter 3)

υ_{th} mean thermal velocity of a gas molecule (Section 3.1, Section 3.2)

$\bar{\upsilon}_d$ mean drift velocity of gas molecule along the emitter shank (Chapter 3)

V electric potential (Section 2.2.2, Section 3.1)

V_{coll} collector voltage (Equation (2.60))

V_{ex} extraction voltage (Equation (2.43), (2.44))

w complex notation of the ray coordinate (Section 2.3.1.1 and 2.3.1.2)

x_c critical distance

x_m maximum hopping height of gas molecule at emitter surface (Equation (2.55) and pp80)

Y_{cy} gas supply function for cylindrical emitter (Chapter 3)

Y_{sp} gas supply function for spherical emitter (Chapter 3)

z_f the distance from the SOC core center to the extraction electrode (Chapter 2)

z_g axial position of the Gaussian image plane (Figure, Equation (2.44))

Z_{sh} gas flux into the ionization zone along the emitter shank (Chapter 3)

Z_{sp} gas flux into the ionization zone from space (Chapter 3)

ϕ work function

Φ electric potential (Equation (2.10))

Φ^* relativistically corrected electric potential (Equation (2.6))

θ initial emission polar angle of ion (Chapter 2); also as the polar angle of electron's trajectory (Equation (2.27) and (2.28))

θ_0 half polar angle of the emitter surface region to be imaged (Section 2.3.3.2 and 2.3.3.4); also as the exterior cone half angle of a conical emitter (Figure 3-2)

θ_c half angle of Taylor cone (Equation. (1.3))

η $\eta = (q/2m)^{1/2}$ (Equation (2.6), (2.8) and (2.9))

η_e charge to mass ratio of electron (Equation (2.29))

η_i charge to mass ratio of ion (Equation (2.29), Equation (2.68))

α convergence half angle of the ion beam at the Gaussian image plane (Chapter 2)

α_g polarizability of gas molecule (Section 2.3.3.1 and Chapter 3)

Ω solid angle of beam limiting aperture (Equation (2.44), (2.45), (2.51) and (2.52))

ε_0 permittivity of free space

γ the form factor in SOC model (Chapter 2 and 3); also as the surface tension (in Newton/m; Equation. (1.3))

$\psi(z)$ electric potential on axis (Section 2.3.1)

ν orbital frequency of tunneling electron in the gas molecule (Section 3.2.2)

Δ_e relative error in energy (Equation (2.29))

ΔV beam energy spread (Section 2.3.2)

Δw lens aberration in position (Section 2.3.1.3)

Δx_c half width of the ionization zone (Section 3.2.2)

Δ_θ relative error in position (Equation (2.28))

Chapter 1   Introduction

1.1   Review of The Thesis

This thesis consists of the following four chapters.

Chapter 1 Introduction

The motivation is explained, followed by a brief introduction of the history of high resolution focused ion beam (FIB) that focuses on the development of the gas phase ionization source (GFIS) and the liquid metal ion source (LMIS). It explains why the GFIS was abandoned in favor of the LMIS over the past twenty years and how GFIS is regaining attention.

Chapter 2 Theoretical Model of the GFIS

The emission diode region is introduced where the ionization and particle acceleration processes occur. The electric potential distribution in the emission diode region is one of the most important source characteristics, therefore methods for calculating the potential distribution are reviewed. Among those analytical approaches, we choose the Sphere-on-Orthogonal-Cone (SOC) model as the representation of the emitter geometry. The optical properties of the source are then computed based on the SOC model. The virtual source size of GFIS is derived in two alternative ways: addition in quadrature and direct ray tracing.

Chapter 3 Emission Current In GFIS

The mechanism of gas material supply to the emitter is discussed, which results in a relatively simple model for the emission current calculation. The simulation results are then presented for various emitter geometric and physical parameters.

Chapter 4 Conclusions

1.2   Motivation

High resolution FIB technology began in the early 1970's with the work on GFIS based instruments by Levi-Setti at the University of Chicago and by Orloff and Swanson at the Oregon Graduate Institute. The GFIS was abandoned in the late 1970's in favor of the Ga LMIS because the LMIS provides a higher angular intensity and more current overall than the GFIS and because the LMIS was easier to use—differential pumping and cryogenic environment were not required. Almost all FIB systems today are based on the Ga LMIS. In the 1980's, FIB proved to be an extremely valuable technology and had a major effect on the way semiconductor devices were designed, through the direct editing of circuits. It also proved to be critically important for failure analysis and for lithographic mask repair. More recently FIB has been used in academic laboratories for a wide range of research topics mostly having to do with MEMS, materials science and nanotechnology (the adoption of the technology by universities was slowed by the high cost, $300,000–$1,000,000, of the instruments).

The motivation for the present work is that the LMIS is limited to the production of metallic ions and there is a need for other ion species, in particular ions from noble gases, for applications such as EUV lithographic mask repair and applications that cannot risk contamination by Ga ions, such as in-line failure analysis in a semiconductor FAB. In addition, the imaging resolution of the FIB is limited by sample sputtering: a Ga based FIB is limited to ~5 nm imaging resolution even if the beam is focused to a smaller spot (the reason is that fine structure is destroyed before enough information can be gathered from the specimen to form a reliable image). For high resolution ion microscopy it would be useful to have light-weight ions, such as H or He ions, and a nanometer sized beam of

these ions can only be produced by a GFIS based FIB. This would be an interesting application to complement high resolution electron microscopy since the contrast mechanism of image formation is quite different for electrons and ions.

In order to be able to design a GFIS based FIB effectively, it is necessary to understand the optical properties of the GFIS. While experimental studies of this source were made many years ago, this is the first systematic theoretical study of the source optical properties that has been undertaken. In addition, a fundamental property of the source, the current-voltage characteristic, has been calculated from first principles and for the first time an accurate prediction of this property has been made. The information in this thesis and the methods used are meant to be employed by an FIB optical designer.

1.3   Review Of History Of High Resolution FIB

High resolution FIB technology based on field ionization has allowed a 2~3 orders of magnitude improvement in resolution and current density over conventional technologies and has had a major impact on the semiconductor industry. The success of FIB depends largely on the use of high brightness ion sources. The most widely used ion source in FIB is the LMIS; although the first source used in FIB, the GFIS is rarely used at present. Both are referred to as point ion sources. LMIS has the advantages of high current angular intensity (~20μA/sr at modest current), stability and ease of use. The FIB systems employing LMIS have found applications since the mid 80's in extensive areas such as lithographic mask repair, TEM specimen preparation, failure analysis, secondary ion mass spectrometry and semiconductor device re-wiring (in the design stage). The GFIS, while not as popular in FIB as the LMIS, is invaluable for high-resolution microscopy. In addition, the unique properties of GFIS may prove to be of great

3

importance for specialized applications, e.g. non-metallic ion sputtering, proton-induced x-ray emission analysis (PIXE), high-resolution microscopy and applications where ion damage or sputtering must be minimized.

1.3.1 The Gas Field Ionization Source

Although it has long been realized that a hydrogen atom in an electric field has a finite probability to be ionized by tunneling[1], for many years this phenomenon was inaccessible experimentally due to the difficulty of generating and managing the extremely high electric field required. The observation of field ionization was first made by Mü ller[2, 3, 4] with his invention of field ion microscope (FIM). By admitting H_2 at a low pressure (~10^3 torr) to a field emission apparatus (see Figure 1-1) and applying high positive voltage to a sharp metallic tip, he obtained a faint but highly resolved image of the tip surface.

With the development of vacuum technology and cryogenic techniques, the FIM is capable of imaging the field emitter surface on the atomic level and has since become a powerful analytical tool for studying surface processes. Although field ionization is closely related to field electron emission, in which an electron is extracted from the metal surface by the applied high electric field, the intrinsic resolution of FIM (2–3$\mathring{A}$) is about 10 times higher than that of the field emission microscope (FEM, ~25$\mathring{A}$) because the latter suffers from the lateral velocity spread of the emitted electrons[5] and, to a lesser extent, because the diffraction effect is more severe in FEM due to the longer wavelength of electrons than ions.

In the most simplified form, a FIM consists of an anode which is basically a sharpened needle—called the field emitter—made from the metallic specimen to be

analyzed, and a closely placed grounded counter electrode. The field emitter typically has an end radius of ~0.1μm. In practice, such a sharp emitter can be obtained from a thin wire through use of the electro-polishing technique[6] followed by thermal anneal and field evaporation[7]—a process in which a surface metal atom located above the average emitter surface is pulled out of the surface by high electric field (>5V/Å)—leaving an atomically smooth end-form. By applying high positive voltage (~10kV) to the emitter relative to the ground, an electric field of around 2-5V/Å is obtained at the emitter apex. An electric field of this magnitude will appreciably deform and lower the ionization potential barrier of the gas molecules, such as H_2, N_2 or He, introduced near the emitter so that an electron could tunnel through this barrier from the gas molecule into the emitter. The resulting ions are then directed toward the cathode in almost radial directions and thus form a highly magnified (~10^7) image of the emitter surface on the viewing screen (Figure 1-1). The magnification is approximately equal to the ratio between the emitter-to-viewing screen distance and the emitter apex radius. Figure 1-2 shows an emission pattern from a (111) oriented tungsten emitter[8], the individual surface atoms as well as the crystal structure of 3-fold symmetry at the emitter apex are clearly identified.
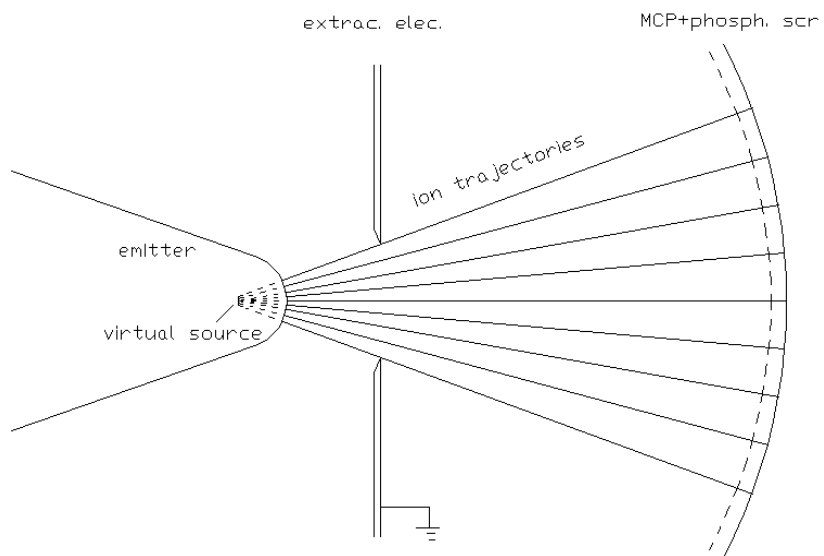
Figure 1-1 Schematic diagram of field ion microscope (not to scale)
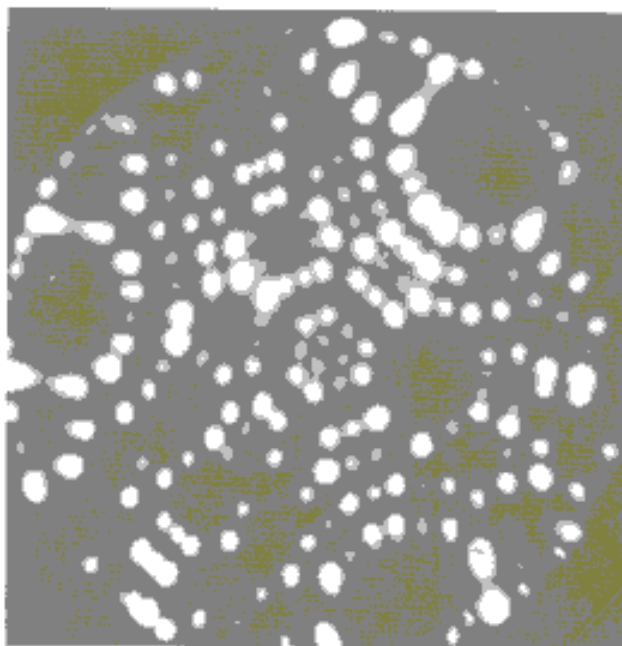
Figure 1-2 Emission pattern of a [111] oriented W emitter[8]
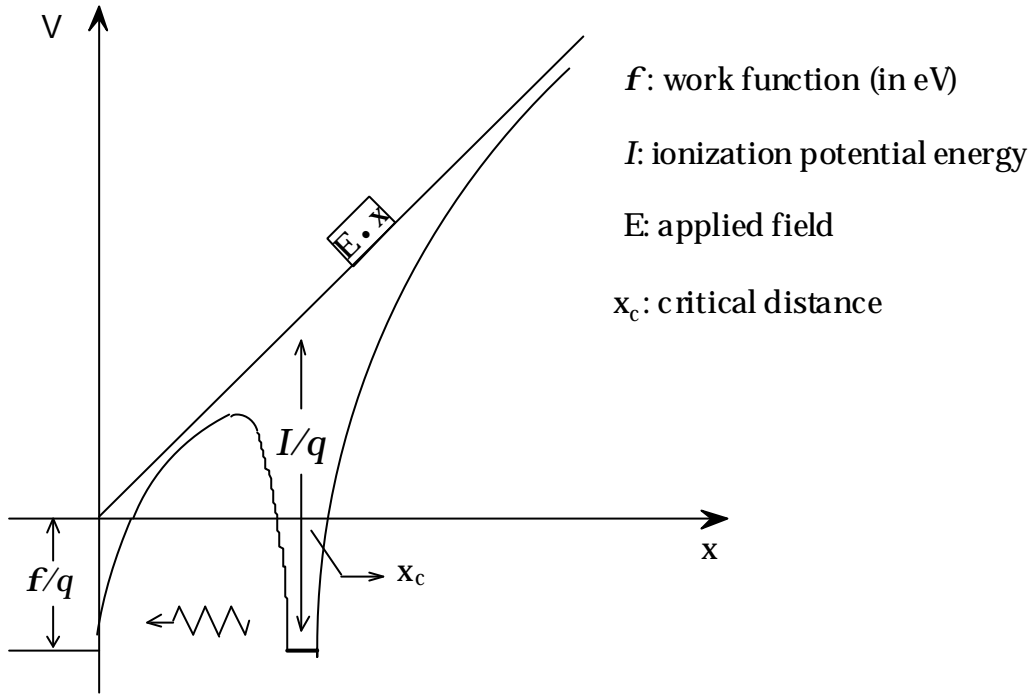
Figure 1-3 Potential diagram of an atom near a metal surface in electric field

The ion generation mechanism of GFIS is a purely quantum process which may be briefly described as follows (Figure 1-3).

A one-dimensional model of the electron potential of an atom near the metal surface in the presence of a uniform electric field E may be expressed as[3]

$$V(x) = -\frac{q}{4pe|x_i - x|} + Ex - \frac{q}{16pex} + \frac{q}{4pe(x_i + x)} \qquad (1.1)$$

where x and x_i represent the positions of the electron and the remaining ion core, respectively. The first term is the Coulomb interaction between the tunneling electron and the ion, the second term results from the applied electric field, and the last two terms represent the image effects of the electron and ion close to the metal surface.

Due to the external electric field E, the ionization potential barrier is deformed into a hump with finite height and width so that ionization may even occur at T = 0°K. When the atom moves closer to the metal surface, the potential barrier narrows. However, there exists a critical distance x_c below which ionization can not occur since the tunneling electron would otherwise fall below the Fermi level of the metal, which is prohibited by the Pauli exclusion principle. We can get an expression for x_c by neglecting the image effects that are usually quite small compared with the other terms

$$x_c = \frac{I - f}{qE} \qquad (1.2)$$

e.g. the ionization of helium (I = 24.5eV) before a tungsten surface (ϕ = 4.5eV) in the existence of E = 4.4V/Å ("best image field") gives x_c = 4.5Å. At this distance, the contribution of the image terms is only about 0.8eV.

Under these conditions, the tunneling probability of the electron can be calculated via the WKB approximation[9] where the potential barrier is modeled as a triangle with base x_c and height as determined by the superposition of the potential due to applied field and the original ionization potential. The tunneling probability depends exponentially on the electric field, which implies that the ionization occurs preferentially above the individual surface atoms where the local radius of curvature is small and the field is accordingly high. Further improvement of resolution can be accomplished by operating the FIM at cryogenic temperatures so as to reduce the lateral velocity spread of the imaging gas molecules.

The first efforts to apply the gas field ionization source in the microprobe applications were made by Levi-Setti *et al.*[10] and by Orloff and Swanson[11, 12, 13] in

the early 1970's. The motivation came from the fact that the GFIS is intrinsically a very bright ion source ($\sim 10^9 A \cdot sr^{-1} \cdot cm^{-2}$) with sub-nanometer source size. From the optical point of view, the emitted ions, when the tangents to their trajectories at the extraction electrode are projected back to the source, originate from a virtual image—called the virtual source—with typical size ~1nm located somewhere behind the emitter surface (Figure 1-1). Therefore, a small probe size can be achieved without having to resort to complicated optical systems.

Figure 1-4 shows a field ionization gun designed by Orloff and Swanson[14], where several important structures are worth noting: the two filament leads connecting power supply pass through a reservoir filled with liquid N_2, and the gas material is supplied through a long central tube in this reservoir in the vacuum chamber. By this means, the cryogenic condition for both the emitter and the imaging gas was achieved. This is important because it can minimize the energy spread of the ions as well as increase the emission current. Another interesting feature is the counter electrode very close to the emitter with a small hole in it. While serving as the extraction electrode, this structure will limit the pumping speed so that different pressures can be maintained between the source region (up to 10^{-2}–10^{-3}torr) and the region below the limiting aperture (10^{-5}–10^{-6}torr). The pressure in the source region is usually kept as high as possible to increase the supply of gas material to the emitter apex region where the ionization occurs, but it is limited by vacuum discharge effects and the ion-neutral interactions that results in the broadening of beam energy distribution. On the other hand, as low a pressure as possible is preferred in the optical column part so as to protect the ion beam from disturbance by the neutrals.
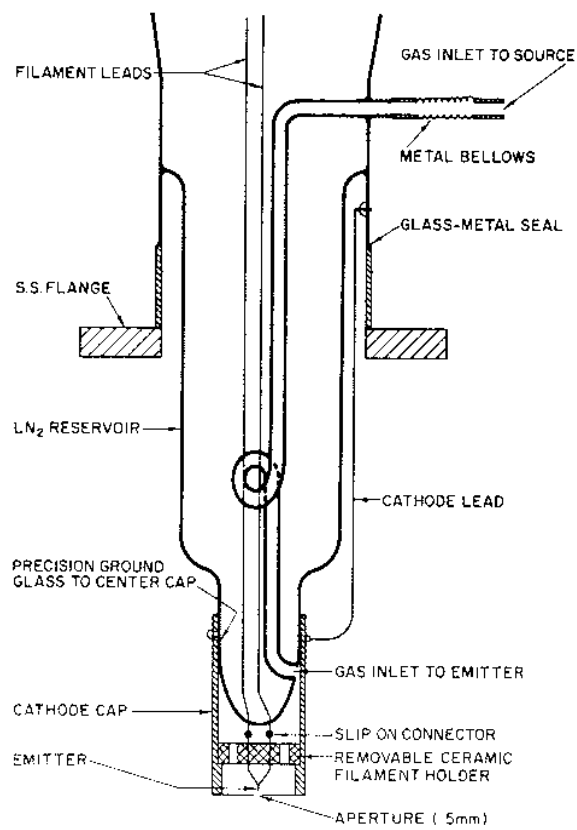
Figure 1-4 Practical gas phase field ionization source[14]

Although the virtual source size of GFIS is very small ~0.5nm, the actual emission occurs over a large area (~100nm in diameter) around the surface and the current density is typically ~10^2A·cm^{-2}. As a result, the space charge effects are negligible for GFIS and the energy spread is quite small ~1eV[15].

In practical FIB systems, the final probe size is often chosen to be on the order of 0.1μm, which is much larger than the virtual source size of GFIS. Therefore, instead of the source brightness, a more convenient quantity to characterize GFIS is the angular current intensity. The highest angular intensity obtained from conventional GFIS is 1μA/sr[16] with Ir emitter and H_2 at 77°K.

1.3.2 Liquid Metal Ion Source

The use of liquid metal ion source (LMIS) was first applied in FIB systems beginning in the late 70's [17, 18]. Now, it has become a most important and well-established tool in FIB technology.

The LMIS consists of a low melting point, low volatility metal film flowing via surface tension and electrostatic stress forces to the apex of a solid needle substrate with typical radius of several μm. Atoms are removed from the apex by field evaporation. The requirement of low melting temperature is to minimize the reaction between the liquid metal and the substrate, while low vapor pressure (typically $<10^{-7}$torr) is preferred so as to conserve the film supply and ensure a long lifetime of the source[19]. In cases where elements of high melting points and/or high vapor pressures are desired, e.g. B, As, P, Be and Si which are of particular interest to the semiconductor technology, liquid alloy ion sources (LAIS's) are used. Figure 1-5 shows a commercial LMIS emitter, where the

emitter substrate is connected to a spiral reservoir holding liquid Ga, which is spot-welded on a hairpin holder.

In order to understand the emission mechanism of the LMIS, it is advantageous to first review the electrostatic model of the LMIS, which was first studied by Sir G. Taylor[20]. He demonstrated that in a high electric field, under appropriate boundary conditions, there exists a unique surface geometry for the charged liquid. This geometry is an infinite cone—now known as a Taylor cone—with half angle of about 49.3°. He obtained this result by solving the equation that balances the electrostatic stress and the surface tension force over the cone surface, while neglecting the hydrostatic pressure difference across the curved surface:

$$\frac{1}{2}\varepsilon_0 E^2 = \frac{\gamma}{r} ctg\theta_c \tag{1.3}$$

where E is the applied electric field at the surface, γ is the surface tension, r is the radial distance measured from the apex of the Taylor cone and θ_c is the cone half angle. A special solution of (1.3) is given by

$$V(r,\theta) = V_0 + A \cdot P_{\frac{1}{2}}(\cos\theta) \cdot r^{1/2} \tag{1.4}$$

where $P_{1/2}(\cos\theta)$ is the Legendre function of order ½, V_0 is the potential of the cone surface and A is a constant to be determined by boundary conditions. The requirement that $V(r,\theta)$ is constant ($=V_0$) over the cone surface implies that $P_{1/2}(\cos\theta_c) = 0$ which gives $\theta_c = 49.3°$.
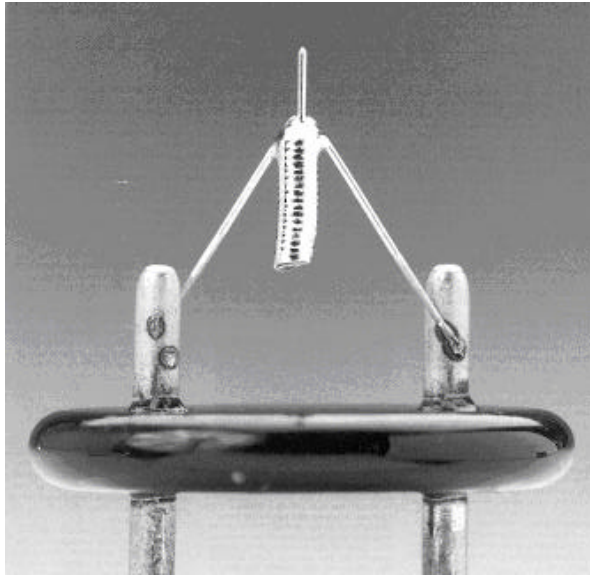
Figure 1-5 A commercial Ga LMIS (courtesy FEI Company)
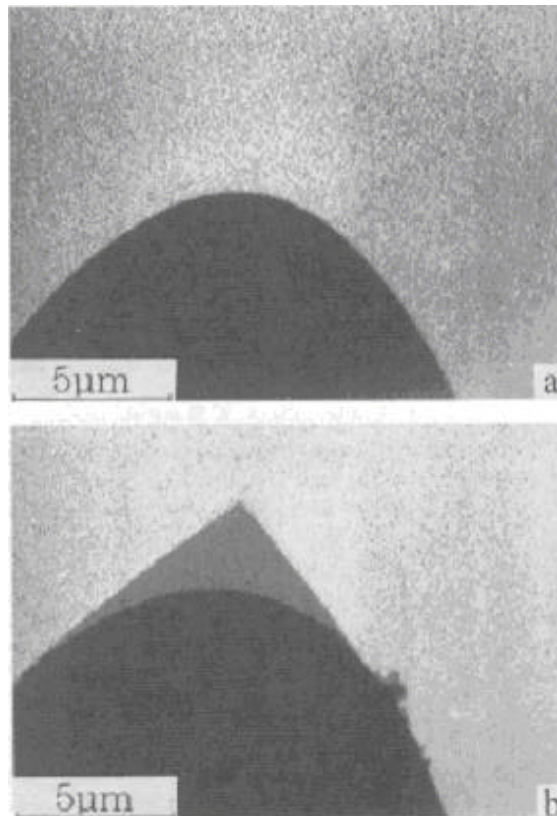
Figure 1-6 a) LMIS substrate; b) AuGe forming a Taylor cone[22]

A LMIS in operation can never really form a Taylor cone, however, since field evaporation of surface atoms will set in when the electric field approaches ~1V/Å. As a result, the Taylor cone is rounded off to an apex of diameter ~5nm[21]. Nevertheless, the SEM photographs of the frozen-in emitter as well as those taken in-situ [22, 23, 24] illustrated that the shape of LMIS at low currents is close to the Taylor cone (Figure 1-6).

The Taylor model did not take into account the fluid flow as is necessary to replace the loss of material from emission. In addition, due to the extremely small emission area of LMIS, the current density can be as high as $10^6 A/cm^2$, so space charge effects[25] play an important role, as opposed to the case of GFIS. At current $I > 10\mu A$, the space charge effects become such an important issue that it initially led to confusion in understanding the emission mechanism of LMIS[26, 27]—the field at the end of the rounded-off Taylor cone would not be high enough to allow field evaporation (FEV), yet field ionization (FI) was excluded from being a primary mechanism by careful analysis of electronic heating of emitter from the apex. In order to solve this problem, Kang and Swanson[28] postulated that a cylindrical protrusion ("jet") existed at the end of the Taylor cone due to the fluid flow and space charge effects. Kingham and Swanson later[29] developed this idea by taking the liquid metal as irrotational and viscosity-free. They incorporated a hydrodynamic term $\rho v^2/2$ in the balance equation, which represents the negative pressure in the flowing liquid, chose a likely shape for the emitter and calculated the field as was necessary to stabilize the LMIS. This field, which was obtained from the hydrodynamic perspective, was then compared with that obtained from the ion-emission point of view (taking into account the space charge). The procedure was continued iteratively until a self-consistent solution was found. The results, as were

confirmed by experiments[23, 29], demonstrated the existence of a jet-like protrusion at the end of Taylor cone, whose apex radius is several nm and whose length is tens of nanometers and increases with current.

The primary emission mechanism of LMIS is FEV[30, 31, 27] as was mentioned before. The FEV can be described as a field-enhanced thermally activated evaporation of surface atoms and subsequent ionization at the critical distance (section 1.3.1 Eqn. (1.2)). Some LMIS's also emit multiply charged ions through post-ionization—a field-evaporated ion is further ionized near the emitter[32]. At higher currents, there is an increasing contribution from the gas phase field ionization of the thermally evaporated atoms, as the emitter is heated by electron bombardment[33]. In addition, at high currents (typically >50μA), evaporation and ionization of clusters and droplets become noticeable[34].

The most important features of the LMIS include the source size, energy distribution, angular current intensity, source stability and lifetime.

As mentioned before, the emission area of LMIS is extremely small (~5nm) at modest current level. The strong space charge present at the emitter apex, however, dramatically increases the apparent source size to ~50nm at least.

Besides beam broadening, the space charge is also responsible for the broadening of ion energy distribution. This is reflected by the dependence of energy spread on the total current as well as the charge-to-mass ratio of ions[35]. The energy spread has a lower limit of about 5eV at low currents[36], and increases rapidly with the total current (to the power of 2/3) and the increasing mass-to-charge ratio. The physical reason is believed to be mainly due to the potential relaxation[37, 38], or Boersch effect whereby

the potential energy stored between closely spaced ions is converted to the kinetic energy as they travel. Moreover, at high currents, the energy distribution is also affected by the charge-exchange reactions[39] and increasing contribution from gas phase field ionization.

The angular current distribution is found to be quite broad, with typical width of 25°–30°[40]. The remarkable features of it are the extreme uniformity and a sharp fall-off at the edge. From the application point of view, the former is favorable in that it eases the requirement of source alignment.

The emission of the LMIS is very stable. The DC current level decreases but slowly with time as the result of the change of flow impedance. The physical processes affecting the flow impedance include the liquid-substrate reaction, the segregation of impurities on the surface, the material precipitates resulting from the change in source composition (for LAIS) and the sputtering of aperture material onto the LMIS[19, 41]. The latter process is the most important. The routine way to restore the normal condition of LMIS is to overvolt and heat the source so as to evaporate the impurities or remove them in the form of droplet emission. Moreover, the presence of space charge also helps to stabilize the current through potential relaxation and negative feedback on the local field[33].

The lifetime of various LMIS currently in use is ~2000μA·hr·cm^{3}[21]. The type shown in Figure 1-5 has a lifetime up to 6000μA·hrs.

Current FIB systems employing LMIS are capable of focusing 5pA–30nA current into 5nm–1μm spot size, with current density of several Acm^{-2}. Typical applications include scanning ion microscopy (SIM) where the ion beam is raster-scanned over the

target surface and various secondary particles can be collected to either obtain a surface contrast image or analyze the target chemical composition through use of secondary ion mass spectrometry (SIMS[42, 43, 44, 45]); lithographic mask repair where excessive material can be removed through ion beam sputtering[46, 47, 48] and clear defect can be repaired by FIB enhanced deposition with the use of suitable chemical gases[49, 21]; IC circuit repair or editing where electrical connections can be broken or created on a micrometer scale by appropriate removal or addition of conducting or non-conducting materials; and maskless ion implantation which is particularly suitable for accurately controlled device tailoring[50].

1.3.3 Supertip GFIS

From the perspective of FIB applications, the main impediment to the use of conventional GFIS is its small angular current intensity (~1μA/sr) compared with that of LMIS (20–40μA/sr). In order to improve this quantity, Hansen et.al[51, 52] developed a technique whereby ion bombardment with He$^+$ creates a damage around the emitter apex when operating in FE mode, and subsequent surface atom migration at elevated temperatures to the damaged cite creates a small hump of typically 10nm in diameter and several nm in height. Since the electric field at this local protrusion is higher than its neighboring regions, the ion emission is highly confined to this microscopic protuberance—called a supertip[53]. Besides, the distribution of electric field in the vicinity of supertip on top of a larger substrate is such that the lines of force bend considerably toward the emission axis. Accordingly, the angular divergence of emission is reduced dramatically, from ~30° down to ~1°[54]. The reason behind this can be inferred by noting that the ion trajectory is largely determined by the field within a

17

distance on the order of the emitter radius (~5nm for supertip). As a rough estimation, take the field of a spherical emitter

$$E = E_0 \left(\frac{r_0}{r} \right)^2 \qquad (1.5)$$

where E_0 and r_0 are the surface field and emitter radius, respectively. The ratio of the kinetic energy of an ion relative to its full kinetic energy at the extraction electrode, is given by $(1 - r_0/r)$, i.e. the ion would gain 90% of its full kinetic energy within $10r_0$.

The resulting angular ion current intensity from supertip GFIS can be as high as that obtained from LMIS, while maintaining the advantages of smaller source size and energy spread.

The supertip GFIS is still a subject under active investigation, mainly by the group of Kalbitzer at the Max-Planck Institute in Heidelberg[54, 55, 56], however the main difficulty in practical employment of supertip GFIS is, in addition to the operational complexities related to conventional GFIS, that it is extremely difficult—if not impossible—to control the location of damage caused by the ion bombardment, hence the position of the growth of supertip. The protrusion locates in an angular interval of $4° - 10°$ about the emitter apex[53], corresponding to a solid angle of 15–100msr, as compared with the limiting beam aperture of 0.05msr (for 1nA at 20μA/sr). This lack of control places a stringent requirement on the system alignment as well as the skill of operator. Moreover, the question of whether or not long term emission stability of supertip GFIS with various gases can be assured remains to be addressed.

1.4   Potential Advantages Of GFIS Compared To LMIS

The GFIS was abandoned in FIB applications in favor of LMIS mainly due to its greater operational complexity and lower angular current intensity. However, compared with the LMIS, the GFIS has several exclusive properties that may be of critical importance for certain applications: a much smaller intrinsic source size is available, which is to be covered in more detail in Chapter 2; the energy spread can be as low as 1eV, implying that the focused ion beam suffers less from the chromatic aberrations; and that noble gas ions can be generated as a supplement to the metallic ions from LMIS.

Besides the employment in FIM as a surface analysis means, it is thus conceivable that the GFIS is inherently a superior source to be used in scanning ion microscopy because the sputtering of sample is minimized using light ions.

It is known that the imaging resolution limit of SIM is determined by the destructive nature of ion beam[57, 58]. In order to resolve a structure on the sample with a given contrast, a human-eyes-discernible minimum signal-to-noise (S/N) ratio has to be achieved, which is S/N ~ 5[59]. Better images would require S/N ~ 20–25. In SIM, it is through collecting the induced secondary electrons (ISE) and/or ions (ISI) that the information about the sample is conveyed. Meanwhile, the sputtering of sample by the imaging ion beam also occurs in the form of induced secondary atoms (ISA). If a structure on the sample is too small, it would be destroyed by ion bombardment before enough secondary charged particles could be collected, hence the resolution limit. The highest resolution available with LMIS at present is around 5nm at S/N = 20, and higher ones are possible only at the cost of reducing the S/N which results in poor image quality. This situation may be changed by employing GFIS using lightweight gases such as H_2 or

He. Besides the fact that smaller beam spot is inherently available, it is also expected that the sputtering effect of light ions is smaller than the heavy metallic ones [60, 61]. In fact, theoretically[62], it is expected that the sputtering yield (atoms sputtered / incident ion) on Si by proton beam is only about 0.02–0.006 of that by Ga^+ beam at 10–50keV.

On the other hand, by changing to heavier gaseous ions such as Ar^+ and Kr^+, the GFIS might also be used for direct micromachining. But unlike the LMIS where contamination of the target by metallic ions is inevitable and undesirable for certain applications, this issue is minimized with GFIS where the noble elements can be easily annealed out.

Other potential applications of GFIS involve high-resolution proton-induced x-ray-emission or PIXE analysis, and particle-induced nuclear reactions. The PIXE is a multi-elemental, high sensitivity (~1ppm) analytical method[63] based on the fact that an energetic proton (several MeV) impinging on a sample atom will eject an inner-shell electron from the target, leaving a vacancy there, and the following transition of an electron from the outer-shell to the vacancy will generate x-ray emission whose frequency is characteristic of the element. A great advantage of PIXE combined with high-resolution FIB is that it allows a two-dimensional trace element mapping with minimum detectable concentration requirement[64]. Similar to PIXE, an element can be identified through the energy of nuclear reaction induced by the impingement of an energetic particle. While PIXE is more efficient in detecting heavy elements (Z > 11)[65], particle-induced nuclear reactions are more appropriate for identifying light ones (Z < 20)[64], and together they can provide analysis tools for a wide range of elements.

1.5   Technical Aspects Of GFIS Operation

From the technical point of view, two critical issues are involved for practical use of GFIS in FIB systems.

Firstly, before admitting the imaging gas, it is necessary to pump the source chamber to high vacuum ($<10^{-9}$ torr) and in some cases (e.g. with W emitter) to bake the system so as to minimize the emitter surface corrosion by water vapor[66] and other active residual gas species[67, 68], especially when imaging gases, such as H_2, of low ionization potentials are to be used because the emitter surface field would not be high enough to prevent the approach of reactive molecules. The field-promoted etching of the emitter surface would result in surface defects as well as change in the tip shape, which accordingly would change the electric field and emission characteristics or even, under extreme circumstances, destroy the emitter.

Secondly, source cooling is commonly required in order to achieve highest resolution and maximize the emission current. In general, this is accomplished by keeping a good thermal contact of the emitter filaments as well as the gas supply path with a cryostat filled with a cooling liquid with a low boiling point, such as liquid nitrogen, hydrogen and helium (Figure 1-4).

On the other hand, the imaging gas pressure in the source region can be as high as 10^{-2} torr, so that special care must be taken to prevent the tip from blowing out due to vacuum arc caused by degassing of the chamber walls, especially when non-bakable devices are installed (e.g. the viewing screen). The situation is worse with long-term source operation at cryogenic temperature because the gas density around the emitter depends exponentially on the reciprocal of temperature as a consequence of the dipole

attraction force on the gas molecule[2]. For long-term operation, periodic thermal-field processing technique[69] seems to be necessary whereby the tip is heated, in the presence of electric field, to a temperature below its melting point. In this way, surface roughness is smoothed by atom migration and surface contaminants are removed via desorption or field evaporation.

1.6   Present Work And Its Significance

In this thesis, the work is focused on the optical properties and current emission process of GFIS.

The Gaussian optical properties, such as the linear magnification, and the 3rd order geometrical and 1st order chromatic aberrations are evaluated via the paraxial ray equation and the aberration integrals. There exist several forms of the aberration integrals[70], which either involve the 4^{h} derivative of the potential or assume that the aperture plane is in field-free region. In this thesis, two alternative integrals for the spherical and chromatic aberration coefficients are presented based on the formula by Lencová *et al.*[71] for aberrations in both slope and position.

Among the optical properties, the virtual source size of GFIS is important both theoretically and practically. In FIB applications, it is desirable to have knowledge about the source size, which is to be imaged on the target, especially its dependence on the emitter geometry and extraction voltage, in order to find the optimal design of the optical column.

Wiesner and Everhart made a calculation of the virtual source size of the emitter in a field electron emission mode[72]. Their calculation was done by setting up and evaluating the equations of motion of the electrons to obtain the magnification, spherical

and chromatic aberrations, and then added these terms in quadrature to get the virtual source size, taking into account the diffraction effect.

The change to the ion emission mode, however, is nontrivial. Besides the fact that the diffraction effect is negligible for ions, an essential difference is that electrons are emitted right from the tip surface while the ions are generated in a small region beyond the critical distance above the emitter surface, whose width and hence the ion energy spread depend on the gas species and increase with the extraction voltage. In addition, it is well known that the algorithm of addition in quadrature, although commonly used to estimate the overall effect from individual contributions, lacks solid mathematical support[73] except in special cases (e.g. for Gaussian distribution).

In this thesis, besides the algorithm of addition in quadrature, the virtual source size of GFIS is obtained alternatively by numerically solving the equation of motion and calculating the trajectories of ions. The initial positions of the ions are set according to the energy distribution obtained with a one-dimensional model[74]. By assuming uniform current density in a small region around the emitter apex, we can then obtain the (relative) current density distribution in the virtual image plane.

The advantage of this method is that higher order aberrations are inherently included and that the uncertainty in the addition of individual terms is avoided.

The current emission process in GFIS is complicated in that it inevitably involves the interaction between the gas molecule and the emitter surface, which is not yet fully understood. It is well known that the supply of gas material into the ionization zone—a small region around the emitter apex where virtually all ionization events occur—plays the key role in current emission. Former attempts by Van Eekelen[75] and Iwasaki *et*

23

al.[76] made use of the supply function from the vacuum to the ionization zone to calculate the total current, while making explicit assumptions on the gas-surface interaction. Their calculations, however, neglected the effect of gas supply via the emitter shank, which is now believed to be the principal supply mechanism. Consequently, their results underestimated the total current, especially at large extraction voltages when the current emission is supply-limited.

In this thesis, a relatively simple model is presented based on the analysis of the supply mechanism. Although a complete solution from the first principle is absent, it is shown that the resulting I-V characteristic agrees reasonably well with the experiment, both in magnitude and in slope.

Chapter 2   Optical Properties Of The GFIS

In this chapter, the theoretical aspects of the GFIS are investigated in more detail, beginning with the introduction of the emission diode region as the environment for the study of the optical and physical source characteristics. Detailed information about the electric potential distribution is critical to the source analysis, and various methods involved are reviewed in section 2.2. Among all analytical models, the sphere-on-orthogonal-cone (SOC) model is found to well describe the geometry of thermally annealed emitters and is adopted in the following calculations. Section 2.3 is devoted to the problem of evaluating the source optical properties and leads to the calculation of virtual source size for various source configurations. A summary is presented in section 2.4.

2.1   Emission Diode Region

In a FIB optical system, the emission diode region is referred to as the region between the source and the extraction electrode. Its importance is reflected in two aspects:

i.   The beam characteristic as determined by the diode region would set an upper limit for the whole system performance because, in an aberration-free system the brightness is an invariant[77], and the existence of lens aberrations would cause the brightness to decrease, therefore limiting the final probe size and current intensity obtainable.

ii.   It determines the electric field near the emitter and so critically influences the physical processes regarding ion generation, e.g. the supply of impinging gas material to the emitter apex region, the gas-emitter surface interaction and current generation, and

the initial trajectories of the ions. Study of these physical processes, while important theoretically, is of great value in determining the optimal system design.

The research in all aforementioned areas, especially in evaluating the source optical properties, requires detailed information of electric field distribution. In GFIS, the difficulty of this problem comes mainly from two factors. The first one is due to the complicated geometric configuration of the diode region. In particular, a real emitter, as shown by various field ion micrographs, often exhibits facets around its apex, corresponding to the growth preference of certain crystallographic planes as a result of minimization of the surface free energy. Structures of this kind, plus the possible inclusion of a suppressor electrode, prevent us from getting an analytic solution of the potential distribution.

On the other hand, typical emitters have apex radii of ~0.1μm while the distance from the emitter to the extraction electrode is ~1mm or larger. Such an extreme difference in scale (up to 10^5) adds to the difficulty of numerically solving the Poisson's equation.

The following section therefore goes to the problem of calculating the potential distribution in the emission diode region.

2.2   Calculation Of Electric Potential In The Diode Region

2.2.1   Review Of Methods

The methods of attacking the electrostatic potential distribution problem can be generally put into two categories—analytical approach and numerical calculation.

Among the various analytical models, the spherical emitter model is certainly the simplest one where the field is proportional to r^{-2}. The main problem with it is that the emitter shank has been neglected. From the optical point of view, the presence of a conical shaped shank acts as a suppressor electrode so that the trajectories of charged particles are driven toward the axial direction, which is advantageous from the perspective of increasing the angular current intensity. Besides its effect on the optical properties, the emitter shank plays a key role in the current emission process, as will be discussed in the next chapter. Nevertheless, the spherical model has been used in a point-cathode study, at least in the immediate region around the emitter[78], so as to obtain an estimation of the source properties.

Other models, which incorporate the emitter shank, include the paraboloidal, hyperboloidal and SOC emitters. Of these, the SOC model is considered the most successful in that it closely approximates the topography of thermally annealed emitters by adjusting a couple of parameters, and has been used in the study of field emission cathode[72] and in trajectory calculations in the LMIS[79]. It is thus the model adopted in this thesis. The paraboloidal and hyperboloidal models, though could be used alone, are often employed in combination with the spherical model to represent the region far away from the emitter, or serve as the substrate of supertips[56].

There is no need to mention that the number of analytical solutions is highly limited. In addition, the space charge effect can sometime be important, e.g. in dealing with the LMIS, and must be included in the calculation. Since the advent of high speed computers, various numerical techniques have been developed, including the finite difference method (FDM)[70], the finite element method (FEM)[80, 81] and the charge density method (CDM).

In FDM, the region of interest is covered with a regular grid (usually a rectangular mesh) of points. The Laplace's equation is then put into a finite difference form which associates the potential on each grid point to its neighbors. The resulting set of equations is then solved to find the potential distribution. Kang *et al.*[82] proposed a spherical-coordinate-with-increasing-mesh (SCWIM) model, which is a modified version of FDM, where the spherical coordinates are used and the radial mesh size increases with radius. In this way, it was shown that the difficulty from the extreme difference in scale can be effectively overcome.

The FEM algorithm provides an alternative approach based on the use of finely divided mesh. In each mesh cell—called the finite element—the potential is assumed to be either a linear (in first-order FEM) or quadratic function (in second-order FEM) of the grid points. The potential distribution is then obtained by minimizing a proper variational functional (commonly the field energy).

The CDM is a special case of the general boundary element methods[70]. Instead of directly calculating the potential distribution, this method aims at finding the distribution of charge density on the involving electrodes, in correspondence to the

applied voltage configuration, and the potential in space can then be computed from Coulomb's law by an integration of the charge density distribution on these electrodes.

2.2.2 SOC Model

If the emitter as well as the extraction electrode is chosen to coincide with equipotentials generated by a conducting Cone with an Orthogonal Sphere at the end—called the core of the system, Laplace's equation can be solved analytically in spherical coordinates to yield[83]:

$$V(r,\boldsymbol{q}) = V_0 \left(\frac{r_a}{z_f}\right)^n \left[1 - \boldsymbol{g}^{-2n-1} - \left(\left(\frac{r}{r_a}\right)^n - \boldsymbol{g}^{-2n-1}\left(\frac{r_a}{r}\right)^{n+1}\right)P_n(\cos\boldsymbol{q})\right] \qquad (2.1)$$

where the emitter potential is taken as 0 for convenience; r_a and z_f are the distances from the core center to the emitter apex and the extraction electrode, respectively; $P_n(\cos\theta)$ is the Legendre function; parameters n and γ are called the cone index and form factor, respectively[72], where n satisfies $P_n(\cos\theta_0) = 0$ (θ_0 is the exterior cone half angle) and γ is the ratio of r_a to the core radius.

V_0 is related to the extraction voltage V_{ex} by

$$V_{ex} = V_0 \left(\frac{r_a}{z_f}\right)^n \left(1 - \boldsymbol{g}^{-2n-1} - \left(\frac{z_f}{r_a}\right)^n + \boldsymbol{g}^{-2n-1}\left(\frac{r_a}{z_f}\right)^{n+1}\right) \approx -V_0 \qquad (2.2)$$

because $z_f \gg r_a$. Note that $V_{ex} < 0$ in the ion emission mode.

The SOC model is a good geometric representation of thermally annealed emitters as the surface roughness is smoothed by surface atom migration from the region of large curvature to the one of small curvature. It is of less value for field-buildup emitters[69]

29

where the emitter end-form is more polyhedral and the emission is highly non-uniform. In this latter case, one of the aforementioned numerical techniques has to be used.

Figure 2-1 shows the SOC core and the equipotentials generated for the case of n = 0.15 (θ_0 = 175.8°) and varied γ. It is seen that for fixed n that smaller γ leads to a more spherical-like end cap. If γ is fixed, then larger n (or smaller θ_0) corresponds to a blunter emitter (Figure 2-2). Therefore different combinations of n and γ can be used to generate a variety of smooth emitter end-forms.

Figure 2-3 shows n as the function of θ_0 determined by $P_n(\cos\theta_0) = 0$. As can be seen, n decreases monotonously with θ_0, and asymptotically goes to 0 as θ_0 approaches 180°. Typical field emitters have θ_0 around 170°, corresponding to n $\approx$ 0.2.

It should be noted that rigorously the radius of curvature of the tip apex r_t is not equal to r_a, rather, since the emitter surface is an equipotential, r_t is determined by

$$r_t = \left| \frac{2\dfrac{\partial V(r_a,0)}{\partial r}}{\dfrac{\partial^2 V(r_a,0)}{\partial r^2}} \right| = \lambda\, r_a$$

$$\lambda = \frac{2(1+n+n\gamma^{1+2n})}{2+n(3+\gamma^{1+2n})+n^2(1-\gamma^{1+2n})}$$

(2.3)

From (2.3), it is seen that λ increases with n and γ, and $1 < \lambda < 2$ for a wide range of emitter morphology.

By differentiating eqn. (2.1), we get the electric field

30

$$E_r(r, \boldsymbol{q}) = \frac{E_a}{n + (n+1)\boldsymbol{g}^{-2n-1}} \cdot \left(n \left(\frac{r}{r_a} \right)^{n-1} + \frac{n+1}{\boldsymbol{g}^{1+2n}} \left(\frac{r}{r_a} \right)^{-2-n} \right) \cdot P_n$$

$$E_q(r, \boldsymbol{q}) = \frac{n \cdot E_a}{n + (n+1)\boldsymbol{g}^{-2n-1}} \cdot \left(\left(\frac{r}{r_a} \right)^{n-1} - \boldsymbol{g}^{-1-2n} \left(\frac{r}{r_a} \right)^{-2-n} \right) \cdot \frac{\cos \boldsymbol{q} \cdot P_n - P_{n-1}}{\sin \boldsymbol{q}}$$

(2.4)

where P_n represents $P_n(\cos\theta)$ and $E_a = E_r(r_a, 0)$ is the emitter apex field

$$E_a = \frac{V_0}{z_f^n r_a^{1-n}} \cdot \left(n + \frac{n+1}{\boldsymbol{g}^{1+2n}} \right)$$

(2.5)

Especially, when n = 0.13, $E_a \propto r_t^{-0.87} z_f^{-0.13}$ which might be compared with the empirical relationship of thermally anne aled emitters[84].
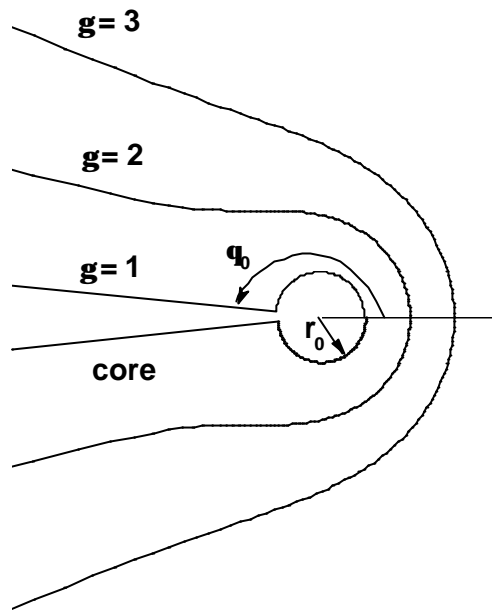
Figure 2-1 SOC equipotentials for fixed n and varied γ. γ = 1 corresponds to the core
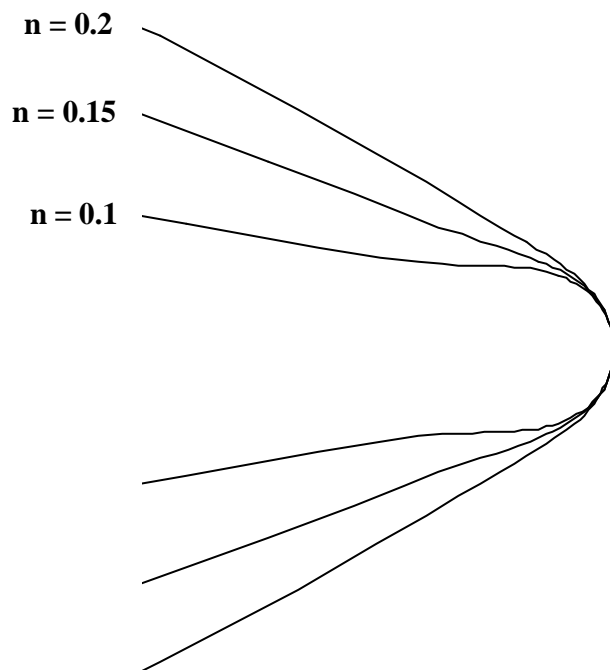
Figure 2-2 SOC equipotentials for fixed γ and varied n
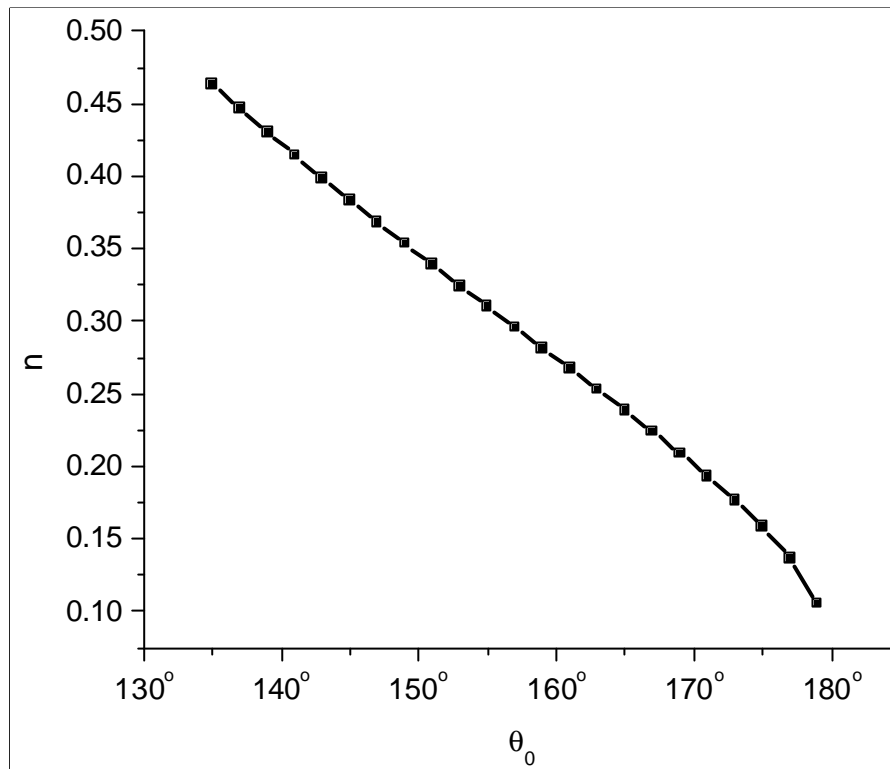
Figure 2-3 Cone index n vs. the exterior cone half angle θ_0

2.3   Optical Properties Of SOC Emitters

Unless otherwise stated, all optical calculations are done for He gas and tungsten emitters with $I = 24.5\text{eV}$ and $\phi = 4.5\text{eV}$.

2.3.1   Theory Of Electrostatic Lens

2.3.1.1   Ray Equation And Paraxial Approximation

In general, the optical properties of diode region can be analyzed by the electrostatic lens theory, as any axially symmetric field distribution acts as a lens. In the theory of charged particle optics, the behavior of the charged particle is often described by the ray equation which is most conveniently obtained from the well-known law of least action, whose general form for positive ions, in the presence of electric and magnetic fields, is given by[85]

$$d\int_{P1}^{P2}\left(\sqrt{\Phi^*}\,ds + h\mathbf{A}\cdot d\mathbf{s}\right) = 0 \qquad (2.6)$$

where ds is the elemental path of the particle under consideration; P1 and P2 are two fixed terminal points of the path; $\eta = (q/2m)^{1/2}$, q is the charge of ion and m its mass; $\mathbf{A}$ is the magnetic vector potential; Φ^* is the relativistically corrected electric potential with its origin and sign chosen such that $q\Phi^*$ is equal to the kinetic energy of the charged particle

$$\Phi^* = \Phi\cdot\left(1 + \mathbf{e}\cdot\Phi\right) \qquad (2.7)$$

where $\varepsilon = q/(2mc^2)$.

The variational principle of (2.6) states that the real path of the particle is such that the integral in (2.6) over this path assumes a stationary value, which is analogous to Fermat's law in light optics.

For systems with straight axis, (2.6) is turned into the following form

$$d\int_{z1}^{z2} M(x,y,z;\acute{x},y')dz = 0$$

$$M(x,y,z;x',y') = \Phi^{*1/2}(1+x'^2+y'^2)^{1/2} +h(A_x x' + A_y y' + A_z)$$

(2.8)

where $M(x,y,z,x',y')$ is the refractive index.

The ray equations are the Euler's equations of this variational principle, which can be expressed as[70] (z is the optical axis)

$$x'' \equiv \frac{d^2x}{dz^2} = \frac{r^2}{2\Phi^*}\left(\frac{\partial\Phi^*}{\partial x} - x'\Phi^{*'}\right) + \frac{hr^2}{\Phi^{*1/2}}\left(y'B_t - rB_y\right)$$

$$y'' \equiv \frac{d^2y}{dz^2} = \frac{r^2}{2\Phi^*}\left(\frac{\partial\Phi^*}{\partial y} - y'\Phi^{*'}\right) + \frac{hr^2}{\Phi^{*1/2}}\left(rB_x - x'B_t\right)$$

(2.9)

where ' denotes the derivative with respect to z; $\rho = (1+x'^2+y'^2)^{1/2}$; $\mathbf{B} = (B_x, B_y, B_z)$ is the magnetic field and $B_t = (x'B_x+y'B_y+B_z)/\rho$ is the component tangential to the path.

In all cases of interest to FIB, the relativistic effect can be safely neglected because of the large mass of ion. It can be easily verified that at 10MeV that the correction is only about 0.005 ($\epsilon\cdot\Phi = 0.0053$). Moreover, in the emission diode region, the magnetic field is absent. So that the ray equation is reduced to

$$x'' = \frac{r^2}{2\Phi}\left(\frac{\partial \Phi}{\partial x} - x'\Phi'\right)$$

$$y'' = \frac{r^2}{2\Phi}\left(\frac{\partial \Phi}{\partial y} - y'\Phi'\right)$$

(2.10)

The important near-axis properties of the lens can be obtained by making the paraxial approximation in eqn.(2.10) where only up to linear terms with respect to x, x', y and y' are kept. In fact, assuming rotational symmetry that is the most important case in charged particle optics, the potential $\Phi(r,z)$ can be expanded around the axis as

$$\Phi(r,z) = \mathbf{y}(z) - \frac{r^2}{4}\mathbf{y}''(z) + \frac{r^4}{64}\mathbf{y}^{(4)}(z) + O(r^6)$$

(2.11)

with $\psi(z) = \Phi(0,z)$. And the paraxial ray equation becomes

$$w'' + \frac{\mathbf{y}'(z)}{2\mathbf{y}(z)}w' + \frac{\mathbf{y}''(z)}{4\mathbf{y}(z)}w = 0$$

(2.12)

where w = x + i·y is the complex notation of the ray.

Eqn.(2.12) is a linear, second-order, homogenous ODE, so that any solution can be expressed as a combination of two linearly independent solutions. A convenient choice of these two canonical rays is

$$h(z_0) = 0,\ h'(z_0) = 1$$

$$g(z_0) = 1,\ g'(z_0) = 0$$

(2.13)

so that by specifying the (complex) initial position w_0 and slope w_0', a paraxial ray w(z) can be expressed as

$$w(z) = w_0 g(z) + w_0' h(z) \tag{2.14}$$

An important property of the paraxial ray equation is the existence of an invariant, the Wronskian

$$\psi^{1/2}(u_1'u_2 - u_1 u_2') = const. \tag{2.15}$$

where u_1 and u_2 are two linearly independent paraxial rays, as is easily verified by use of the paraxial ray equation. Specifically, let $u_1 = h$ and $u_2 = g$, (2.15) becomes

$$h'g - g'h = \frac{\psi_0^{1/2}}{\psi^{1/2}} \tag{2.16}$$

where $\psi_0 = \psi(z_0)$.

2.3.1.2   Gaussian Optical Properties Of Emission Diode Region

With the aid of the paraxial rays, the Gaussian optical properties, such as the focal length f, the linear magnification M, and the angular magnification M_A, of the diode region can be determined.

$$f = -\frac{1}{g'(z_f)}$$

$$M_A = h'(z_f) \tag{2.17}$$

$$M = \frac{1}{M_A}\left(\frac{\psi_0}{\psi_f}\right)^{1/2}$$

where $\psi_f = \psi(z_f)$.

37

These quantities can only be calculated numerically for the emission diode region. For this purpose, it is more convenient to rewrite the paraxial ray equation by introducing the reduced ray representation[86]

$$R(z) = w(z) \left(\frac{y(z)}{y_0} \right)^{1/4} \tag{2.18}$$

so that eqn. (2.12) takes the form

$$R'' + \frac{3}{16} \left(\frac{y'}{y} \right)^2 R = 0 \tag{2.19}$$

Corresponding to $h(z)$ and $g(z)$, we now have $R_h(z)$ and $R_g(z)$, satisfying the initial conditions

$$R_h(z_0) = 0, \; R_h'(z_0) = 1$$

$$R_g(z_0) = 1, \; R_g'(z_0) = \frac{y_0'}{4y_0} \tag{2.20}$$

And (2.17) can be expressed in terms of R_h and R_g as

$$f = -\cfrac{1}{R_g'(z_f) - \cfrac{\mathbf{y}_f'}{4\mathbf{y}_f} R_g(z_f)} \left(\frac{\mathbf{y}_f}{\mathbf{y}_0}\right)^{1/4}$$

$$M_A = \left(R_h'(z_f) - \frac{\mathbf{y}_f'}{4\mathbf{y}_f} R_h(z_f)\right)\left(\frac{\mathbf{y}_0}{\mathbf{y}_f}\right)^{1/4} \tag{2.21}$$

$$M = \frac{1}{M_A}\left(\frac{\mathbf{y}_0}{\mathbf{y}_f}\right)^{1/2} = \cfrac{1}{R_h'(z_f) - \cfrac{\mathbf{y}_f'}{4\mathbf{y}_f} R_h(z_f)}\left(\frac{\mathbf{y}_0}{\mathbf{y}_f}\right)^{1/4}$$

The axial potential distribution of the SOC diode region is obtained, from eqn. (2.1) and (2.5), as (note that $\psi \geq 0$)

$$\mathbf{y}(z) = \frac{E_a r_a}{n + (n+1)\mathbf{g}^{-2n-1}}\left[\mathbf{g}^{-2n-1} - 1 + \left(\frac{z}{r_a}\right)^n - \mathbf{g}^{-2n-1}\left(\frac{z}{r_a}\right)^{-n-1}\right] \tag{2.22}$$

If we simply substitute (2.22) into the ray equation, as is done when dealing with the FE cathode, we will get singularity at the emitter apex $z = r_a$, in which case the emitter acts as a cathode lens. In field ionization, however, the ions are all generated beyond the critical distance x_c above the emitter surface, where they have an average energy of $3kT_t/2$ (T_t is the tip temperature). Therefore, eqn. (2.22) should be modified as

$$\begin{aligned}
\mathbf{y}(z) &= KE_i - E_a x_c + \frac{E_a r_a}{n + (n+1)\mathbf{g}^{-2n-1}}\left[\mathbf{g}^{-2n-1} - 1 + \left(\frac{z}{r_a}\right)^n - \mathbf{g}^{-2n-1}\left(\frac{z}{r_a}\right)^{-n-1}\right] \\
&= \frac{3kT_t - 2(I - \mathbf{f})}{2q} + \frac{E_a r_a}{n + (n+1)\mathbf{g}^{-2n-1}}\left[\mathbf{g}^{-2n-1} - 1 + \left(\frac{z}{r_a}\right)^n - \mathbf{g}^{-2n-1}\left(\frac{z}{r_a}\right)^{-n-1}\right]
\end{aligned} \tag{2.23}$$

where KE_i is the potential equivalent of the initial kinetic energy; x_c is defined in eqn. (1.2); $E_a \cdot x_c$ is essentially the potential at the critical distance above the emitter surface by considering that $x_c \ll r_a$.

Accordingly, we have

$$\boldsymbol{y}'(z) = \frac{E_a}{n + (n+1)\boldsymbol{g}^{-2n-1}} \left(n \left(\frac{z}{r_a} \right)^{n-1} + (n+1)\boldsymbol{g}^{-2n-1} \left(\frac{z}{r_a} \right)^{-n-2} \right) \qquad (2.24)$$

The first step in solving the paraxial ray eqn. (2.19) is to transform it into two 1st order differential equations by introducing proper auxiliary variables

$$y_0 = R, \quad y_1 = R' \qquad (2.25)$$

so that

$$y_0' = y_1$$
$$y_1' = -\frac{3}{16} \left(\frac{\boldsymbol{y}'}{\boldsymbol{y}} \right)^2 y_0 \qquad (2.26)$$

A C routine is written where the integration of ODE is done by the Bulirsch-Stoer extrapolation method with adaptive step size control[87]. Compared with the common Runge-Kutta algorithm, the extrapolation method has the advantage that fewer steps and less stringent error control are needed to obtain a given accuracy for problems involving smooth functions. Indeed, in the accuracy check for both spherical and SOC emitters, given identical internal local truncation errors, the relative energy errors by the extrapolation method are found to be about one order of magnitude smaller than the

40

Runge-Kutta method, while the latter needs 1.5–16 times more intermediate steps than the former, depending on the truncation error specified.

The accuracy check procedure goes as follows.

For a spherical emitter with radius r_a and surface field E_a, assume an electron is emitted tangential to the surface with initial kinetic energy KE_e. By solving the equation of motion for this electron, the following trajectory can be obtained[78]

$$\cos q \equiv \frac{z}{\sqrt{r^2+z^2}} = \frac{1+\dfrac{2KE_e}{E_a\sqrt{r^2+z^2}}}{1+\dfrac{2KE_e}{E_a r_a}} \tag{2.27}$$

where (r,z) are the cylindrical coordinates and θ is the polar angle. With (2.27), the relative error Δ_θ of $\cos\theta$ is evaluated by

$$\Delta_q = \frac{\cos\tilde{q}-\cos q}{\cos q} = \frac{E_a+2KE_e/r_a}{E_a\sqrt{1+(\tilde{r}/\tilde{z})^2}+2KE_e/\tilde{z}} - 1 \tag{2.28}$$

where ($\tilde{r}$, $\tilde{z}$) represent the numerical solutions.

Likewise, the relative error in energy Δ_e is given by

$$\Delta_e = \frac{E_a r_a(r_a/\tilde{r}-1)+\dfrac{1}{2h_e}(\dot{\tilde{r}}^2+\dot{\tilde{z}}^2)-KE_e}{KE_e} \tag{2.29}$$

where "dot" denotes the derivative with respect to time; $\eta_e = 1.76\times10^{11}$C/kg is the electron charge to mass ratio.

The results are given in Table 2-1 where $r_a = 10$nm, $E_a = 2$V/Å and $KE_e = 0.1$eV. The flight time is adjusted to yield $\tilde{z} = 0.1$mm, 1mm and 1cm, whose relative error is controlled under 10^{-10}. For the purpose of comparison, the results of two local truncation errors, 10^{-8} and 10^{10}, are listed.

For the SOC model, there is no independent check on the trajectory without an analytical solution, but the relative energy error can be calculated in a similar way. And by adjusting the local truncation error, relative energy errors of $\leq 10^{-7}$ can be routinely achieved. From the results of the spherical emitter, we then expect the relative error in the ratio of z/r to be about 10^{-13} or smaller.

Table 2-2 lists the geometric parameters of the SOC emitter and the applied surface electric field, for which the optical properties are calculated. The tip temperature is taken to be 78°K ($KE_i = 0.01$eV). The value of z_f is set to 1mm, which agrees with typical settings in FIB systems. It should be noted that, from the ray equation, by changing the dimensions of the diode region by a common factor, the optical properties (including aberrations) all change by the same factor. On the other hand, changing the potential by a common factor does not affect the optical properties.

The magnifications per unit distance M/z_f and M_A/z_f are listed in Table 2-3 for each configuration in Table 2-2.

42

Table 2-1 Accuracy check of the B-S extrapolation algorithm for spherical emitter

$\tilde{z}$ (mm)	$\tilde{r}$ (μm)	$\dot{\tilde{z}}$ (m/sec)	$\dot{\tilde{r}}$ (m/sec)	Δ_θ	Δ_e
$r_a = 10\text{nm}, E_a = 2\times10^{10}\text{V/m}, KE_e = 0.1\text{eV}, \text{local truncation error} = 10^8$					
0.1	4.473	8.381×10^6	3.749×10^5	-3.86×10^{-13}	1.80×10^{-6}
1	44.732	8.381×10^6	3.749×10^5	-3.84×10^{-13}	1.52×10^{-5}
10	447.325	8.381×10^6	3.749×10^5	-3.84×10^{-13}	1.66×10^{-5}
$r_a = 10\text{nm}, E_a = 2\times10^{10}\text{V/m}, KE_e = 0.1\text{eV}, \text{local truncation error} = 10^{10}$					
$\tilde{z}$ (mm)	$\tilde{r}$ (μm)	$\dot{\tilde{z}}$ (m/sec)	$\dot{\tilde{r}}$ (m/sec)	Δ_θ	Δ_e
0.1	4.473	8.381×10^6	3.749×10^5	-2.89×10^{-15}	2.16×10^{-7}
1	44.732	8.381×10^6	3.749×10^5	-2.89×10^{-15}	2.52×10^{-7}
10	447.325	8.381×10^6	3.749×10^5	-2.66×10^{-15}	2.63×10^{-7}

Table 2-2 Emitter and gas parameters (marked by '×') for the optical calculation.

$z_f = 1mm$; $KE_i = 0.01eV$			
	γ		
	1.5	2	2.5	3

	1.5	2	2.5	3
n = 0.12		×	×	×
0.14		×	×	×
0.16		×	×	×
0.18		×	×	×
0.2	×	×	×	×

	E_a (10^8V/cm)		
	2	3	4
$r_a=0.01\mu m$	×	×	×
0.05	×	×	×
0.1	×	×	×
0.5	×	×	×
1	×	×	×

44

Table 2-3 Magnifications per unit distance M/z_f and M_A/z_f for SOC emitters

$E_a = 2\times10^8$ V/cm					
M/z_f (mm^{-1}) M_A/z_f (mm^{-1})	z_f / r_a				
	10^5	2×10^4	10^4	2×10^3	10^3
$(n, \gamma) = (0.12, 2)$	0.370 8.05×10^{-3}	0.390 3.80×10^{-3}	0.399 2.76×10^{-3}	0.422 1.32×10^{-3}	0.433 9.62×10^{-4}
$(0.12, 2.5)$	0.363 7.47×10^{-3}	0.383 3.55×10^{-3}	0.393 2.58×10^{-3}	0.416 1.24×10^{-3}	0.427 9.03×10^{-4}
$(0.12, 3)$	0.358 7.04×10^{-3}	0.379 3.35×10^{-3}	0.388 2.44×10^{-3}	0.412 1.17×10^{-3}	0.424 8.56×10^{-4}
$(0.14, 2)$	0.359 7.36×10^{-3}	0.380 3.52×10^{-3}	0.390 2.57×10^{-3}	0.415 1.24×10^{-3}	0.427 9.06×10^{-4}
$(0.14, 2.5)$	0.353 6.81×10^{-3}	0.374 3.27×10^{-3}	0.384 2.39×10^{-3}	0.409 1.15×10^{-3}	0.422 8.46×10^{-4}
$(0.14, 3)$	0.349 6.39×10^{-3}	0.370 3.08×10^{-3}	0.380 2.25×10^{-3}	0.406 1.09×10^{-3}	0.418 7.99×10^{-4}
$(0.16, 2)$	0.349 6.74×10^{-3}	0.372 3.26×10^{-3}	0.382 2.39×10^{-3}	0.409 1.16×10^{-3}	0.421 8.53×10^{-4}
$(0.16, 2.5)$	0.344 6.20×10^{-3}	0.366 3.01×10^{-3}	0.377 2.21×10^{-3}	0.404 1.08×10^{-3}	0.417 7.93×10^{-4}
$(0.16. 3)$	0.341 5.81×10^{-3}	0.363 2.83×10^{-3}	0.374 2.08×10^{-3}	0.401 1.02×10^{-3}	0.414 7.47×10^{-4}
$(0.18, 2)$	0.340 6.17×10^{-3}	0.364 3.01×10^{-3}	0.375 2.22×10^{-3}	0.403 1.09×10^{-3}	0.416 8.04×10^{-4}
$(0.18, 2.5)$	0.336 5.66×10^{-3}	0.359 2.78×10^{-3}	0.370 2.04×10^{-3}	0.399 1.01×10^{-3}	0.413 7.44×10^{-4}
$(0.18, 3)$	0.334 5.29×10^{-3}	0.357 2.60×10^{-3}	0.368 1.92×10^{-3}	0.397 0.947×10^{-3}	0.411 7.00×10^{-4}
$(0.2, 1.5)$	0.339 6.35×10^{-3}	0.364 3.12×10^{-3}	0.376 2.30×10^{-3}	0.405 1.14×10^{-3}	0.418 8.42×10^{-4}
$(0.2, 2)$	0.332 5.64×10^{-3}	0.357 2.79×10^{-3}	0.369 2.06×10^{-3}	0.398 1.02×10^{-3}	0.412 7.57×10^{-4}
$(0.2, 2.5)$	0.329 5.16×10^{-3}	0.353 2.56×10^{-3}	0.365 1.89×10^{-3}	0.395 0.942×10^{-3}	0.409 6.99×10^{-4}
$(0.2, 3)$	0.328 4.82×10^{-3}	0.352 2.39×10^{-3}	0.363 1.77×10^{-3}	0.394 0.883×10^{-3}	0.408 6.56×10^{-4}

$E_a = 3\times10^8$ V/cm					
M/z_f (mm^{-1}) M_A/z_f (mm^{-1})	z_f / r_a				
	10^5	2×10^4	10^4	2×10^3	10^3
$(n, \gamma) = (0.12, 2)$	0.370 6.55×10^{-3}	0.390 3.11×10^{-3}	0.399 2.26×10^{-3}	0.422 1.08×10^{-3}	0.433 7.85×10^{-4}

M/z_f (mm^{-1}) M_A/z_f (mm^{-1})	10^5	2×10^4	10^4	2×10^3	10^3
(0.12, 2.5)	0.363 6.09×10^{-3}	0.383 2.90×10^{-3}	0.392 2.11×10^{-3}	0.416 1.01×10^{-3}	0.427 7.37×10^{-4}
(0.12, 3)	0.358 5.74×10^{-3}	0.378 2.74×10^{-3}	0.388 1.99×10^{-3}	0.412 9.57×10^{-4}	0.424 6.99×10^{-4}
(0.14, 2)	0.359 6.00×10^{-3}	0.380 2.87×10^{-3}	0.390 2.10×10^{-3}	0.415 1.01×10^{-3}	0.427 7.40×10^{-4}
(0.14, 2.5)	0.353 5.55×10^{-3}	0.374 2.67×10^{-3}	0.384 1.95×10^{-3}	0.409 9.42×10^{-4}	0.422 6.90×10^{-4}
(0.14, 3)	0.349 5.21×10^{-3}	0.370 2.51×10^{-3}	0.380 1.84×10^{-3}	0.406 8.90×10^{-4}	0.418 6.53×10^{-4}
(0.16, 2)	0.349 5.49×10^{-3}	0.371 2.66×10^{-3}	0.382 1.95×10^{-3}	0.408 9.49×10^{-4}	0.421 6.97×10^{-4}
(0.16, 2.5)	0.344 5.06×10^{-3}	0.366 2.46×10^{-3}	0.377 1.80×10^{-3}	0.404 8.80×10^{-4}	0.417 6.47×10^{-4}
(0.16. 3)	0.340 4.75×10^{-3}	0.363 2.31×10^{-3}	0.374 1.69×10^{-3}	0.401 8.29×10^{-4}	0.414 6.10×10^{-4}
(0.18, 2)	0.340 5.03×10^{-3}	0.364 2.46×10^{-3}	0.375 1.81×10^{-3}	0.403 8.90×10^{-4}	0.416 6.57×10^{-4}
(0.18, 2.5)	0.336 4.62×10^{-3}	0.359 2.27×10^{-3}	0.370 1.67×10^{-3}	0.399 8.23×10^{-4}	0.413 6.08×10^{-4}
(0.18, 3)	0.333 4.42×10^{-3}	0.357 2.12×10^{-3}	0.368 1.57×10^{-3}	0.397 7.73×10^{-3}	0.411 5.71×10^{-4}
(0.2, 1.5)	0.339 5.18×10^{-3}	0.364 2.55×10^{-3}	0.376 1.88×10^{-3}	0.405 9.31×10^{-4}	0.418 6.88×10^{-4}
(0.2, 2)	0.332 4.60×10^{-3}	0.357 2.28×10^{-3}	0.368 1.68×10^{-3}	0.398 8.35×10^{-4}	0.412 6.19×10^{-4}
(0.2, 2.5)	0.329 4.22×10^{-3}	0.353 2.09×10^{-3}	0.365 1.55×10^{-3}	0.395 7.69×10^{-4}	0.409 5.70×10^{-4}
(0.2, 3)	0.327 3.94×10^{-3}	0.351 1.96×10^{-3}	0.363 1.45×10^{-3}	0.394 7.21×10^{-4}	0.408 5.35×10^{-4}

$E_a = 4\times10^8$ V/cm					
M/z_f (mm^{-1}) M_A/z_f (mm^{-1})			z_f / r_a		
	10^5	2×10^4	10^4	2×10^3	10^3
(n, γ) = (0.12, 2)	0.370 5.67×10^{-3}	0.390 2.69×10^{-3}	0.399 1.95×10^{-3}	0.422 9.34×10^{-4}	0.433 6.80×10^{-4}
(0.12, 2.5)	0.363 5.27×10^{-3}	0.383 2.51×10^{-3}	0.392 1.83×10^{-3}	0.416 8.75×10^{-4}	0.427 6.38×10^{-4}
(0.12, 3)	0.358 4.96×10^{-3}	0.378 2.37×10^{-3}	0.388 1.73×10^{-3}	0.412 8.29×10^{-4}	0.424 6.05×10^{-4}
(0.14, 2)	0.359 5.19×10^{-3}	0.380 2.49×10^{-3}	0.390 1.82×10^{-3}	0.415 8.76×10^{-4}	0.427 6.40×10^{-4}
(0.14, 2.5)	0.353 4.80×10^{-3}	0.374 2.31×10^{-3}	0.384 1.69×10^{-3}	0.409 8.16×10^{-4}	0.422 5.98×10^{-4}

(0.14, 3)	0.349 4.51×10⁻³	0.370 2.17×10⁻³	0.380 1.59×10⁻³	0.406 7.71×10⁻⁴	0.418 5.65×10⁻⁴
(0.16, 2)	0.349 4.76×10^{-3}	0.371 2.30×10^{-3}	0.382 1.69×10^{-3}	0.408 8.22×10^{-4}	0.421 6.03×10^{-4}
(0.16, 2.5)	0.343 4.38×10^{-3}	0.366 2.13×10^{-3}	0.377 1.56×10^{-3}	0.404 7.62×10^{-4}	0.417 5.61×10^{-4}
(0.16. 3)	0.340 4.11×10^{-3}	0.363 2.00×10^{-3}	0.373 1.47×10^{-3}	0.401 7.18×10^{-4}	0.414 5.29×10^{-4}
(0.18, 2)	0.340 4.36×10^{-3}	0.364 2.13×10^{-3}	0.375 1.57×10^{-3}	0.403 7.71×10^{-4}	0.416 5.69×10^{-4}
(0.18, 2.5)	0.335 4.00×10^{-3}	0.359 1.96×10^{-3}	0.370 1.45×10^{-3}	0.399 7.12×10^{-4}	0.413 5.26×10^{-4}
(0.18, 3)	0.333 3.75×10^{-3}	0.357 1.84×10^{-3}	0.368 1.36×10^{-3}	0.397 6.69×10^{-3}	0.411 4.95×10^{-4}
(0.2, 1.5)	0.339 4.48×10^{-3}	0.364 2.21×10^{-3}	0.376 1.63×10^{-3}	0.405 8.06×10^{-4}	0.418 5.96×10^{-4}
(0.2, 2)	0.332 3.99×10^{-3}	0.357 1.97×10^{-3}	0.368 1.46×10^{-3}	0.398 7.23×10^{-4}	0.412 5.36×10^{-4}
(0.2, 2.5)	0.328 3.65×10^{-3}	0.353 1.81×10^{-3}	0.365 1.34×10^{-3}	0.395 6.66×10^{-4}	0.409 4.94×10^{-4}
(0.2, 3)	0.327 3.41×10^{-3}	0.351 1.69×10^{-3}	0.363 1.25×10^{-3}	0.393 6.25×10^{-4}	0.408 4.64×10^{-4}

We will find that another relation is useful in estimating the source size. This relation associates the initial polar angle θ of an ion emitted in normal direction with its divergence angle α at the extraction electrode[72](Figure 2-4).
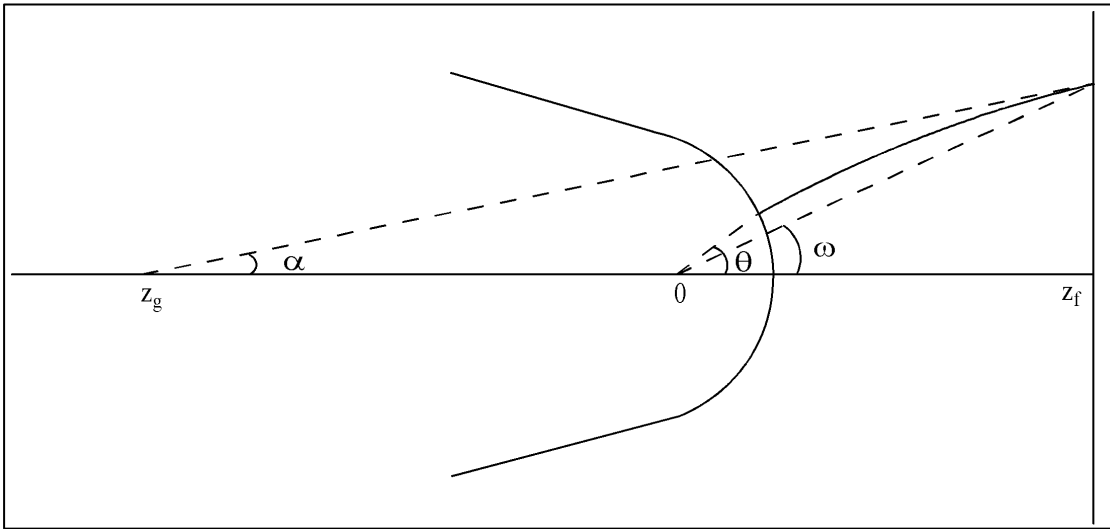
Figure 2-4 Schematic diagram of the ion trajectory in the emission diode region. ω is the aperture half angle.

Define K_θ as

$$K_q = \frac{\tan a}{\tan q} \tag{2.30}$$

Table 2-4 lists the average values of K_θ and their relative errors for $0 \le \theta \le 20°$ and various source parameters as given in Table 2-2.

Table 2-4 Average K_θ and its error

K_θ	$E_a = 2 \times 10^8 V/cm$				
	z_f / r_a				
	10^5	2×10^4	10^4	2×10^3	10^3
$(n, \gamma) = (0.12, 2)$	0.51±2.4%	0.56±2.3%	0.58±2.2%	0.62±2.1%	0.64±2.0%
(0.12, 2.5)	0.47±2.6%	0.51±2.5%	0.53±2.4%	0.57±2.3%	0.59±2.2%
(0.12, 3)	0.43±2.7%	0.48±2.6%	0.49±2.6%	0.53±2.5%	0.55±2.4%
(0.14, 2)	0.47±2.6%	0.52±2.5%	0.53±2.4%	0.58±2.3%	0.60±2.2%
(0.14, 2.5)	0.42±2.8%	0.47±2.6%	0.48±2.6%	0.53±2.5%	0.54±2.4%
(0.14, 3)	0.39±2.9%	0.43±2.8%	0.45±2.7%	0.48±2.6%	0.50±2.6%
(0.16, 2)	0.42±2.8%	0.47±2.6%	0.49±2.6%	0.54±2.4%	0.56±2.4%
(0.16, 2.5)	0.38±2.9%	0.42±2.8%	0.44±2.8%	0.48±2.7%	0.50±2.6%
(0.16. 3)	0.35±3.0%	0.39±2.9%	0.40±2.9%	0.44±2.8%	0.46±2.8%
(0.18, 2)	0.38±2.9%	0.43±2.8%	0.45±2.7%	0.50±2.6%	0.52±2.5%
(0.18, 2.5)	0.34±3.1%	0.39±3.0%	0.40±2.9%	0.45±2.8%	0.47±2.8%
(0.18, 3)	0.31±3.2%	0.35±3.1%	0.37±3.0%	0.41±3.0%	0.43±2.9%
(0.2, 1.5)	0.40±2.8%	0.46±2.7%	0.48±2.6%	0.54±2.5%	0.56±2.4%
(0.2, 2)	0.34±3.0%	0.40±2.9%	0.41±2.9%	0.46±2.8%	0.48±2.7%
(0.2, 2.5)	0.31±3.2%	0.35±3.1%	0.37±3.0%	0.41±3.0%	0.43±2.9%
(0.2, 3)	0.28±3.3%	0.32±3.2%	0.33±3.2%	0.37±3.1%	0.39±3.0%

K_θ	$E_a = 3 \times 10^8 V/cm$				
	z_f / r_a				
	10^5	2×10^4	10^4	2×10^3	10^3
$(n, \gamma) = (0.12, 2)$	0.52±2.4%	0.56±2.2%	0.58±2.2%	0.62±2.0%	0.64±2.0%
(0.12, 2.5)	0.47±2.6%	0.52±2.5%	0.53±2.4%	0.57±2.3%	0.59±2.2%
(0.12, 3)	0.44±2.7%	0.48±2.6%	0.49±2.6%	0.53±2.5%	0.55±2.4%
(0.14, 2)	0.47±2.6%	0.52±2.5%	0.53±2.4%	0.58±2.3%	0.60±2.2%
(0.14, 2.5)	0.43±2.8%	0.47±2.6%	0.48±2.6%	0.53±2.5%	0.54±2.4%
(0.14, 3)	0.39±2.9%	0.43±2.8%	0.45±2.7%	0.48±2.6%	0.50±2.6%
(0.16, 2)	0.43±2.8%	0.47±2.6%	0.49±2.6%	0.54±2.4%	0.56±2.4%
(0.16, 2.5)	0.38±2.9%	0.43±2.8%	0.44±2.8%	0.48±2.7%	0.50±2.6%
(0.16. 3)	0.35±3.0%	0.39±2.9%	0.40±2.9%	0.44±2.8%	0.46±2.8%
(0.18, 2)	0.39±2.9%	0.43±2.8%	0.45±2.7%	0.50±2.6%	0.52±2.5%
(0.18, 2.5)	0.34±3.0%	0.39±3.0%	0.40±2.9%	0.45±2.8%	0.47±2.8%
(0.18, 3)	0.31±3.2%	0.35±3.1%	0.37±3.0%	0.41±3.0%	0.43±2.9%
(0.2, 1.5)	0.41±2.8%	0.46±2.7%	0.48±2.6%	0.54±2.5%	0.56±2.4%
(0.2, 2)	0.35±3.0%	0.40±2.9%	0.42±2.9%	0.46±2.8%	0.48±2.7%
(0.2, 2.5)	0.31±3.2%	0.35±3.1%	0.37±3.0%	0.41±3.0%	0.43±2.9%
(0.2, 3)	0.28±3.3%	0.32±3.2%	0.33±3.2%	0.37±3.1%	0.39±3.0%

K_θ	$E_a = 4 \times 10^8 V/cm$				
	z_f / r_a				
	10^5	2×10^4	10^4	2×10^3	10^3
$(n, \gamma) = (0.12, 2)$	0.52±2.4%	0.56±2.3%	0.58±2.2%	0.62±2.1%	0.64±2.0%
(0.12, 2.5)	0.48±2.6%	0.52±2.5%	0.53±2.4%	0.57±2.3%	0.59±2.2%
(0.12, 3)	0.44±2.7%	0.48±2.6%	0.49±2.6%	0.53±2.5%	0.55±2.4%
(0.14, 2)	0.47±2.6%	0.52±2.5%	0.54±2.4%	0.58±2.3%	0.60±2.2%
(0.14, 2.5)	0.43±2.8%	0.47±2.6%	0.49±2.6%	0.53±2.5%	0.54±2.4%
(0.14, 3)	0.39±2.9%	0.43±2.8%	0.45±2.7%	0.49±2.6%	0.50±2.6%
(0.16, 2)	0.43±2.7%	0.47±2.6%	0.49±2.6%	0.54±2.4%	0.56±2.4%
(0.16, 2.5)	0.39±2.9%	0.43±2.8%	0.44±2.8%	0.48±2.7%	0.50±2.6%
(0.16. 3)	0.35±3.0%	0.39±2.9%	0.41±2.9%	0.44±2.8%	0.46±2.8%
(0.18, 2)	0.39±2.9%	0.43±2.8%	0.45±2.7%	0.50±2.6%	0.52±2.5%
(0.18, 2.5)	0.35±3.0%	0.39±2.9%	0.40±2.9%	0.45±2.8%	0.47±2.8%
(0.18, 3)	0.32±3.1%	0.35±3.1%	0.37±3.0%	0.41±3.0%	0.43±2.9%
(0.2, 1.5)	0.41±2.8%	0.46±2.7%	0.48±2.6%	0.54±2.5%	0.56±2.4%
(0.2, 2)	0.35±3.0%	0.40±2.9%	0.42±2.9%	0.46±2.8%	0.48±2.7%
(0.2, 2.5)	0.31±3.2%	0.35±3.1%	0.37±3.0%	0.41±3.0%	0.43±2.9%
(0.2, 3)	0.28±3.3%	0.32±3.2%	0.33±3.2%	0.37±3.1%	0.339±3.0%

From Table 2-3 and Table 2-4, we can see that both M and K_θ are nearly independent of the electric field E_a. Also, they are both smaller for blunter emitters (i.e. larger n and γ) as well as smaller tip radius.

From the data, it is seen that the variation in M is quite small considering the range of emitter radius and shape covered. Actually, if we set M = 0.38 regardless of n, γ and r_a, the maximum error is only about 14%.

2.3.1.3   Chromatic and Spherical Aberrations of Emission Diode Region

The paraxial ray equation and the Gaussian optical properties hold only for the imaging of points close to the axis with extremely small beam limiting aperture, which is rarely satisfied in practical systems. Thus deviations from the Gaussian image almost always need to be taken into account. For electrostatic lenses, the aberrations originate from the change in the focusing power of the field distribution as the off axis distance changes as well as on charged particles with different energies.

In order to include aberrations in the image, one is prompted to solve the ray equation as given in (2.10), relaxing the paraxial condition. In many cases, however, the deviation is not much. In these cases, for monochromatic beam, it is adequate and more convenient to expand the ray equation in terms of the powers of the ray coordinates and slopes, and keeping only the lowest order terms next to the paraxial ones. In addition, these geometric aberrations are often separated into different types by their dependencies on the ray coordinates and slopes. In rotationally symmetric, electrostatic lenses, there are altogether five 3rd order geometric aberrations[88]: distortion, curvature of field, astigmatism, coma, and spherical aberration.

51

Similarly, in the presence of beam energy spread, the ray equation can be expanded in terms of the energy of the charged particle, and the so-called 1st order chromatic aberrations are resulted by keeping only the linear terms with respect to the energy.

The most important aberrations in the source region, when the beam aperture is small (< 1msr), are the spherical and chromatic aberrations as they don't vanish even for object on axis.

These aberrations are commonly evaluated in the form of integrals of the paraxial ray, the axial potential distribution and their derivatives with respect to the optical axis[70, 88]. It should be noted that the commonly used aberration integrals either involve 4th order derivative of the potential for spherical aberration (and are hence not convenient for numerical calculation, especially for general emitter topography) or assume that the aperture plane is in field-free region. In the diode region, however, the ψ' does not vanish at the extraction electrode. As a result, in order to derive the aberrations in the image plane, we need to know the aberrations not only in position, but also in slope at the aperture plane.
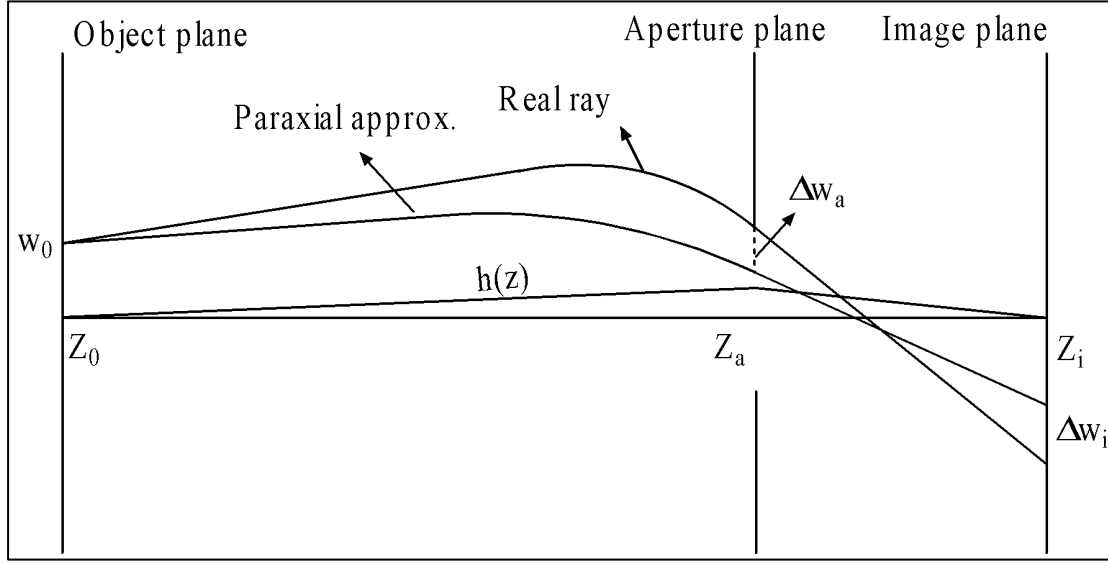
Figure 2-5 Schematic diagram of lens aberration

The lens aberration in the image plane is given by (Figure 2-5)

$$\Delta w_i = \Delta w_a - \frac{h_a}{h_a'} \cdot \Delta w_a'$$ (2.31)

where w(z) is given in (2.14), Δw_a and Δw_a' are the aberrations in position and in slope at the aperture plane, respectively.

We will be using the set of expressions derived by Lencová and Lenc[71] to find Δw_a and $\Delta w_a'$ in order to evaluate Δw_i. First, the ray equation (2.10) is expanded in power series of the beam energy spread and the ray coordinates. And by keeping up to the 1st order term of the energy spread and 3rd order terms of the ray coordinates, we will get[71]

$$\Delta w'' + \Delta w' \frac{y'}{2y} + \Delta w \frac{y'}{4y} = R_3(z) + R_c(z)$$ (2.32)

where

53

$$R_3(z) = \frac{1}{2\boldsymbol{y}^{1/2}} \frac{d}{dz} \left(\boldsymbol{y}^{1/2} w'^2 \overline{w} + \frac{\boldsymbol{y}''}{8\boldsymbol{y}^{1/2}} w \cdot \overline{w} \cdot w' \right) - \frac{\boldsymbol{y}''}{8\boldsymbol{y}} w \cdot w' \cdot \overline{w}' + \frac{1}{32} \left(\frac{\boldsymbol{y}^{(4)}}{\boldsymbol{y}} - \frac{\boldsymbol{y}''^2}{\boldsymbol{y}^2} \right) w^2 \overline{w}$$

(2.33)

$$R_c(z) = \frac{\Delta \boldsymbol{y}}{\boldsymbol{y}} \left(\frac{\boldsymbol{y}'}{2\boldsymbol{y}} w' + \frac{\boldsymbol{y}''}{4\boldsymbol{y}} w \right)$$

represent the effects of 3^d order geometrical deviation and 1^t order energy deviation, respectively, and $\Delta\psi$ is the energy spread.

From eqn.(2.32) and (2.33), the various aberration terms can be obtained by the method of variation of parameters with the aid of the paraxial rays.

Specifically, the chromatic aberration in the image plane is given as

$$\Delta w_{ci} = \frac{\Delta \boldsymbol{y}}{\boldsymbol{y}_0} \left(\left(C_{cf} \cdot \frac{\boldsymbol{y}_0^{1/2}}{\boldsymbol{y}_f^{1/2}} + \frac{\boldsymbol{y}_0}{2\boldsymbol{y}_f} \cdot h_f h_f' \right) \frac{w_0'}{h_a'} + \left(C_{Df} \cdot \frac{\boldsymbol{y}_0^{1/2}}{\boldsymbol{y}_f^{1/2}} + \frac{\boldsymbol{y}_0}{2\boldsymbol{y}_f} \cdot h_f \cdot g_f' \right) \frac{w_0}{h_f'} \right)$$ (2.34)

where the subscript f represents the value evaluated at the extraction electrode $z = z_f$, C_{Cf} and C_{Df} are related to the aberrations in image position and in magnification, respectively, and are given by

$$C_{Cf} = -\frac{\boldsymbol{y}_0^{1/2}}{2} \int_{z_0}^{z_f} \frac{1}{\boldsymbol{y}^{1/2}} \left(h'^2 + \frac{\boldsymbol{y}''}{2\boldsymbol{y}} h^2 \right) dz$$

$$C_{Df} = -\frac{\boldsymbol{y}_0^{1/2}}{2} \int_{z_0}^{z_f} \frac{1}{\boldsymbol{y}^{1/2}} \left(h' \cdot g' + \frac{\boldsymbol{y}''}{2\boldsymbol{y}} h \cdot g \right) dz$$

Let $w_0 = 0$, eqn.(2.34) can be expressed in terms of the slope at the aperture plane

$$\Delta w_{ci} = -\frac{\Delta \boldsymbol{y}}{\boldsymbol{y}_f} w_f' C_{ch}$$

(2.35)

$$C_{ch} = -\frac{h_f}{2h_f'} + \frac{\boldsymbol{y}_f^{1/2}}{2h_f'^2} \int_{z_0}^{z_f} \frac{1}{\boldsymbol{y}^{1/2}} \left(h'^2 + \frac{\boldsymbol{y}''}{4\boldsymbol{y}} h^2 \right) dz$$

where C_{ch} represents the chromatic aberration coefficient, applicable to the emission diode region, referred to the image plane.

Note that in the case $\psi_f' = 0$, we have constant h' and ψ in the image region, and C_{ch} can be verified to reduce to the familiar form

$$C_{ch} = \frac{3y_i^{1/2}}{8h_i'^2} \int_{z_0}^{z_i} \frac{y'^2}{y^{5/2}} h^2 \, dz \tag{2.36}$$

To evaluate the spherical aberration, suppose that this is the only aberration existing or dominating, eqn.(2.32) can be solved to yield

$$\Delta w_s = S \cdot w_0'^2 \overline{w}_0$$
$$\Delta w_s' = S' \cdot w_0'^2 \overline{w}_0 \tag{2.37}$$

where

$$S = S_0 \cdot g - h\left(K_0 - \frac{y''}{16y} h^2 + \frac{1}{2} \right)$$
$$S' = S_0 \cdot g' - h'\left(K_0 - \frac{y''}{16y} h^2 + \frac{1}{2} \right) + \frac{h'^3}{2} + \left(\frac{y'''}{32y} + \frac{y'y'}{64y^2} \right) h^3 \tag{2.38}$$

and

$$S_0 = I_1(h,h,h,h) = \frac{1}{2y_0^{1/2}} \int_{z_0}^{z} y^{1/2} h'^4 \left(1 - \frac{y'}{4y} \frac{h^2}{h'^2} + \frac{3}{8} \frac{y'y''}{y^2} \frac{h^3}{h'^3} + \frac{5}{32} \frac{y''^2}{y^2} \frac{h^4}{h'^4} - \frac{3}{64} \frac{y'^2 y''}{y^3} \frac{h^4}{h'^4} \right) dx$$

$$K_0 = I_1(h,g,h,h) + I_2(h,h)$$

$$I_1(a,b,c,d) = \frac{1}{2y_0^{1/2}} \int_{z_0}^{z} y^{1/2} \left(\left(r_a' r_b' - \frac{y''}{8y} r_a r_b \right) \cdot \left(r_c' r_d' - \frac{y''}{8y} r_c r_d \right) + \right.$$

$$\frac{3}{192} \left(\frac{3y''}{y} r_a r_b + \frac{2y'}{y} (r_a' r_b + r_a r_b') \right) \cdot$$

$$\left(\frac{3y'}{y} r_c r_d + \frac{2y'}{y} (r_c' r_d + r_c r_d') \right) -$$

$$\frac{1}{16} \left(\frac{y'}{y} \right)^2 (r_a' r_b + r_a r_b')(r_c' r_d + r_c r_d') -$$

$$\left. \frac{3}{64} \frac{y'^2 y''}{y^3} r_a r_b r_c r_d \right) dx$$

(2.39)

$$I_2(a,b) = \frac{y''}{32y} r_a r_b - \frac{y_0''}{32y_0'} r_a(z_0) r_b(z_0)$$

From (2.31), (2.37) and (2.38), we can get

$$\Delta w_{si} = C_{si} \cdot w_f'^2 \overline{w}_f'$$

$$C_{si} = -\frac{h_f}{2h_f'} - \frac{h_f^4}{h_f'^4} \left(\frac{y_f'''}{32y_f} + \frac{y_f' y_f''}{64y_f^2} \right) + \frac{1}{h_f'^4} \left(\frac{y_0}{y_f} \right)^{1/2} S_0(z_f)$$

(2.40)

The integrand in eqn. (2.40) involves only up to the 2nd order derivative of ψ, which thus eases numerical calculation of potential distribution for general emitter topography.

In the case $\psi_f' = 0$, C_{si} can be verified to reduce to

$$C_{si} = \frac{1}{16h_i'^4 y_i^{1/2}} \int_{z_0}^{z_i} \frac{h^4}{y^{3/2}} \left(\frac{5y''^2}{4} + \frac{5y'^4}{24y^2} + \frac{14y'^3}{3y} \frac{h'}{h} - \frac{3y'^2}{2} \frac{h'^2}{h^2} \right) dz$$

(2.41)

For the emitter configuration in Table 2-2, the spherical and chromatic aberration coefficients are listed in Table 2-5 and Table 2-6.

The results show that C_{si} and C_{ch} are affected in a complex manner by the emitter shape parameters n and γ, the electric field E_a, and the ratio z_f / r_a. A general trend is that both C_{si} and C_{ch} increase with the electric field and the emitter radius. They are also greater for blunter emitters.

For any given E_a and r_a listed, C_{si} increases approximately linearly while C_{ch} logarithmically with γ. They both have exponential dependence on the cone index n. Moreover, the emitter radius has a remarkable effect on C_{si} and C_{ch}. On one hand, for given n, γ and E_a, C_{si} and C_{ch} increase with r_a more rapidly than linearly but less rapidly than exponentially. On the other hand, there is an interesting feature that differentiates the field ionization from field emission—the critical distance x_c plays an important role, especially at large field and emitter radius (small ratios of z_f / r_a), as shown in Figure 2-6 and Figure 2-7. It is found that although x_c is only on the order of several angstroms, the C_{si} as obtained by taking x_c into account can be more than 10 times higher than when setting $x_c = 0$. As for C_{ch}, the effect is opposite, i.e. the presence of x_c reduces C_{ch} dramatically as compared with FE where $x_c = 0$.

Table 2-5 Spherical aberration coefficient C_{si} referred to the virtual image plane in the diode region

$E_a = 2{\times}10^8 \text{V/cm}$					
C_{si} (μm)	z_f / r_a				
	10^5	$2{\times}10^4$	10^4	$2{\times}10^3$	10^3
$(n, \gamma) = (0.12, 2)$	43.4	112.2	238.2	1.977e3	5.177e3
(0.12, 2.5)	48.8	140.4	306.0	2.560e3	6.667e3
(0.12, 3)	53.6	169.0	376.0	3.171e3	8.230e3
(0.14, 2)	51.3	134.9	285.9	2.330e3	6.040e3
(0.14, 2.5)	57.5	170.8	373.0	3.078e3	7.944e3
(0.14, 3)	63.1	207.3	463.3	3.862e3	9.943e3
(0.16, 2)	60.1	161.8	342.8	2.747e3	7.053e3
(0.16, 2.5)	67.4	207.1	453.7	3.693e3	9.447e3
(0.16. 3)	74.1	253.5	568.8	4.685e3	1.196e4
(0.18, 2)	70.2	193.9	411.4	3.242e3	8.244e3
(0.18, 2.5)	78.8	251.1	551.6	4.426e3	1.122e4
(0.18, 3)	87.0	309.9	697.4	5.666e3	1.433e4
(0.2, 1.5)	70.6	165.4	332.5	2.500e3	6.324e3
(0.2, 2)	81.7	232.8	494.5	3.833e3	9.651e3
(0.2, 2.5)	92.2	304.9	671.2	5.305e3	1.332e4
(0.2, 3)	102.4	379.1	854.6	6.840e3	1.715e4

$E_a = 3{\times}10^8 \text{V/cm}$					
C_{si} (μm)	z_f / r_a				
	10^5	$2{\times}10^4$	10^4	$2{\times}10^3$	10^3
$(n, \gamma) = (0.12, 2)$	44.6	128.6	282.6	2.410e3	6.327e3
(0.12, 2.5)	50.6	162.1	364.3	3.122e3	8.149e3
(0.12, 3)	55.9	196.3	449.0	3.868e3	1.006e4
(0.14, 2)	52.9	154.8	339.3	2.840e3	7.382e3
(0.14, 2.5)	59.8	197.6	444.5	3.753e3	9.711e3
(0.14, 3)	66.2	241.5	554.0	4.713e3	1.215e4
(0.16, 2)	62.2	186.1	407.2	3.348e3	8.620e3
(0.16, 2.5)	70.4	240.4	541.4	4.504e3	1.155e4
(0.16. 3)	78.1	296.3	681.2	5.717e3	1.462e4
(0.18, 2)	72.8	223.6	489.1	3.952e3	1.008e4
(0.18, 2.5)	82.7	292.4	659.2	5.399e3	1.372e4
(0.18, 3)	92.2	363.3	836.3	6.915e3	1.753e4
(0.2, 1.5)	72.5	188.5	392.7	3.045e3	7.727e3
(0.2, 2)	85.1	269.1	588.8	4.674e3	1.180e4
(0.2, 2.5)	97.2	356.0	803.3	6.472e3	1.629e4
(0.2, 3)	109.0	445.8	1.026e3	8.349e3	2.097e4

C_{si} (μm)	z_f / r_a				
	10^5	2×10^4	10^4	2×10^3	10^3
$(n, \gamma) = (0.12, 2)$	45.7	142.6	320.1	2.776e3	7.297e3
(0.12, 2.5)	52.2	180.6	413.5	3.596e3	9.399e3
(0.12, 3)	58.0	219.4	510.6	4.456e3	1.160e4
(0.14, 2)	54.4	171.8	384.4	3.270e3	8.514e3
(0.14, 2.5)	61.9	220.5	505.0	4.323e3	1.120e4
(0.14, 3)	68.9	270.5	630.6	5.429e3	1.402e4
(0.16, 2)	64.1	206.7	461.6	3.855e3	9.941e3
(0.16, 2.5)	73.1	268.6	615.6	5.188e3	1.332e4
(0.16. 3)	81.7	332.6	776.3	6.587e3	1.686e4
(0.18, 2)	75.2	248.8	554.9	4.551e3	1.162e4
(0.18, 2.5)	86.2	327.4	750.1	6.220e3	1.582e4
(0.18, 3)	96.8	408.6	953.8	7.968e3	2.022e4
(0.2, 1.5)	74.4	208.1	443.7	3.505e3	8.910e3
(0.2, 2)	88.2	299.9	668.4	5.383e3	1.360e4
(0.2, 2.5)	101.6	399.3	914.9	7.457e3	1.879e4
(0.2, 3)	115.0	502.2	1.171e3	9.622e3	2.419e4

Table header: $E_a = 4\times10^8$ V/cm

Table 2-6 Chromatic aberration coeff. C_{ch} referred to the virtual image plane in the diode

region

C_{ch} (μm)	z_f / r_a				
$E_a = 2\times10^8$V/cm					
	10^5	2×10^4	10^4	2×10^3	10^3
(n, γ) = (0.12, 2)	50.0	54.9	60.6	117.8	210.7
(0.12, 2.5)	51.1	56.8	63.3	128.6	234.0
(0.12, 3)	51.8	58.3	65.6	138.3	255.2
(0.14, 2)	58.7	64.9	72.0	143.2	256.8
(0.14, 2.5)	59.8	67.0	75.3	157.2	287.4
(0.14, 3)	60.5	68.5	77.8	169.5	315.1
(0.16, 2)	68.2	75.7	84.7	172.8	311.2
(0.16, 2.5)	69.3	78.1	88.4	190.7	350.6
(0.16. 3)	70.0	79.8	91.4	206.5	386.3
(0.18, 2)	78.6	87.7	98.8	207.5	375.5
(0.18, 2.5)	79.6	90.3	103.3	230.3	426.0
(0.18, 3)	80.4	92.3	106.9	250.3	471.2
(0.2, 1.5)	88.2	97.0	108.0	215.6	380.5
(0.2, 2)	89.9	101.1	114.9	248.5	451.9
(0.2, 2.5)	91.0	104.1	120.2	277.2	516.0
(0.2, 3)	91.8	106.4	124.6	302.7	573.0

C_{ch} (μm)	z_f / r_a				
$E_a = 3\times10^8$V/cm					
	10^5	2×10^4	10^4	2×10^3	10^3
(n, γ) = (0.12, 2)	49.8	55.4	62.1	131.2	244.6
(0.12, 2.5)	51.0	57.4	65.1	143.9	272.5
(0.12, 3)	51.7	59.0	67.5	155.3	298.0
(0.14, 2)	58.6	65.6	74.0	160.1	298.8
(0.14, 2.5)	59.7	67.8	77.6	176.6	335.4
(0.14, 3)	60.5	69.5	80.3	191.3	368.8
(0.16, 2)	68.1	76.7	87.3	193.9	362.8
(0.16, 2.5)	69.2	79.2	91.4	215.1	410.5
(0.16. 3)	70.0	81.1	94.8	234.0	453.5
(0.18, 2)	78.5	89.1	102.1	233.8	438.8
(0.18, 2.5)	79.6	91.8	107.1	261.0	499.8
(0.18, 3)	80.4	94.0	111.3	285.1	554.8
(0.2, 1.5)	88.0	98.3	111.3	241.8	443.2
(0.2, 2)	89.9	102.8	119.1	281.1	529.5
(0.2, 2.5)	91.0	106.1	125.2	315.7	607.1
(0.2, 3)	91.8	108.7	130.3	346.3	676.5

C_{ch} (μm)	$E_a = 4{\times}10^8$V/cm				
	z_f / r_a				
	10^5	$2{\times}10^4$	10^4	$2{\times}10^3$	10^3
$(n, \gamma) = (0.12, 2)$	49.8	55.9	63.4	142.6	273.2
(0.12, 2.5)	50.9	58.0	66.6	156.9	305.0
(0.12, 3)	51.7	59.6	69.2	169.7	334.1
(0.14, 2)	58.6	66.3	75.7	174.3	334.1
(0.14, 2.5)	59.7	68.6	79.5	193.0	376.0
(0.14, 3)	60.5	70.3	82.5	209.7	414.3
(0.16, 2)	68.1	77.6	89.4	211.7	406.2
(0.16, 2.5)	69.2	80.2	94.0	235.9	460.7
(0.16. 3)	70.1	82.2	97.7	257.4	510.1
(0.18, 2)	78.5	90.2	104.9	255.9	492.3
(0.18, 2.5)	79.6	93.2	110.4	286.8	562.2
(0.18, 3)	80.5	95.6	115.0	314.4	625.3
(0.2, 1.5)	88.0	99.5	114.3	264.1	496.1
(0.2, 2)	90.0	104.2	122.6	308.6	594.9
(0.2, 2.5)	91.1	107.8	129.5	348.2	684.2
(0.2, 3)	92.0	110.7	135.2	383.2	763.9
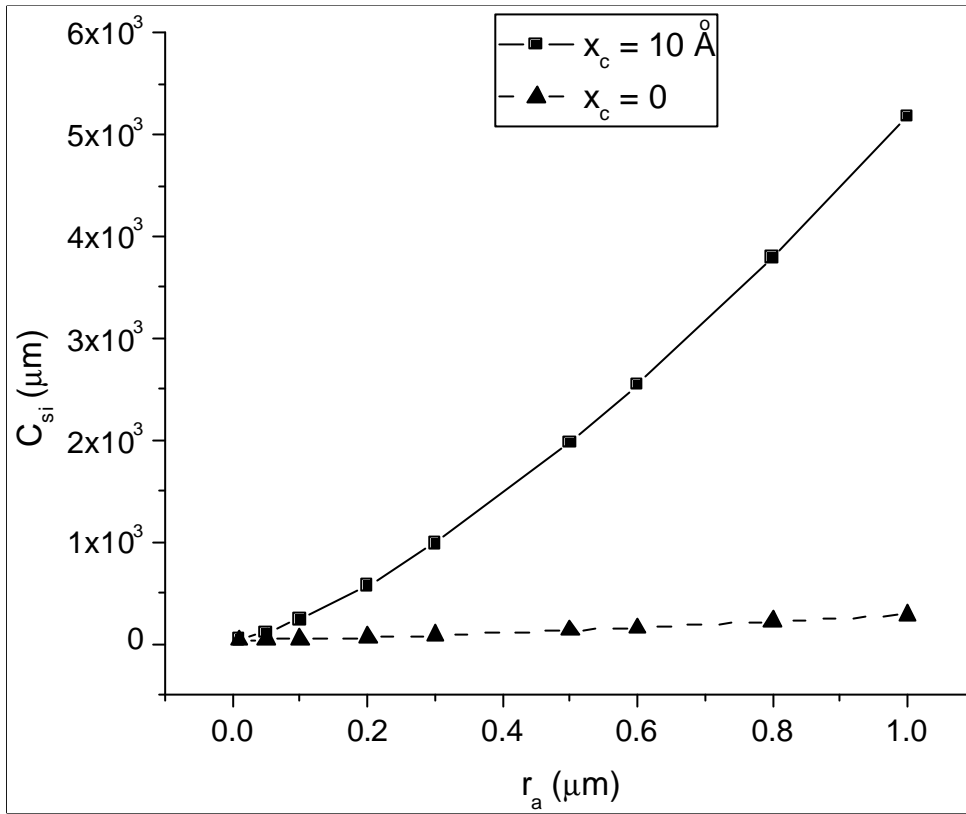
Figure 2-6 Comparison of C_s for FI ($x_c = (I-\phi)/E_a$) and FE ($x_c = 0$). Parameters: $E_a = 2V/\text{Å}$, n = 0.12, $\gamma = 2$
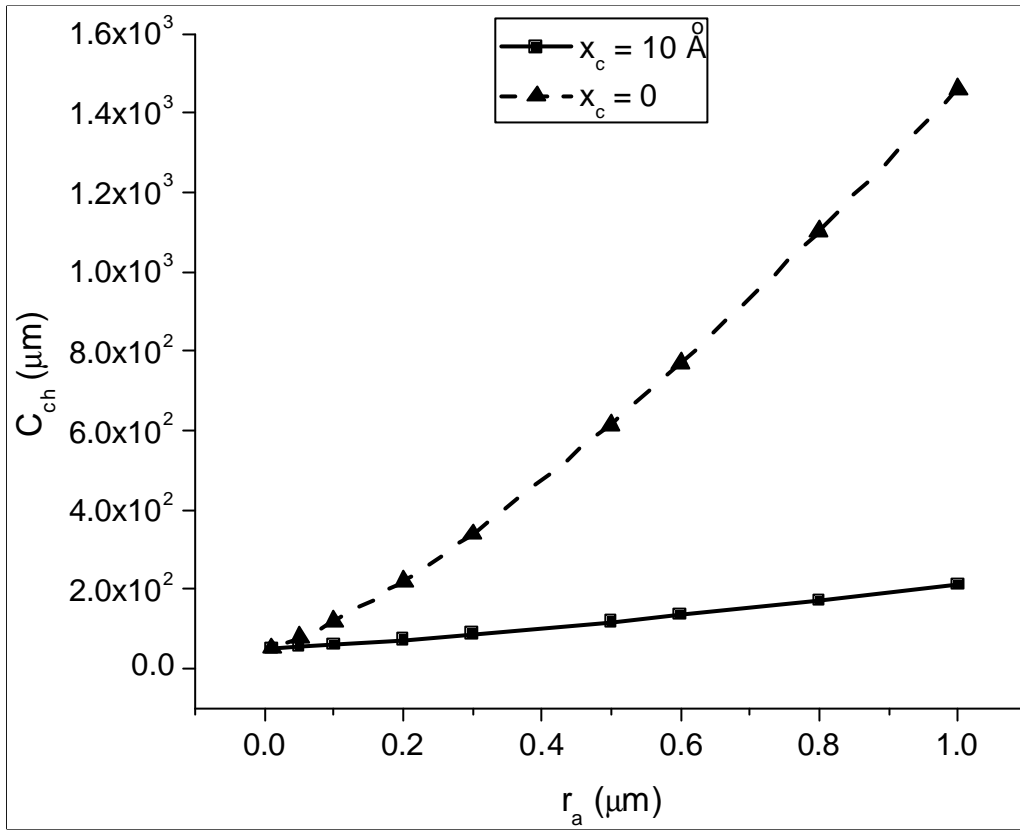
Figure 2-7 Comparison of C_{ch} for FI ($x_c = (I-\phi)/E_a$) and FE ($x_c = 0$). Parameters: $E_a =$ 2V/Å, n = 0.12, $\gamma = 2$

2.3.2 Calculation Of Virtual Source Size By Addition In Quadrature

When the beam limiting aperture is small (<1msr), a convenient and commonly used method to evaluate the virtual source size of GFIS is by adding in quadrature the contributions from the Gaussian source size, spherical and chromatic aberrations, and diffraction effect (but see section 2.3.3 below)

$$
\begin{aligned}
r_s &= \left((M \cdot r_a \cdot \theta)^2 + (C_{si} \cdot \tan^3 \alpha)^2 + \left(C_{ch} \cdot \tan \alpha \cdot \frac{\Delta \psi}{\psi_f} \right)^2 + \left(\frac{0.61}{\alpha} \frac{h}{\sqrt{2mq\psi_f}} \right)^2 \right)^{1/2} \\
&= \left((M \cdot r_a \cdot \theta)^2 + (C_{si} \cdot K_\theta^3 \tan^3 \theta)^2 + \left(C_{ch} \cdot K_\theta \tan \theta \cdot \frac{\Delta V}{\psi_f} \right)^2 + \left(\frac{8.8 \times 10^{-6}}{K_\theta \theta \sqrt{\psi_f}} \right)^2 \right)^{1/2}
\end{aligned}
\tag{2.42}
$$

where the last term represents the diffraction effect (for He ion). θ is the half angle of the beam-limiting aperture (Figure 2-4), and ΔV is the beam energy spread, which is about 1eV for GFIS. In (2.42), r_a, C_{si} and C_{ch} are in μm, and Δψ and ψ_f in volt.

Note that the diffraction effect for ion is usually negligible due to its large mass as compared with electrons. The diffraction effect of He ions is noticeable only when angle θ is so small such that

$$
\theta^2 \leq \frac{8.8 \times 10^{-6}}{M K_\theta r_a \sqrt{V_{ex}}}
\tag{2.43}
$$

And from Figure 2-4, this corresponds to a beam aperture Ω of

$$
\Omega = \pi \theta^2 K_\theta^2 \left(1 - \frac{z_g}{z_f} \right)^2 \leq \frac{2.7 \times 10^{-5}}{r_a \sqrt{V_{ex}}}
\tag{2.44}
$$

64

where the second expression derives since $M \approx K_\theta$ (see Table 2-3 and Table 2-4) and $\left| z_g \right|$ << z_f. For a typical case, let $r_a = 0.1\mu m$ and extraction voltage of 15kV, we have

$$\Omega \leq 0.002 \text{msr} \qquad (2.45)$$

Since M, K_θ and C_{si}, C_{ch} are not sensitive functions of the emitter form factor γ, we may calculate their average values for $\gamma = 2$, 2.5 and 3, for each individual n, r_a and E_a. The resulting r_s for beam aperture of 0.1msr is listed in Table 2-7.

Table 2-7 Virtual source size ξ obtained by addition in quadrature at beam limiting aperture of 0.1msr

$E_a = 2\times10^8$V/cm					
r_s (nm)	z_f / r_a				
	10^5	2×10^4	10^4	2×10^3	10^3
n = 0.12	0.21	0.21	0.40	2.01	4.03
0.14	0.19	0.22	0.43	2.12	4.27
0.16	0.18	0.24	0.46	2.26	4.56
0.18	0.17	0.25	0.49	2.43	4.91
0.2	0.15	0.27	0.53	2.66	5.34

$E_a = 3\times10^8$V/cm					
r_s (nm)	z_f / r_a				
	10^5	2×10^4	10^4	2×10^3	10^3
n = 0.12	0.15	0.21	0.41	2.03	4.10
0.14	0.14	0.22	0.43	2.15	4.35
0.16	0.13	0.23	0.47	2.30	4.66
0.18	0.12	0.25	0.49	2.48	5.04
0.2	0.11	0.27	0.53	2.70	5.51

$E_a = 4\times10^8$V/cm					
r_s (nm)	z_f / r_a				
	10^5	2×10^4	10^4	2×10^3	10^3
n = 0.12	0.11	0.20	0.41	2.05	4.16
0.14	0.11	0.22	0.43	2.17	4.43
0.16	0.10	0.23	0.47	2.33	4.77
0.18	0.10	0.25	0.49	2.52	5.17
0.2	0.09	0.27	0.54	2.75	5.67

It is found that for emitter radius less than 0.1μm ($z_f/r_a > 10^4$), the chromatic aberration dominates in the aberration terms, while for emitter radius greater than 0.1μm, the spherical aberration dominates.

An interesting feature of Table 2-7 is that r_s is virtually independent of the emitter shape, i.e. n and γ, as well as the extraction voltage in the range listed, and that it is largely determined by the emitter radius. By setting n = 0.16 and E_a = 3V/Å, the maximum error induced for emitters with n in 0.12–0.2 and E_a in 2V/Å–4V/Å is found to be within 20%, except at the smallest emitter radius r_a = 10nm where the chromatic aberration dominates and the diffraction effect is the most appreciable and r_s is hence more field sensitive (with relative error of 62%). This conclusion is true even for a beam-limiting aperture as large as 1msr—with relative error less than 54%—where the aberrations become large.

It is therefore not unreasonable to study the dependence of r_s on the emitter radius (for a given emitter to electrode distance) and the beam limiting aperture, regardless of the extraction voltage and detailed emitter shape within a fairly large range—note that the current emission characteristic changes drastically as the field changes from 2V/Å–4V/Å for He gas, as will be shown in Chapter 3.

Figure 2-8 (semi log plot) shows the calculated virtual source size of GFIS of He gas and W emitter at 78°K, as a function of the beam limiting aperture for different emitter radii, which is applicable for E_a in the range 2V/Å–4V/Å.

Additional information is exposed by the dependence of source size on the tip temperature. In order to study this effect, a typical emitter with r_a = 0.1μm is selected, as the tip temperature is changed from 20°K–100°K, the source size r_s is plotted in Figure

2-9 as a function of the beam limiting aperture. It is interesting to see that as the tip temperature reduces, the virtual source size increases, which may seem to be against one's intuition. This effect, however, demonstrates that the chromatic aberration in GFIS is usually dominated by the spherical aberration (except for very small emitters ~10nm), and is the result of the fact that as the initial kinetic energy of ion is reduced, the spherical aberration coefficient is increased (Table 2-8) through the decreasing ray slope h'_f (eqn.(2.40)). From this figure, it is also seen that for a 0.1μm emitter, the minimum virtual source size is 0.1nm or 1Å as set by the diffraction effect. In general, the minimal virtual source size can be inferred from eqn.(2.42) by neglecting the spherical aberration term, so that

$$r_{s\min} = \sqrt{1.76 \times 10^3} \left(\frac{M^2}{K_q^2} \frac{r_a^2}{V_{ex}} + \frac{C_{ch}^2 \Delta V^2}{V_{ex}^3} \right)^{1/4} \approx 42 \left(\frac{r_a^2}{V_{ex}} + \frac{C_{ch}^2 \Delta V^2}{V_{ex}^3} \right)^{1/4} \qquad (2.46)$$

where r_a is in μm, V_{ex} in volt and $r_{s\min}$ in Å.

For emitters with $r_a = 0.1$μm, the chromatic aberration is negligible, so that (2.46) is reduced to

$$r_{s\min} = 42 \frac{r_a^{1/2}}{V_{ex}^{1/4}} \approx 1 \text{ Angstrom} \qquad (2.47)$$
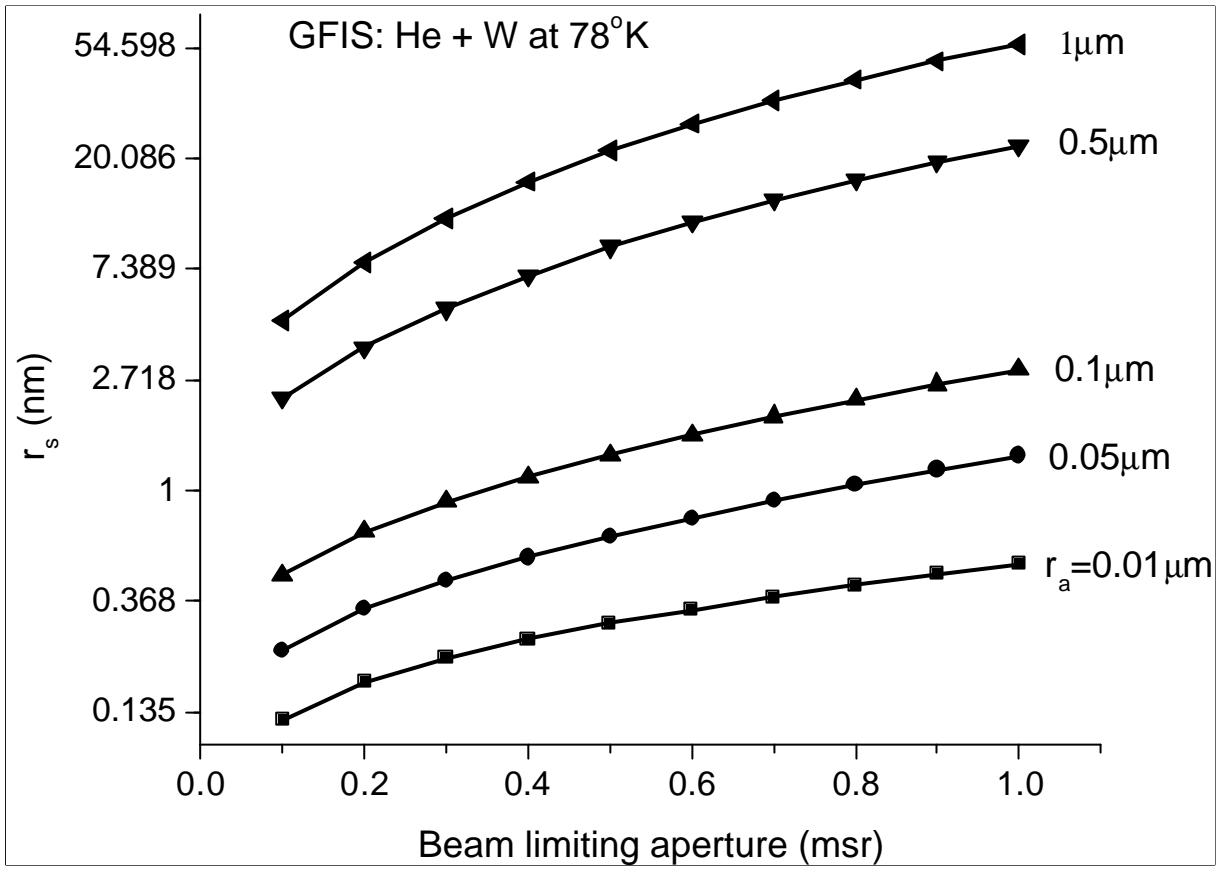
Figure 2-8 r_s as a function of the beam limiting aperture for different emitter radii
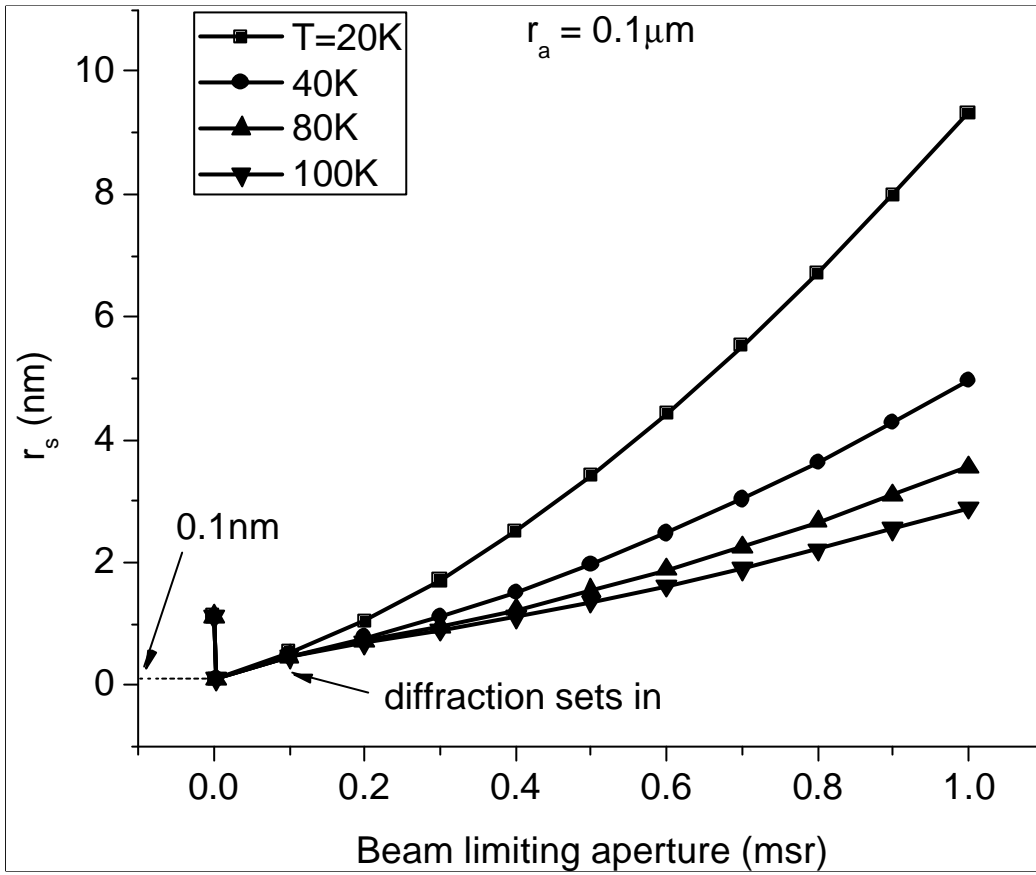
Figure 2-9 Dependence of virtual source size on the tip temperature for a 0.1μm W

emitter with He gas

Table 2-8 The spherical and chromatic aberration coefficients for different tip temperatures (emitter: 0.1μm, n = 0.16, γ = 2.5, E_a = 3V/Å)

	T_t (K)				
	20	40	60	80	100
C_{si} (μm)	1922	989	678	523	429.3
C_{ch} (μm)	94	92.6	91.9	91.3	90.9

2.3.3 Calculation Of Virtual Source Size By Direct Ray Tracing

The algorithm of addition in quadrature (hereinafter referred to as A.I.Q) in last section, although commonly accepted and used to estimate the overall effect from individual contributions, lacks solid mathematical support[73] except in special cases (e.g. for Gaussian distribution). It turns out that the current density distribution in the (virtual) Gaussian image plane is highly non-Gaussian. Consequently, the validity of A.I.Q for the virtual source size needs to be clarified.

On the other hand, higher order (5th rank and above) aberrations need to be considered when the characteristic at large beam-limiting aperture is to be studied, which is obviously the case for the diode region. Let θ be the initial half polar angle (Figure 2-4), the Gaussian image size is

$$r_G = M r_a \sin\boldsymbol{q} \tag{2.48}$$

while the spherical aberration at the Gaussian image plane is

$$r_{sp} = C_s \cdot \tan^3 \boldsymbol{a}_b = C_s \cdot K_{\boldsymbol{q}}^{\;3} \tan^3(\boldsymbol{q}) \tag{2.49}$$

Clearly, the spherical aberration increases more rapidly with θ, we then expect that higher rank aberrations become significant when r_{sp} becomes comparable to r_G, i.e., when

$$\boldsymbol{q}^2 \leq \frac{M r_a}{C_s K_{\boldsymbol{q}}^{\;3}} \tag{2.50}$$

And from (2.44), this corresponds to a beam-limiting aperture Ω of

$$\Omega \doteq p\,\frac{r_a}{C_{si}} \tag{2.51}$$

Substituting $r_a = 0.1\ \mu m$ and $C_{si} = 540\ \mu m$ in (2.51), we have

$$\Omega \le 0.6\,\text{msr} \tag{2.52}$$

In the emission diode region, even with the extraction electrode placed at $z_f = 1cm$ and aperture radius $r_f = 1mm$, the aperture will subtend a solid angle of 31msr at the emitter, so that indeed higher rank aberrations are significant.

Moreover, it should be noted that a fundamental difference exists between field electron emission (FE) and field ion (FI) emission with respect to the source optical properties, including the virtual source size. In the former case, the electron is emitted right out of the tip surface, and its energy spread is thus dependent only on the tip temperature. In the latter case, however, the ions are all generated in a small region beyond the local critical distance (several Å, typically) above the emitter surface (we have already seen the significance of x_c in determining the aberration coefficients), which is called the ionization zone. The ionization zone is extremely narrow. For He ions from W emitter, at the "best image field" $E_a = 4.4V/\text{Å}$ and tip temperature 21°K, the half width of the ionization zone obtained from experiment is only about 0.18Å[15]. So small as it may be, the ion energy spread in this case is 0.8eV due to the large electric field, as compared with the thermal energy of about 3meV. Furthermore, the width of the ionization zone changes with the electric field and tip temperature. As a consequence, the energy spread in GFIS depends on the extraction voltage, tip temperature as well as the imaging gas species.

In this section, the calculation of the GFIS virtual source size is done by the method of direct ray tracing. The advantage of this method is that higher order aberrations are inherently included and that the uncertainty in the addition of individual terms is avoided. While A.I.Q may be valid for small emitters and beam apertures where the aberrations are small and diffraction effect comes into play, the method of direct ray tracing is more appropriate for larger emitters with larger beam apertures. In addition, the method of direct ray tracing can be used to examine the applicability of A.I.Q to large apertures.

In direct ray tracing, the equation of motion for an individual charged particle in the meridianal plane is solved numerically in order to obtain its coordinates and slope at the beam limiting aperture, which can then be used to calculate the virtual image coordinates in arbitrary image plane (such as the Gaussian image plane).

First of all, the ion's initial emission position and direction need to be generated according to appropriate distribution functions.

2.3.3.1   One Dimensional Model of Energy Distribution In GFIS

Tsong and Müller[15] developed a one-dimensional theory for the energy distribution in GFIS, which yields the following distribution function

$$f_E(x) = \frac{\log\left(\frac{2x_m}{x} - 1 + \frac{2x_m}{x}\left(1 - \frac{x}{x_m}\right)^{1/2}\right)}{\log\left(\frac{2x_m}{x_c} - 1 + \frac{2x_m}{x_c}\left(1 - \frac{x_c}{x_m}\right)^{1/2}\right)} \cdot \exp\left(\frac{0.683}{E_a}\left((I - qE_a x)^{3/2} - (I - qE_a x_c)^{3/2}\right)\right) \quad (2.53)$$

where $f_E(x)$ represents the (unnormalized) pdf function of ionization at the height x above the emitter surface; x_c is the critical distance evaluated by eqn.(1.2), which is repeated here

$$x_c = \frac{I - f}{qE_a} \tag{2.54}$$

x_m is the maximum hopping height of a gas molecule rebounding from surface, given by

$$x_m = \frac{3kT_t}{2n_f \boldsymbol{a}_g E_a^2} r_t \tag{2.55}$$

with r_t the emitter apex radius, α_g the gas polarizability and T_t the tip temperature; n_f is an empirical parameter describing the field distribution close to the emitter, i.e. the field strength E near the emitter surface is approximated by

$$E(r) = \left(\frac{r_t}{r}\right)^{n_f} E_a \tag{2.56}$$

For a spherical emitter, $n_f = 2$. And in the original theory, $n_f = 4/3$ is assumed to account for the effect of emitter shank. For the SOC emitters, it is found that choosing n_f between 1.7–1.8 fits a wide range of emitter geometries. In eqn.(2.53), E_a is in V/Å, x_c and x_m are in Å.

The half width as obtained from eqn.(2.53) at $E_a = 4.4$V/Å and $T_t = 21°$K is about 65% wider than the experimental value (taking I = 24.5eV, ϕ = 4.5eV, r_t = 900Å, n_f = 4/3).

One problem with eqn. (2.53) is that the image effect has been neglected. Due to the extremely small width of the ionization zone, this effect, small as it may be, can be of some significance. By including an image potential term of the tunneling electron, we have

$$qE_a x_c = I - \boldsymbol{f} + \frac{q^2}{16 \boldsymbol{p} \boldsymbol{e}_0 x_c} \tag{2.57}$$

solving (2.57) to get

$$x_c = \frac{I - \boldsymbol{f}}{qE_a} - \frac{3.6}{I - \boldsymbol{f}} \tag{2.58}$$

Accordingly, eqn.(2.53) is modified as

$$f_E(x) = \frac{\log\left(\frac{2x_m}{x} - 1 + \frac{2x_m}{x}\left(1 - \frac{x}{x_m}\right)^{1/2}\right)}{\log\left(\frac{2x_m}{x_c} - 1 + \frac{2x_m}{x_c}\left(1 - \frac{x_c}{x_m}\right)^{1/2}\right)} \cdot \exp\left(\frac{0.683}{E_a}\left(\left(I - qE_a x + \frac{3.6}{x}\right)^{3/2} - \left(I - qE_a x_c + \frac{3.6}{x_c}\right)^{3/2}\right)\right) \tag{2.59}$$

with x_c given by (2.58).

With eqn.(2.59), the resulting ionization zone width better fits the experimental data. Actually, for the aforementioned case, the error in the calculated half width of the ionization zone is reduced to 10%.

Figure 2-10 shows the distribution function $f_E(x)$ at three different emitter apex fields 2V/Å, 3V/Å and 4V/Å, for the case of He gas and W emitter at $T_t = 78°K$. It is seen that at higher electric field, the critical distance becomes smaller and the ionization zone moves closer to the emitter surface. Also, as the field increases, the half width of the

ionization zone reduces but more slowly than linearly, so the energy spread actually increases with the field.

The corresponding energy distribution is shown in Figure 2-11, where the collector voltage represents the voltage applied on the collector in a retarding potential experiment so as to let the ion generated at height x stop just before the collector surface, which is given by[15]

$$V_{coll} = \frac{I - f}{q} + \frac{q}{16\pi\varepsilon_0 x_c} + (x - x_c)E_a \qquad (2.60)$$
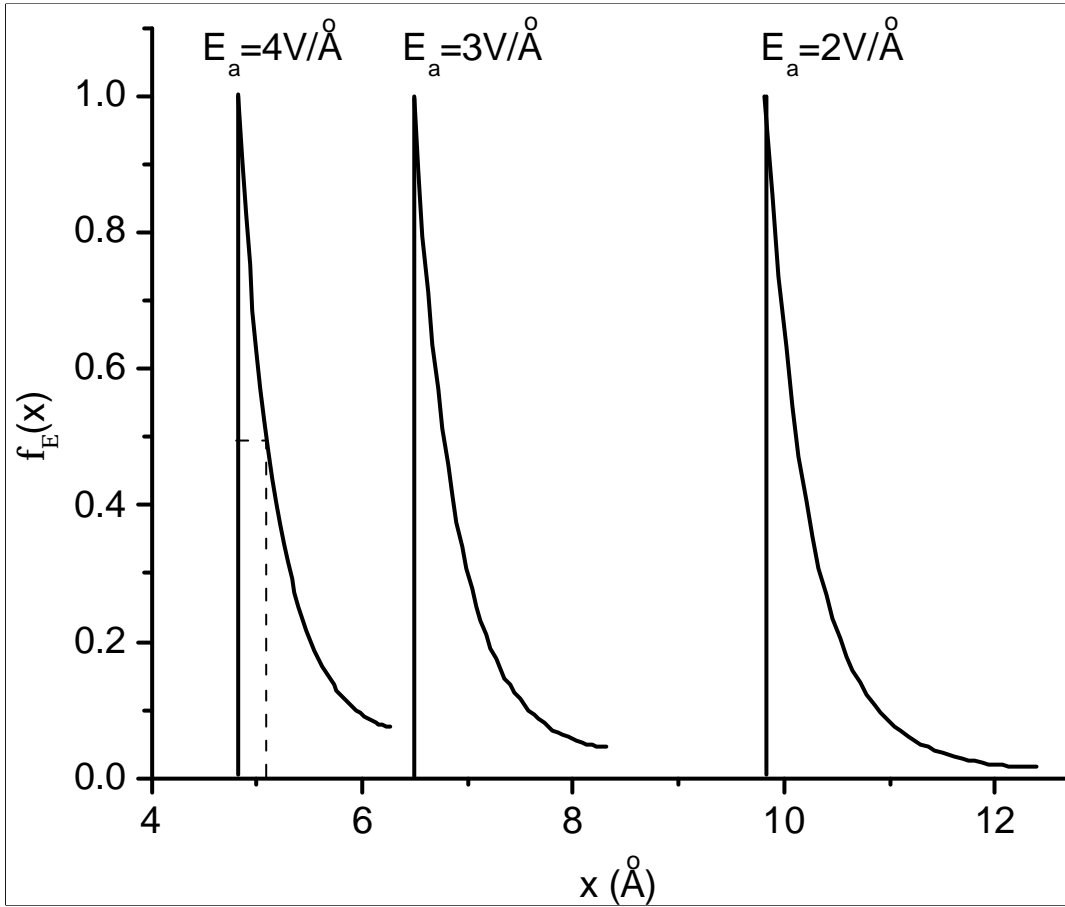
Figure 2-10 Distribution of the height above the emitter surface where ions are generated at different fields. $I = 24.5eV$, $\alpha_g = 0.2\text{Å}^3$, $\phi = 4.5eV$, $r_t = 0.1\mu m$, $T_t = 78°K$.
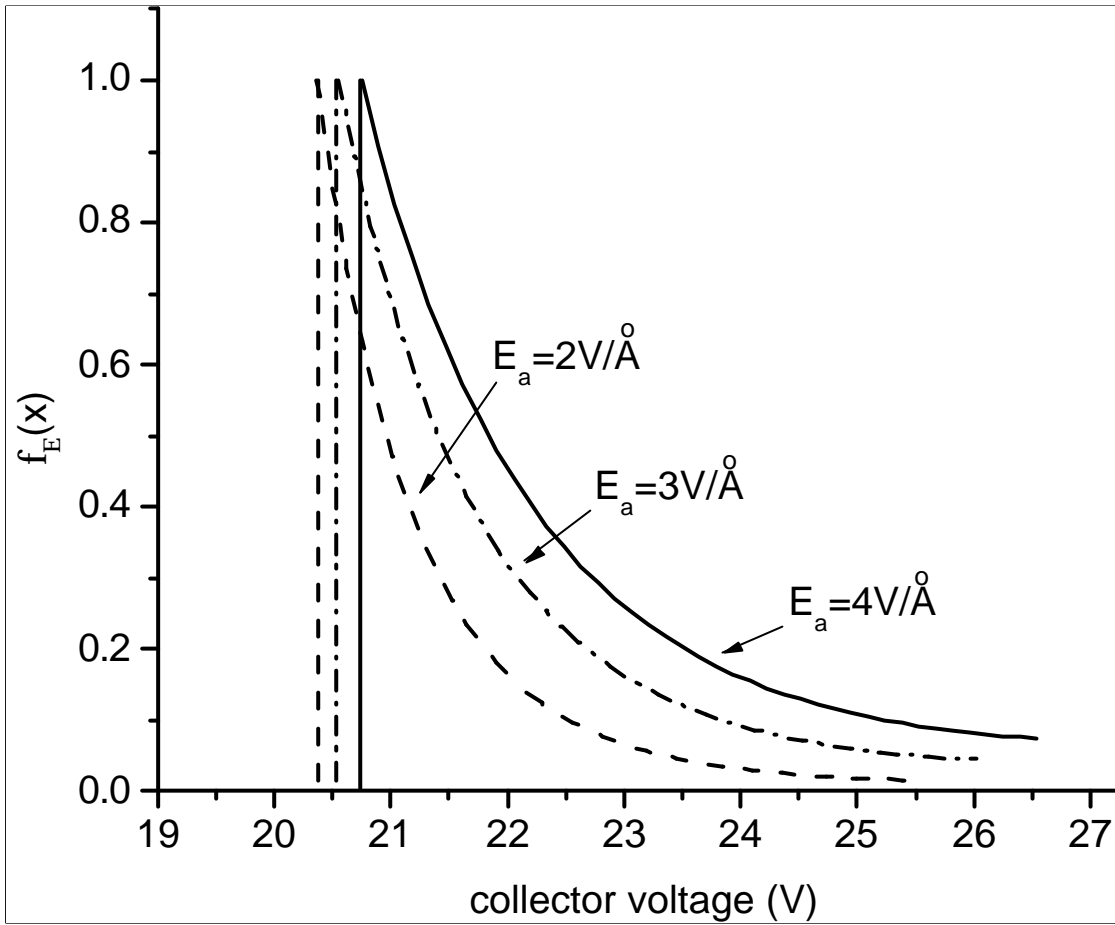
Figure 2-11 Distribution of collector voltage at different fields

2.3.3.2   Setting Up Initial Conditions

With eqn. (2.59), the initial height of emission above the emitter surface can be generated randomly by the following standard procedure.

First we need to get the cumulative distribution function (cdf) P_E for the distribution f_E, which is

$$P_E(X < x) = \frac{\int_{x_c}^{x} f_E(q)dq}{\int_{x_c}^{x_{mm}} f_E(q)dq} \quad (x_c \leq x \leq x_{mm}) \tag{2.61}$$

where the initial height is treated as a random variable X. And the upper limit x_{mm} in (2.61) is chosen to be the smaller one between the maximum hopping height x_m and the root of the equation $I - qE_a x + 3.6/x = 0$, i.e.,

$$x_{mm} = \min\left(\frac{3kT_t}{2n_f a_g E_a^2} r_t, \frac{I}{2qE_a}\left(1+\sqrt{1+14.4\frac{qE_a}{I^2}}\right) \right) \tag{2.62}$$

Let P_E^{-1} be the inverse of function P_E, X can be generated through a random variable U which is uniformly distributed in (0, 1), by

$$X = P_E^{-1}(U) \tag{2.63}$$

Actually, since P_E^{-1} is not available analytically, X is obtained by feeding U to and numerically solving

$$P_E(X) = U \tag{2.64}$$

This procedure is illustrated in Figure 2-12 for an emitter with $r_a = 0.1 \mu m$, $E_a = 4.4 V/\text{Å}$ and at $T_t = 78°K$.

The initial kinetic energy of each ion is taken to be $3kT_t/2$ and the thermal energy spread is negligible (0.04eV at 300°K) compared with the spread in the ionization zone.

We assume that ions are emitted in random directions due to their thermal motions. The emission direction is thus taken to be uniform in $(-\pi/2, \pi/2)$ with respect to the normal direction to the surface.

The initial polar angle about the emitter axis is generated from the surface current density distribution $J(\theta)$. The cdf function for the random polar angle Θ is

$$P_\Theta(0 < \Theta < q) = \frac{\int_0^q J(u) \cdot r^2 \sin u \cdot du}{\int_0^{q_0} J(u) \cdot r^2 \sin u \cdot du} \qquad (0 < q < q_0) \qquad (2.65)$$

where θ_0 is the maximum polar angle of the surface region to be imaged.

If we assume that $J(\theta)$ is uniform within a small region around the emitter apex, (2.65) becomes

$$P_\Theta(0 < \Theta < q) = \frac{1 - \cos q}{1 - \cos q_0} \qquad (2.66)$$

Accordingly,

$$\Theta = \cos^{-1}\left(1 - U\left(1 - \cos q_0\right)\right) \qquad (2.67)$$

81
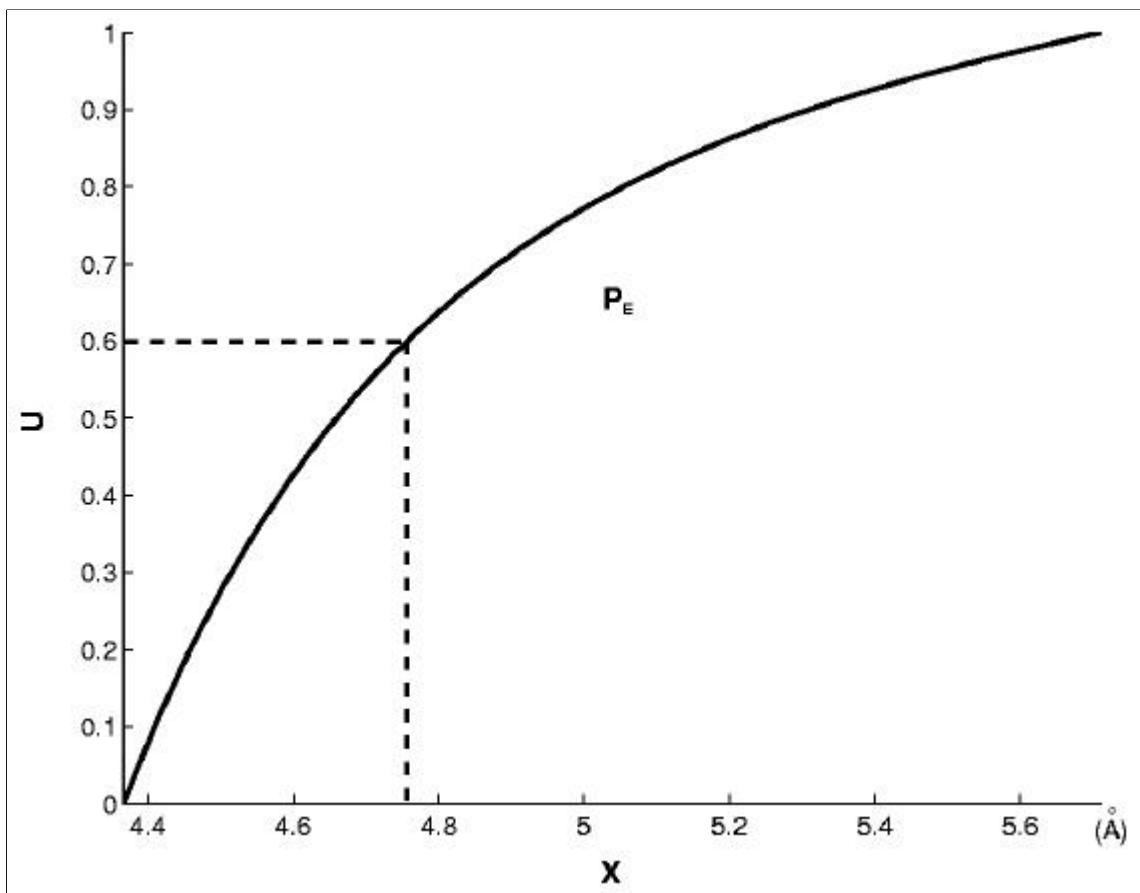
Figure 2-12 cdf function of the energy distribution at $E_a = 4.4V/\text{Å}$, $T_t = 78°K$, $r_t = 0.1\mu m$

2.3.3.3   Equation Of Motion

The equation of motion of ions in the meridianal plane, when expressed in the cylindrical coordinates, is given by

$$\ddot{r} = \boldsymbol{h}_i E_{\boldsymbol{r}}$$
$$\ddot{z} = \boldsymbol{h}_i E_{\boldsymbol{z}}$$

(2.68)

where

$$E_{\boldsymbol{r}} = E_r \sin \boldsymbol{q} + E_{\boldsymbol{q}} \cos \boldsymbol{q}$$
$$E_{\boldsymbol{z}} = E_r \cos \boldsymbol{q} - E_{\boldsymbol{q}} \sin \boldsymbol{q}$$

(2.69)

and E_r, E_θ are given in (2.4).

2.3.3.4   Simulation And Results

For direct ray tracing, we assume that ion emission is limited to the portion of emitter surface around the apex with half angle θ_0. For the following calculation, θ_0 is chosen to be $\leq 10^\circ$. Note that the contribution of ions from high polar angle region is not significant for beam apertures up to several tens of milli-steradian, anyway, which is demonstrated by the simulation. A certain number N random initial polar angles are generated according to (2.67). With each initial angle, 10 ions are created whose initial heights are generated randomly according to (2.61)–(2.63) and whose emission directions are picked randomly in $(-\pi/2, \pi/2)$ with respect to the local surface normal direction. So altogether 10N ions are processed. The initial kinetic energy of each ion is taken to be $3kT_t/2$.

The current distribution at the virtual image plane is first examined. Figure 2-13 shows the current profile for the case of r_a = 0.1μm, T_t = 78°K and beam aperture of 1msr (setting θ_0 = 5°, 172,255 out of 919,419 ions calculated are found to pass through this aperture)—again, it is found that the variation in r_s is small for electric field in the range 2V/Å–4V/Å, and that it is virtually independent of the detailed emitter geometry.

The corresponding current density distribution is shown in Figure 2-14. One can see that J(r) is highly non-Gaussian—it is fairly flat over a wide region, followed by a sharp drop. The ripple in the curve is due to the noise in the data, as a consequence of the stochastic nature of ion generation. Also note that the maximum is not on the axis (r = 0) but located slightly outward.

With the current density distribution, we can also calculate its spatial frequency response (note that J(r) is an even function of r)

$$F(f) = \frac{\int_0^R J(r)\cos(2\boldsymbol{p}rf)dr}{\int_0^R J(r)dr} \tag{2.70}$$

where F(f) is the (normalized) amplitude of the spatial frequency response, R denotes the physical radius of the image.

For the distribution in Figure 2-14, F(f) is plotted in Figure 2-15. The frequency $f_{0.1}$ at which the relative amplitude drops to 0.1 is about 0.27nm^{-1}, corresponding to about 3.7nm, which may be taken as the source size by Rayleigh's criterion[77].

Figure 2-16 shows the comparison of the physical radius of the image as obtained from the direct ray tracing with r_s by A.I.Q, as a check on the consistency of these two methods. Parameters used in the calculation are θ_0 = 10° and N = 20000.

It can be seen that at apertures below 0.8msr, A.I.Q can be applied fairly well with max. relative error of about 30%, which is consistent with the criterion in eqn.(2.52). For apertures larger than 1msr, A.I.Q largely overestimates the source size. The source size by direct ray tracing changes with the aperture almost (or slightly less than) linearly, which is slower than the quadratic changing rate predicted by A.I.Q.
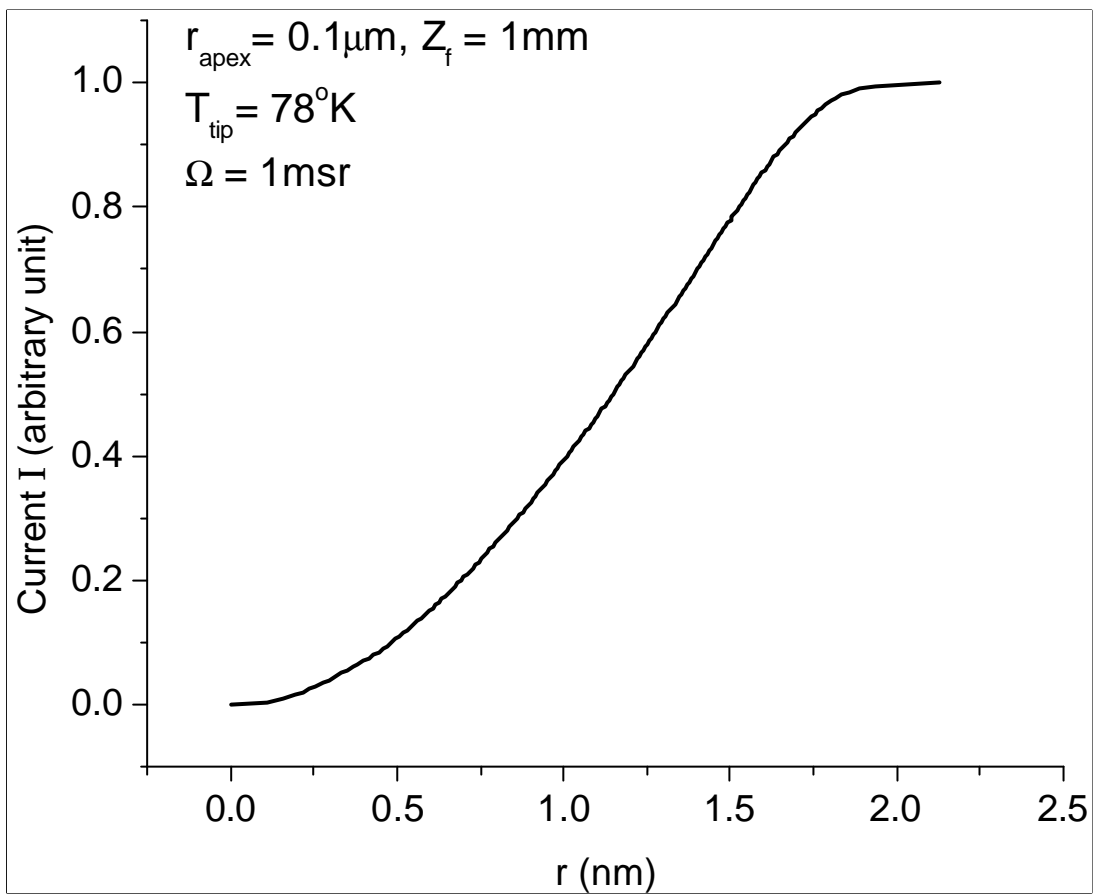
Figure 2-13 Current profile at the Gaussian image plane
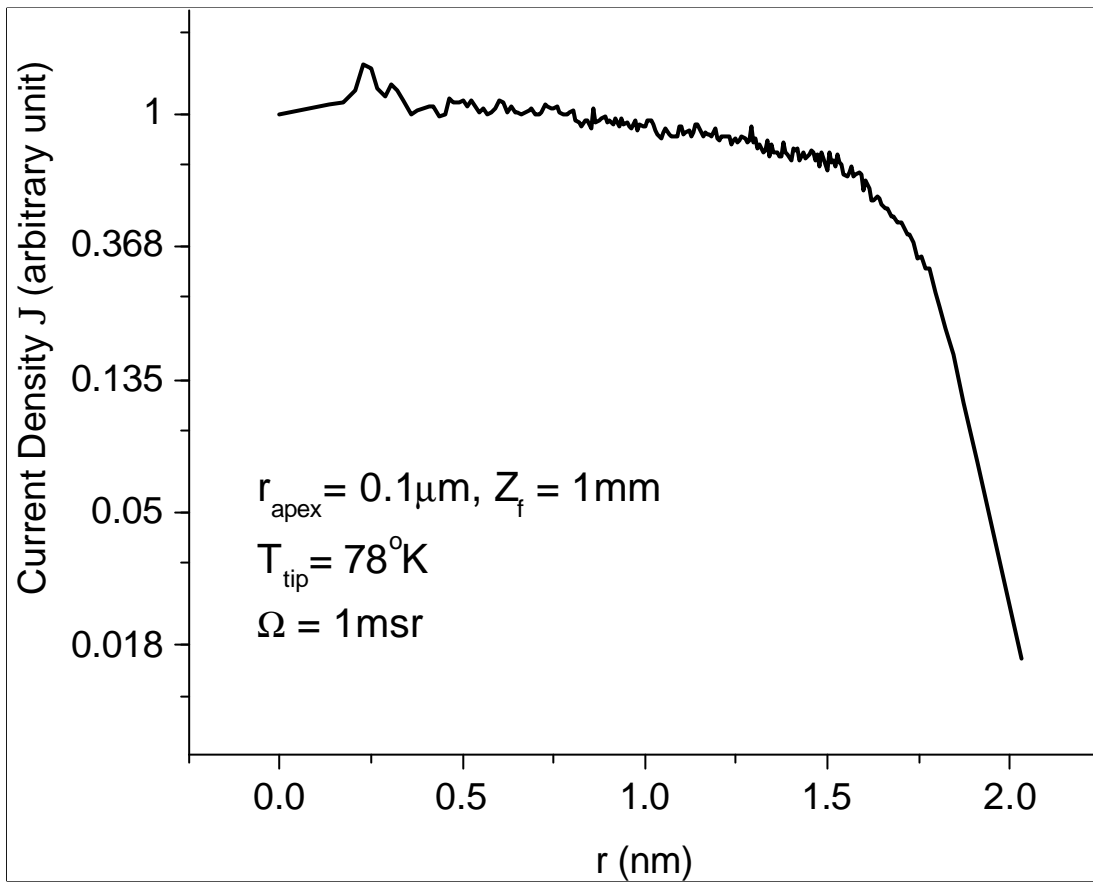
Figure 2-14 Current density distribution at the Gaussian image plane
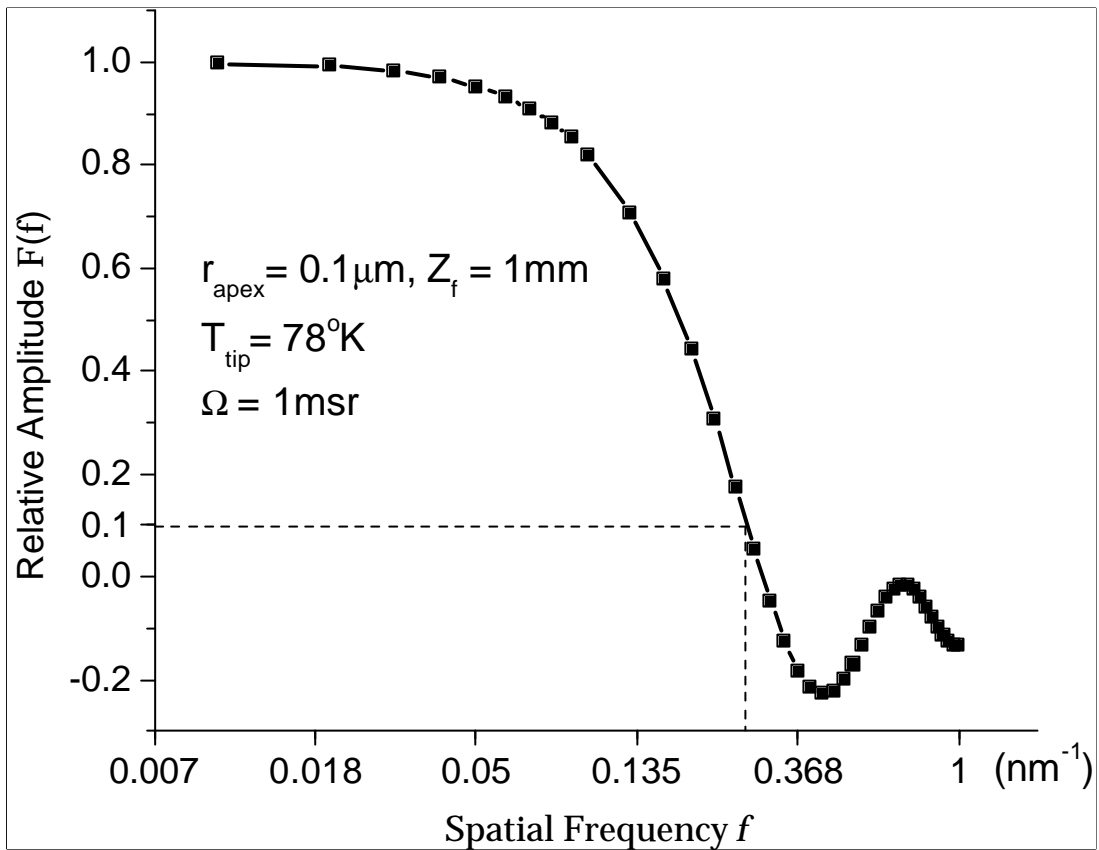
Figure 2-15 Spatial frequency response at the Gaussian image position
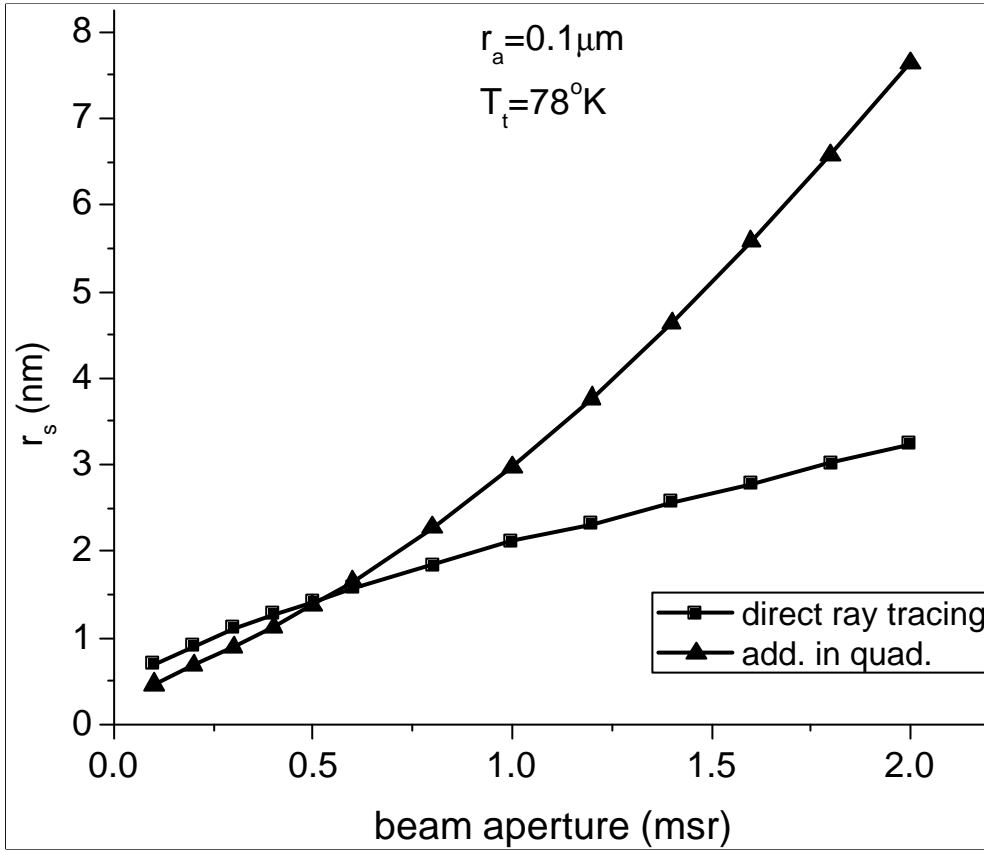
Figure 2-16 Comparison of the virtual source size obtained by direct ray tracing with that from A.I.Q

2.4   Summary

In this chapter, the GFIS source optical properties are studied based on the SOC model which well represents the thermally annealed emitter geometry.

The Gaussian optical properties—linear and angular magnifications—are computed by numerically solving the paraxial ray equations through the Bulirsch-Stoer extrapolation method, which has the advantage of higher precision and less intermediate steps than the well-known Runge-Kutta method.

In the emission diode region, the dominating aberrations at small apertures are spherical and chromatic aberrations. Commonly used aberration integrals either involve 4th order derivative of the potential for spherical aberration and hence are not convenient for numerical calculation or assume that the aperture plane is in field-free region, which is not satisfied in the diode region. This thesis presents two alternative spherical and chromatic aberration integrals. They are shown to reduce to the usual forms under special circumstance. In addition, the derived spherical aberration involves in the integrand only up to the 2nd order derivative of the potential, which thus eases numerical calculation of potential distribution for general emitter topography. One noticeable feature of field ionization is that the critical distance, though very small in magnitude, plays an important role in determining the aberration coefficients, so that one can not simply borrow the results of field electron emission in deriving source optical properties.

Two methods to evaluate the GFIS virtual source size are explored. The first one is by the algorithm of A.I.Q, which is supposed to work at small apertures and emitter radii. The result shows that the source size is largely determined by the emitter radii for given emitter to electrode distance, and that it is roughly independent of the field strength

as well as the detailed emitter geometry within a fairly wide range. The dependence of r_s on the tip temperature shows that r_s increases as the tip temperature decreases, which demonstrates that the GFIS is dominated by spherical aberration (except for very small emitters $z_f/r_a \sim 10^5$).

The second method is through direct ray tracing whereby the ions are all generated within an extremely narrow region beyond the critical distance above the emitter surface. By randomly generating initial conditions according to appropriate distribution functions and solving the equation of motion, the individual ion trajectory can be traced and the projected coordinates at the image plane can be calculated. The simulation result shows that the current density distribution at the Gaussian image plane is fairly flat over a wide range, followed by a sharp drop. Moreover, it is seen that A.I.Q is approximately valid at small apertures, while at large apertures, it predicts too fast the growth of source size with the aperture.

Chapter 3   Emission Current In GFIS

We next proceed to an analysis of the ion generation process in GFIS, focusing on the gas supply mechanism under various tip conditions. It is shown that a relatively simple model solely based on the gas supply mechanism, regardless of the complication due to the dynamical behavior of gas molecules and gas–surface interactions, would come up with emission currents in reasonable agreement with experiments. And this model gives better results than previous attempts to explain GFIS behavior[75, 76].

3.1   Gas Supply In GFIS

Field ionization depends strongly on the electric field. On one hand, the penetration probability of the tunneling electron into the emitter depends exponentially on the field strength, which, in the form derived by Müller[74], is

$$D(x_c) = \exp\left(-0.455\sqrt{I - 7.6E^{1/2}}\,\frac{I - \phi}{E}\right) \tag{3.1}$$

where I and ϕ are in eV and E is in V/Å. Due to the strong curvature of the emitter apex, the ionization of gas molecules is confined to a small region around the emitter apex, i.e. the ionization zone, where virtually all ions are generated.

On the other hand, measurement of the emission current demonstrated that the supply function—the total number of particles per unit surface per unit time hitting on the emitter—in GFIS is larger by a factor of ~10 than that in the field-free case[2]. The reason is that in an inhomogeneous electric field as that around the tip, the gas molecules are attracted toward the emitter apex (where the field is the largest) due to the dipole force that originates from the dipole moment of the molecule intrinsic or induced by the

strong field. Study of the current‑voltage characteristic of GFIS exposes two distinctive regimes[89]. In the field-limited regime where the field is relatively low, the gas distribution in the ionization zone is approximately in equilibrium and the emission current rises steeply with the electric field. As the field becomes so high that nearly all molecules into the ionization zone are ionized before they could escape the current is limited by the gas supply into the ionization zone, which rises mildly with the field.

Southon[90] calculated the supply functions for spherical and cylindrical emitters, whose results are given below

spherical emitter:

$$
\begin{aligned}
Y_{sp} &= \frac{P_g}{\left(2\boldsymbol{p}mkT_g\right)^{1/2}}\left[\exp\left(-\frac{\boldsymbol{a}_g E^2}{2kT_g}\right)+\left(\frac{\boldsymbol{pa}_g E^2}{2kT_g}\right)^{1/2}erf\sqrt{\frac{\boldsymbol{a}_g E^2}{2kT_g}}\right] \\
&\approx \frac{P_g}{\left(2\boldsymbol{p}mkT_g\right)^{1/2}}\left(\frac{\boldsymbol{pa}_g E^2}{2kT_g}\right)^{1/2}, \quad \left(\frac{\boldsymbol{a}_g E^2}{2kT_g}>1\right)
\end{aligned}
\tag{3.2}
$$

cylindrical emitter:

$$
\begin{aligned}
Y_{cy} &= \frac{P_g}{(2\boldsymbol{p}mkT_g)^{1/2}}\left(\sqrt{\frac{2\boldsymbol{a}_g E^2}{\boldsymbol{p}kT_g}}+e^{\frac{\boldsymbol{a}_g E^2}{2kT_g}}\left(1-erf\left(\sqrt{\frac{\boldsymbol{a}_g E^2}{2kT_g}}\right)\right)\right) \\
&\approx \frac{P_g}{(2\boldsymbol{p}mkT_g)^{1/2}}\left(\frac{2\boldsymbol{a}_g E^2}{\boldsymbol{p}kT_g}\right)^{1/2}, \quad \left(\frac{\boldsymbol{a}_g E^2}{2kT_g}>1\right)
\end{aligned}
\tag{3.3}
$$

where P_g and T_g are the gas pressure and temperature, respectively.

A real emitter, however, has a conical shank with an approximately spherical cap at the end. As a result, gas molecules can be supplied both from space and along the shank[91, 92], and the latter dominates when operating at cryogenic temperatures[93] or

in supply-limited regime. To demonstrate this last point, we examine the emission current as limited by the supply function for a spherical emitter

$$i \approx 4 \boldsymbol{p} \, r_a^{\,2} q Y \qquad (3.4)$$

substituting eqn. (3.2) into (3.4), and taking Ar as an example with $r_a = 0.1 \mu m$, $E_a = 2.2 V/\text{Å}$ (best image field for Ar), $P_g = 5 \times 10^{-3}$ torr, $T_g = 300°K$, we will get $i \approx 1.8 \times 10^{-9}$A which is lower by a factor of 30~40 than the experimental result[13]. Considering that eqn. (3.4) is an upper limit, this indicates that in the imaging region, the supply from shank dominates in the supply function.

Under collisions with the emitter a large part of impinging gas molecules lose their energies and are trapped in the vicinity of the emitter, since their kinetic energies are less than the local polarization potential energy $\alpha_g E^2/2$. When the field is relatively low so that ionization is negligible, the gas distribution is in equilibrium and the gas density increases along the shank toward the emitter apex due to the dipole attraction effect. As the field increases to where the ionization becomes important, the gas deviates from the equilibrium distribution, mainly in the ionization zone, until the source enters supply limited regime and the gas density in the ionization zone is reduced to a magnitude comparable to that in an area remote from the tip[75]. Meanwhile, the region along the shank beyond the ionization zone does not suffer from as severe an ionization loss, due to the strong dependence of ionization rate on the field strength, and the gas may keep at quasi-equilibrium through particle-surface interactions with the emitter. Under the dipole attraction force, the flow of these gas molecules constitutes the major part of gas supply into the ionization zone (Figure 3-1).

94
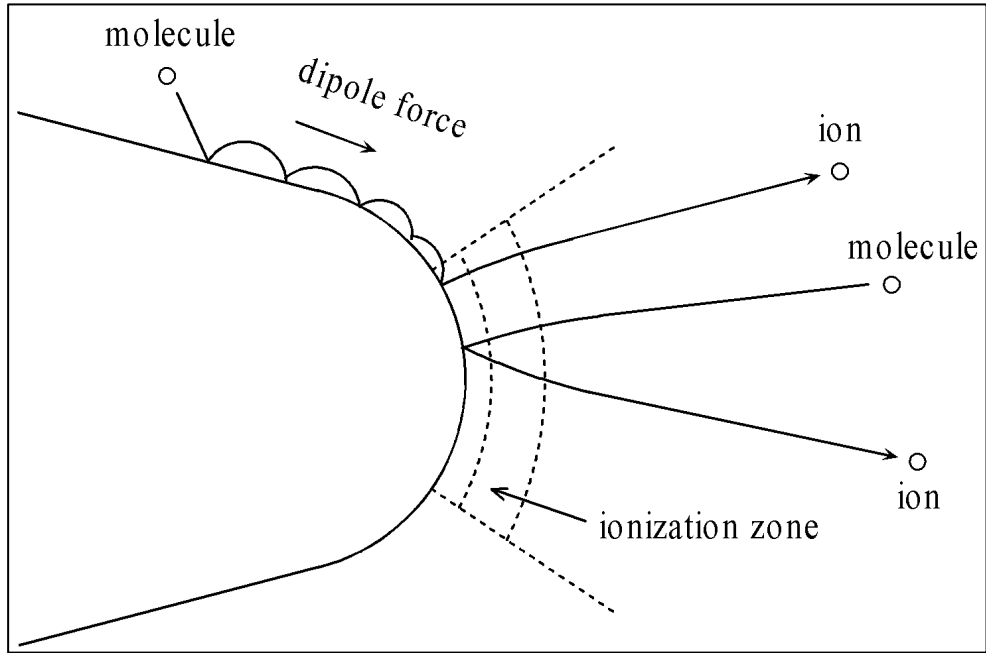
Figure 3-1 Schematic diagram of gas supply to the ionization zone

Consider a molecule moving with velocity v in the ionization zone. If v is very large such that the displacement between consecutive collisions with the emitter surface $\Delta z \gg r_a$, then this molecule is not likely to be one of the trapped molecules (with low kinetic energies) drifting slowly along the shank. In other words, those high velocity molecules in the ionization zone are essentially fed there from free space through direct dipole attraction. On the other hand, a molecule with low velocity is much more likely supplied via the shank than from free space, because the latter would require rather precise initial conditions due to the small area of the ionization zone.

Applying the above argument, we could then estimate the drift flux along the shank into the ionization zone.

Note that at the edge of the ionization zone, those low velocity molecules are located within the height of r_a above the emitter surface, the flux of these molecules into the ionization zone is then given by

$$Z_{sh} = 2\pi r_a{}^2 \cdot \bar{u}_d \cdot n_g e^{a_g E^2 / 2kT_t} \tag{3.5}$$

where n_g is the gas density in the remote area, E is the local electric field at the edge of the ionization zone and $\bar{v}_d$ is the mean drift velocity of molecules along the shank. In deriving (3.5), we have assumed complete thermal accommodation, i.e. the gas distribution along the shank beyond the ionization zone is in equilibrium with the emitter.

To see how $\bar{v}_d$ depends on the exterior half angle of the shank, we assume a conical emitter shank structure(Figure 3-2).

96
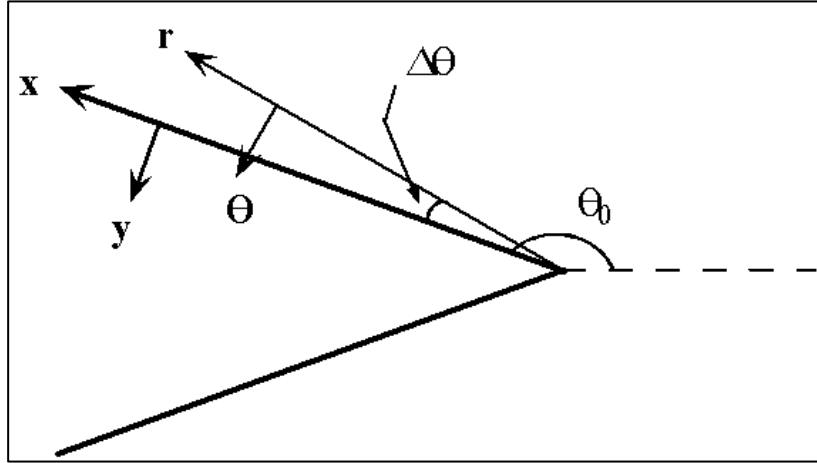
Figure 3-2 Conical emitter shank with exterior half angle θ_0

By choosing appropriate boundary conditions, the potential of a conical emitter with exterior half angle θ_0 can be expressed as

$$V(r,\boldsymbol{q}) = -A r^n \cdot P_n(\cos\boldsymbol{q}) \tag{3.6}$$

where $A > 0$ is a constant determined by the boundary condition. The cone index n satisfies $P_n(\cos\theta_0) = 0$.

The dipole force on the molecule is

$$F_r = \frac{1}{2}\boldsymbol{a}_g \frac{\partial E^2}{\partial r} = \boldsymbol{a}_g \frac{\partial V}{\partial r} \cdot \frac{\partial^2 V}{\partial r^2} + \frac{\boldsymbol{a}_g}{r}\frac{\partial V}{\partial \boldsymbol{q}} \cdot \frac{\partial}{\partial r}\left(\frac{1}{r}\frac{\partial V}{\partial \boldsymbol{q}}\right)$$

$$F_q = \frac{1}{2}\frac{\boldsymbol{a}_g}{r}\frac{\partial E^2}{\partial \boldsymbol{q}} = \frac{\boldsymbol{a}_g}{r}\frac{\partial V}{\partial r} \cdot \frac{\partial^2 V}{\partial r \partial \boldsymbol{q}} + \frac{\boldsymbol{a}_g}{r^2}\frac{\partial V}{\partial \boldsymbol{q}} \cdot \frac{\partial}{\partial \boldsymbol{q}}\left(\frac{1}{r}\frac{\partial V}{\partial \boldsymbol{q}}\right) \tag{3.7}$$

By expanding the potential (3.6) into the polynomial of $\Delta\theta = \theta - \theta_0$ and substituting in (3.7), keeping only the linear terms, we have

97

$$F_r = (-\boldsymbol{x}_1 - \boldsymbol{x}_2 \cdot \Delta\boldsymbol{q}) \cdot r^{2n-3}$$
$$F_q = (\boldsymbol{z}_1 + \boldsymbol{z}_2 \cdot \Delta\boldsymbol{q}) \cdot r^{2n-3}$$

(3.8)

where

$$\boldsymbol{x}_1 = A^2 \cdot \frac{\boldsymbol{a}_g \cdot n^2(1-n)}{\sin^2 \boldsymbol{q}_0} \cdot \left(P_{n-1}(\cos\boldsymbol{q}_0)\right)^2 > 0$$

$$\boldsymbol{x}_2 = A^2 \cdot \frac{\boldsymbol{a}_g \cdot n^2(n-1)}{\sin^2 \boldsymbol{q}_0} \cdot \frac{2\cos\boldsymbol{q}_0}{\sin\boldsymbol{q}_0}\left(P_{n-1}(\cos\boldsymbol{q}_0)\right)^2 > 0$$

$$\boldsymbol{z}_1 = -A^2 \cdot \boldsymbol{a}_g \cdot \frac{n^2 \cos\boldsymbol{q}_0}{\sin^3 \boldsymbol{q}_0}\left(P_{n-1}(\cos\boldsymbol{q}_0)\right)^2 > 0$$

$$\boldsymbol{z}_1 = A^2 \cdot \boldsymbol{a}_g \cdot n^2 \frac{3-(2+n)\sin^2\boldsymbol{q}_0}{\sin^4\boldsymbol{q}_0}\left(P_{n-1}(\cos\boldsymbol{q}_0)\right)^2 > 0$$

The equation of motion in the X-Y plane is:

$$m\ddot{x} = F_r \cos\Delta\boldsymbol{q} - F_q \sin\Delta\boldsymbol{q}$$
$$m\ddot{y} = F_r \sin\Delta\boldsymbol{q} + F_q \cos\Delta\boldsymbol{q}$$

(3.9)

Let x = $x_0+\Delta x$, r = $r_0+\Delta r$, noting that r_0 = x_0 and assuming $\Delta x \ll x_0$, y $\ll x_0$ and $\Delta\theta \ll 1$,

(3.9) can be simplified as

$$m\frac{d^2}{dt^2}\Delta x = -\boldsymbol{x}_1 x_0^{2n-3} + (3-2n)\boldsymbol{x}_1 x_0^{2n-4} \cdot \Delta x + (\boldsymbol{z}_1 - \boldsymbol{x}_2)x_0^{2n-4} \cdot y + O(\Delta x^2 + \Delta x \cdot y + y^2)$$

$$m\frac{d^2 y}{dt^2} = \boldsymbol{z}_1 x_0^{2n-3} - (3-2n)\boldsymbol{z}_1 x_0^{2n-4} \cdot \Delta x + (\boldsymbol{z}_2 - \boldsymbol{x}_1)x_0^{2n-4} \cdot y + O(\Delta x^2 + \Delta x \cdot y + y^2)$$

(3.10)

The lowest order approximation can be obtained by keeping only the constant terms in

(3.10), which yields

$$\Delta x(t) = \mathbf{u}_0 \sin \mathbf{j} \cdot t - \frac{\mathbf{x}_1}{2m} x_0^{2n-3} \cdot t^2$$

$$y(t) = -\mathbf{u}_0 \cos \mathbf{j} \cdot t + \frac{\mathbf{z}_1}{2m} x_0^{2n-3} \cdot t^2$$

(3.11)

where υ_0 is the initial velocity, φ is the angle between $\mathbf{u_0}$ and the normal direction to the shank. The flight time between two consecutive collisions is determined by setting y(t)=0

$$t_d = \frac{2m}{\mathbf{z}_1} x_0^{3-2n} \cdot \mathbf{u}_0 \cos \mathbf{j}$$

(3.12)

The corresponding drift velocity for this particular molecule (υ_0, φ) is defined as

$$\mathbf{u}_d \equiv \frac{\Delta x(t_d)}{t_d} = \mathbf{u}_0 \sin \mathbf{f} - \frac{\mathbf{x}_1}{\mathbf{z}_1} \mathbf{u}_0 \cos \mathbf{j} = \mathbf{u}_0 \sin \mathbf{j} + \frac{\sin \mathbf{q}_0}{\cos \mathbf{q}_0} (1-n) \cdot \mathbf{u}_0 \cos \mathbf{j}$$

(3.13)

To get the mean drift velocity, assuming uniform angular M-B distribution for the rebound molecules,

$$f(\mathbf{u}_0, \mathbf{j}) = \frac{m}{\mathbf{p} k T_t} \cdot \mathbf{u}_0 e^{-\frac{m}{2kT_t} \mathbf{u}_0^2}$$

(3.14)

we then get

$$\bar{\mathbf{u}}_d = \int_{-\mathbf{p}/2}^{\mathbf{p}/2} d\mathbf{j} \int_0^{\infty} \mathbf{u}_d \cdot f(\mathbf{u}_0, \mathbf{j}) d\mathbf{u}_0$$

$$= \left(\frac{2kT_t}{\mathbf{p}m} \right)^{1/2} \frac{(1-n)\sin \mathbf{q}_0}{\cos \mathbf{q}_0}$$

(3.15)

Note that $\bar{\upsilon}_d$ is negative ($\cos \theta_0 < 0$), meaning the molecules are drifting towards the emitter apex. Also note that the ratio of $\bar{\upsilon}_d$ with the mean thermal velocity υ_{th} is

99

$$\frac{\bar{\boldsymbol{u}}_d}{\boldsymbol{u}_{th}} = \frac{(1-n)\sin \boldsymbol{q}_0}{2\cos \boldsymbol{q}_0} \tag{3.16}$$

By substituting (3.15) into (3.5), we will get the drift flux for a conical shank as

$$Z_{sh} = (1-n)\left|\frac{\sin \boldsymbol{q}_0}{\cos \boldsymbol{q}_0}\right| \cdot 4\boldsymbol{p}r_a^2 \cdot \frac{p_g}{\sqrt{2\boldsymbol{p}\, mkT_t}} \cdot \exp\left(\frac{\boldsymbol{a}_g E^2}{2kT_t}\right) \tag{3.17}$$

For common emitters, $\theta_0 \sim 170°$ ($n \approx 0.2$) and

$$Z_{sh} = 1.5 r_a^2 \cdot \frac{p_g}{\sqrt{2\boldsymbol{p}\, mkT_t}} \cdot e^{\boldsymbol{a}_g E^2 / 2kT_t} \tag{3.18}$$

For He gas, let $P_g = 10^{-3}$ torr, $r_t = 0.1$ um, $T_t = 78K$ and $E = 300MV/cm$, we get $Z_{sh} \approx 3.3 \times 10^{12}$ sec^{-1}, corresponding to an emission current of 0.5uA.

3.2   Emission Current Calculation For SOC GFIS

We next calculate the emission current of GFIS for SOC emitters. The following assumptions are made.

- The tip temperature is not so low as to make a liquid film of the imaging gas molecules to form on the emitter surface. (For He gas, it requires $T_t = 4°K$)

- In the supply-limited regime, the gas distribution along the shank beyond the ionization zone is in equilibrium with the emitter because of the exponential dependence of the ionization rate on field strength.

- Imaging gas and emitter are at the same temperature.

The second assumption is the most critical and its validity implies that the drift velocity $\bar{\upsilon}_d \ll$ the thermal velocity υ_{th}. From (3.16), we can see that for n ≈ 0.2, $\bar{\upsilon}_d$ is only about 7% of υ_{th}.

3.2.1 Gas Flux Along The Emitter Shank

The equation of motion of gas molecules in the meridianal plane under the dipole attraction force is

$$\ddot{r} - r\dot{\boldsymbol{q}}^2 = \frac{\boldsymbol{a}_g}{2m}\frac{\partial E^2}{\partial r}$$

$$r\ddot{\boldsymbol{q}} + 2\dot{r}\dot{\boldsymbol{q}} = \frac{\boldsymbol{a}_g}{2mr}\frac{\partial E^2}{\partial \boldsymbol{q}}$$

(3.19)

where (r, θ) is the polar coordinate with the origin at the SOC core center. Defining $z_1 \equiv r/r_a$, $z_2 \equiv dz_1/dt$, $z_3 \equiv \theta$, $z_4 \equiv dz_3/dt$ and substituting the SOC field (2.4), eqn.(3.19) can be transformed into a set of first-order differential equations

$$\dot{z}_1 = z_2$$

$$\dot{z}_2 = z_1 z_4^{\ 2} + \frac{\boldsymbol{a}_g E_a^{\ 2}}{mr_a^{\ 2}} \cdot h_1\left(n,\boldsymbol{g},z_1,z_3\right)$$

$$\dot{z}_3 = z_4$$

$$\dot{z}_4 = \frac{1}{z_1}\left(-2z_2 z_4 + \frac{\boldsymbol{a}_g E_a^{\ 2}}{mr_a^{\ 2}} \cdot h_2\left(n,\boldsymbol{g},z_1,z_3\right)\right)$$

(3.20)

where

$$h_1\left(n,\boldsymbol{g},z_1,z_3\right)=\frac{1}{z_1^{\,2}\cdot\left(n+\dfrac{n+1}{\boldsymbol{g}^{2n+1}}\right)^2}\left\{P_n^{\,2}\left(n^2(n-1)z_1^{\,2n-1}-\frac{(1+n)^2(n+2)}{\boldsymbol{g}^{2+4n}}z_1^{\,-3-2n}-\frac{3n(1+n)}{\boldsymbol{g}^{1+2n}}z_1^{\,-2}\right)\right.$$

$$\left.+\frac{n^2\left(P_{n-1}-\cos z_3\cdot P_n\right)^2}{1-\cos^2 z_3}\left((n-1)z_1^{\,2n-1}-\frac{n+2}{\boldsymbol{g}^{2+4n}}z_1^{\,-3-2n}+\frac{3}{\boldsymbol{g}^{1+2n}}z_1^{\,-2}\right)\right\}$$

$$h_2\left(n,\boldsymbol{g},z_1,z_3\right)=\frac{\left(\cos z_3\cdot P_n-P_{n-1}\right)}{z_1\left(n+\dfrac{n+1}{\boldsymbol{g}^{2n+1}}\right)^2}\cdot\frac{n}{\sqrt{1-\cos^2 z_3}}\cdot\left\{P_n\cdot\left(nz_1^{\,n-1}+\frac{n+1}{\boldsymbol{g}^{1+2n}}z_1^{\,-2-n}\right)^2\right.$$

$$\left.-\frac{n}{1-\cos^2 z_3}\left(\frac{1}{\boldsymbol{g}^{1+2n}}z_1^{\,-2-n}-z_1^{\,n-1}\right)^2\left((1-n)\left(P_{n-2}-2\cos z_3\cdot P_{n-1}\right)+\left(1-n\cos^2 z_3\right)P_n\right)\right\}$$

and the initial conditions are (Figure 3-3)

$$z_1(t=0)=\frac{r(0)}{r_a}$$

$$z_3(0)=\boldsymbol{q}(0)$$

$$z_2(0)=\boldsymbol{u}_0\left(\frac{\cos\boldsymbol{j}}{r_a}\cdot\frac{E_r\left(z_1(0),z_3(0)\right)}{E\left(z_1(0),z_3(0)\right)}-\frac{\sin\boldsymbol{j}}{r_a}\cdot\frac{E_q\left(z_1(0),z_3(0)\right)}{E\left(z_1(0),z_3(0)\right)}\right) \qquad (3.21)$$

$$z_4(0)=\boldsymbol{u}_0\left(\frac{\cos\boldsymbol{j}}{r_a z_1(0)}\cdot\frac{E_q\left(z_1(0),z_3(0)\right)}{E\left(z_1(0),z_3(0)\right)}+\frac{\sin\boldsymbol{j}}{r_a z_1(0)}\cdot\frac{E_r\left(z_1(0),z_3(0)\right)}{E\left(z_1(0),z_3(0)\right)}\right)$$

where t = 0 refers to the moment a rebound molecule just leaves the emitter surface.
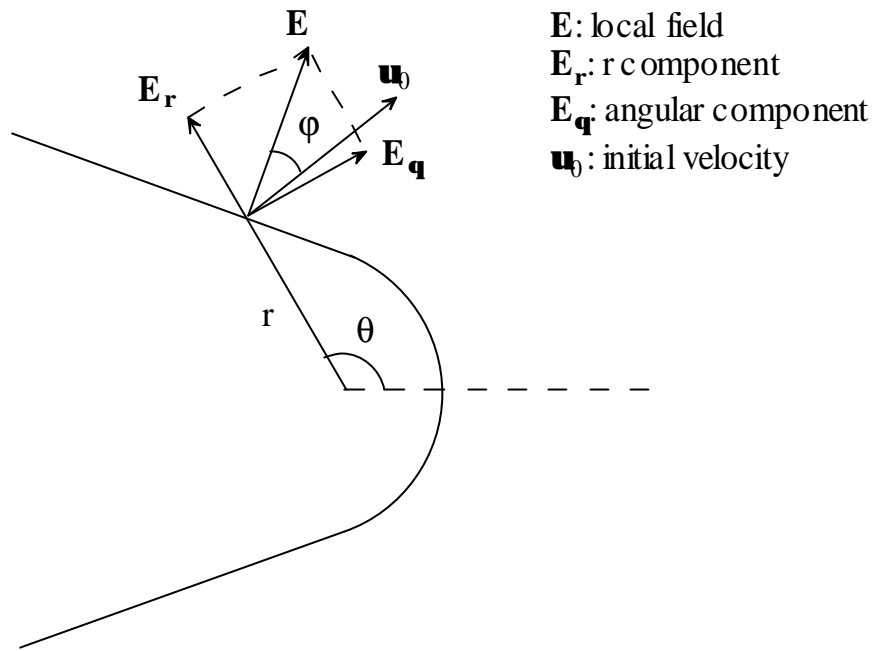
Figure 3-3 Schematic diagram of polar coordinates and initial conditions in SOC model

In order to get the drift velocity, we will need to calculate the drift distance between two consecutive collisions, so that the evaluation of eqn.(3.20) must terminate when the molecule hits the surface again. By noting that the emitter is an equipotential surface, we see that during the flight time t_d, z_1 and z_2 must satisfy

$$\left(g^n z_1^{\,n} - g^{-n-1} z_1^{\,-n-1} \right) \cdot P_n \left(\cos z_3 \right) \geq g^n - g^{-n-1} \tag{3.22}$$

By solving eqn. (3.20) numerically subject to (3.22), we can get the axial drift velocity $\upsilon_{d,z}$

$$\boldsymbol{u}_{d,z} \equiv \frac{\Delta z}{t_d} = \frac{r_a}{t_d} \left(z_1(t_d) \cdot \cos z_3(t_d) - z_1(0) \cdot \cos z_3(0) \right) \tag{3.23}$$

where Δz denotes the axial displacement between two consecutive collisions with the emitter.

Note that $\upsilon_{d,z}$ as obtained is a function of the molecule's initial velocity and ϕ. Averaging $\upsilon_{d,z}$ over the distribution (3.14), we can get the mean axial drift velocity $\bar{\upsilon}_{d,z}$ as

$$\bar{\boldsymbol{u}}_{d,z} = \frac{1}{\boldsymbol{p}} \int_{-\boldsymbol{p}/2}^{\boldsymbol{p}/2} d\boldsymbol{f} \int_0^\infty \boldsymbol{u}_{d,z}(x,\boldsymbol{f}) \cdot e^{-x} dx \tag{3.24}$$

We then define the mean drift velocity $\bar{\boldsymbol{u}}_d$ along the shank as

$$\bar{\boldsymbol{u}}_d(r,\boldsymbol{q}) \equiv \frac{1}{\left(1+\boldsymbol{r}'^2\right)^{1/2}} \bar{\boldsymbol{u}}_{d,z}(r,\boldsymbol{q}) = \frac{E(r,\boldsymbol{q})}{E_r(r,\boldsymbol{q})\cdot\sin\boldsymbol{q} + E_q(r,\boldsymbol{q})\cdot\cos\boldsymbol{q}} \cdot \bar{\boldsymbol{u}}_{d,z}(r,\boldsymbol{q}) \tag{3.25}$$

where ρ' is the local tangential (with respect to z) of the emitter surface.

Next, we calculate the average hopping height h_c of molecules. In doing so, eqn. (2.56) is used, i.e. the field distribution in the vicinity of the emitter is approximated by $E(r) \propto \dfrac{1}{r^{n_f}}$. The hopping height $h(KE)$ of a molecule with kinetic energy KE at the surface is then given by

$$h(KE) = \frac{KE}{n_f \boldsymbol{a}_g E^2} r_t \tag{3.26}$$

where r_t is the radius of curvature as given in eqn. (2.3).

Averaging h(KE) over KE using the distribution (3.14) to yield

104

$$h_c = \frac{2}{\sqrt{\boldsymbol{p}}} \frac{r_t k T_t}{n_f \boldsymbol{a}_g E^2} \int_0^\infty x^{3/2} e^{-x} dx$$

$$= \frac{3}{2} \frac{k T_t}{n_f \boldsymbol{a}_g E^2} \cdot r_t \qquad\qquad (3.27)$$

The gas flux along the shank is then given by

$$Z_{sh} = 2\boldsymbol{pc} \cdot r_t \cdot h_c \cdot \frac{P_g}{kT_t} e^{\boldsymbol{a}_g E^2 / 2kT_t} \cdot \bar{\boldsymbol{u}}_d = \frac{3\boldsymbol{cp} P_g}{n_f \boldsymbol{a}_g E^2} r_t^2 \cdot e^{\boldsymbol{a}_g E^2 / 2kT_t} \cdot \bar{\boldsymbol{u}}_d \qquad (3.28)$$

where $\chi = (r \cdot \sin\theta) / r_a \approx 1$ is determined by the position along the shank where the flux occurs.

Eqn.(3.28) may be further modified by noting that only molecules with hopping heights greater than the critical distance x_c can be ionized. The effective gas density is then given by

$$n_{\textit{eff}} = \frac{P_g}{kT_t} e^{\boldsymbol{a}_g E^2 / 2kT_t} \int_{KE_c / kT_t}^\infty \frac{2}{\sqrt{\boldsymbol{p}}} \cdot \sqrt{x} \cdot e^{-x} dx$$

$$= \left(\frac{2}{\sqrt{\boldsymbol{p}}} \frac{KE_c}{kT_t} e^{-KE_c / kT_t} + 1 - erf\left(\sqrt{\frac{KE_c}{kT_t}} \right) \right) \cdot \frac{P_g}{kT_t} e^{\boldsymbol{a}_g E^2 / 2kT_t} \qquad (3.29)$$

where KE_c is the kinetic energy on the emitter surface of a gas molecule that has the maximum hopping height equal to x_c, i.e.

$$KE_c = \frac{I - \boldsymbol{f}}{q} \cdot \frac{n_f \boldsymbol{a}_g E}{r_t} \qquad\qquad (3.30)$$

therefore we have

105

$$Z_{sh} = \left(\frac{2}{\sqrt{p}} \frac{KE_c}{kT_t} e^{-KE_c/kT_t} + 1 - erf\left(\sqrt{\frac{KE_c}{kT_t}} \right) \right) \frac{3cp\,P_g}{n_f\,a_g\,E^2} \cdot r_t^2 e^{a_g E^2/2kT_t} \cdot \bar{u}_d \qquad (3.31)$$

It should be pointed out that in deriving eqn.(3.28) and (3.29), the diffusion flux, due to the non-uniform gas distribution along the shank, has been neglected. In the supply limited regime, however, the diffusion flux—denoted as Z_{di}—is much smaller than the drift flux Z_{dr}. Note that $Z_{di} \propto dn/dx$ and $Z_{dr} \propto n$, if no ionization occurred, we would have $n = n_g \exp(\alpha_g E^2/2kT_t)$ and $Z_{di} = Z_{dr}$. However, as mentioned before, in the supply-limited regime, due to strong ionization, the gas density in the ionization zone reduces so much that it becomes comparable to that in the remote area[75]. On the other hand, the gas density beyond the ionization zone is not affected as much due to the strong dependence of ionization rate on the field. Consequently, we expect that the real drift flux Z_{dr} does not change much compared to the case without ionization. But the diffusion flux becomes

$$Z_{di} \propto \frac{dn}{dx} \approx \frac{n_g \exp\left(\dfrac{a_g E^2}{2kT_t} \right) - n_g}{r_t} \qquad (3.32)$$

And therefore

$$\frac{Z_{di}}{Z_{dr}} \approx \frac{Z_{di}}{\tilde{Z}_{di}} \approx \frac{\exp\left(\dfrac{a_g E^2}{2kT_t} \right) - 1}{\exp\left(\dfrac{a_g E_a^2}{2kT_t} \right) - \exp\left(\dfrac{a_g E^2}{2kT_t} \right)} = \frac{1 - \exp\left(-\dfrac{a_g E^2}{2kT_t} \right)}{\exp\left(a_g \dfrac{E_a^2 - E^2}{2kT_t} \right) - 1} \approx \exp\left(a_g \dfrac{E^2 - E_a^2}{2kT_t} \right) \;(3.33)$$

For He gas, taking $E_a = 400$MV/cm, $E = 300$V/cm and $T_t = 100$K, we find $\dfrac{Z_{di}}{Z_{dr}} \approx 0.003$.

3.2.2 Emission Current of GFIS

At very low fields, the gas distribution in the ionization zone is approximately in equilibrium. By taking into account the variation of field in the ionization zone, the emission current is given by

$$i = 2pq\frac{P_g}{kT_t}n\Delta x_c \int_0^{q_c} r(q)^2 D(x_c, q)\exp\left(\frac{a_g E(q)^2}{2kT_t}\right)\sin(q)dq \tag{3.34}$$

where $\Delta x_c \approx 0.5\text{Å}$ is the half width of the ionization zone at low fields, ν is the orbital frequency of the tunneling electron and $D(x_c)$ is the penetration probability at the critical distance x_c. The integration is done over the emitter surface up to an appropriate angle θ_c where ionization becomes negligible.

At high fields, we need to consider the total gas supply Z into the ionization zone, which consists of two parts, one from the molecules directly attracted from space and the other from the flux along the shank, i.e.

$$Z = Z_{sp} + Z_{sh} \tag{3.35}$$

where $Z_{sp} = Y_{sp} \cdot A_{ion}$, A_{ion} is the area of the ionization zone and Y_{sp} is given by (3.2).

The total emission current may then be obtained following Gomer's procedure[94]

$$i = \frac{qk_i}{k_d + k_i}Z = \frac{qk_i}{k_d + k_i}(Z_{sp} + Z_{sh}) \tag{3.36}$$

where k_d and k_i are respectively the diffusion and ionization rate constants in the ionization zone, given by

$$k_d = \frac{4\sqrt{2}(kT_t)^{3/2}}{n_f m^{1/2} r_t \boldsymbol{a}_g E_a^{\ 2}}$$

$$k_i \approx \frac{n_f \boldsymbol{a}_g E_a^{\ 5/2} \Delta x_c^{\ 3/2} q^{1/2}}{kT_t r_t (I - \boldsymbol{f})^{1/2}} \boldsymbol{n} D(x_c) \exp\left(-\frac{n_f \boldsymbol{a}_g E_a}{r_t kT_t} \cdot \frac{I - \boldsymbol{f}}{q}\right)$$

(3.37)

Eqn.(3.36) is only valid when the ratio k_i / (k_i+k_d), which represents the ionization probability, is close to unity since we have neglected gas diffusion. For the other extreme case where the ionization probability $\ll$ 1, eqn.(3.34) should be used.

Figure 3-4 plots the ionization probability k_i / (k_i+k_d) vs. emitter apex field at different tip temperatures. It is seen that the curve shifts toward low field region as the tip temperature decreases, implying that the GFIS enters supply limited regime at lower fields when T_t is reduced.
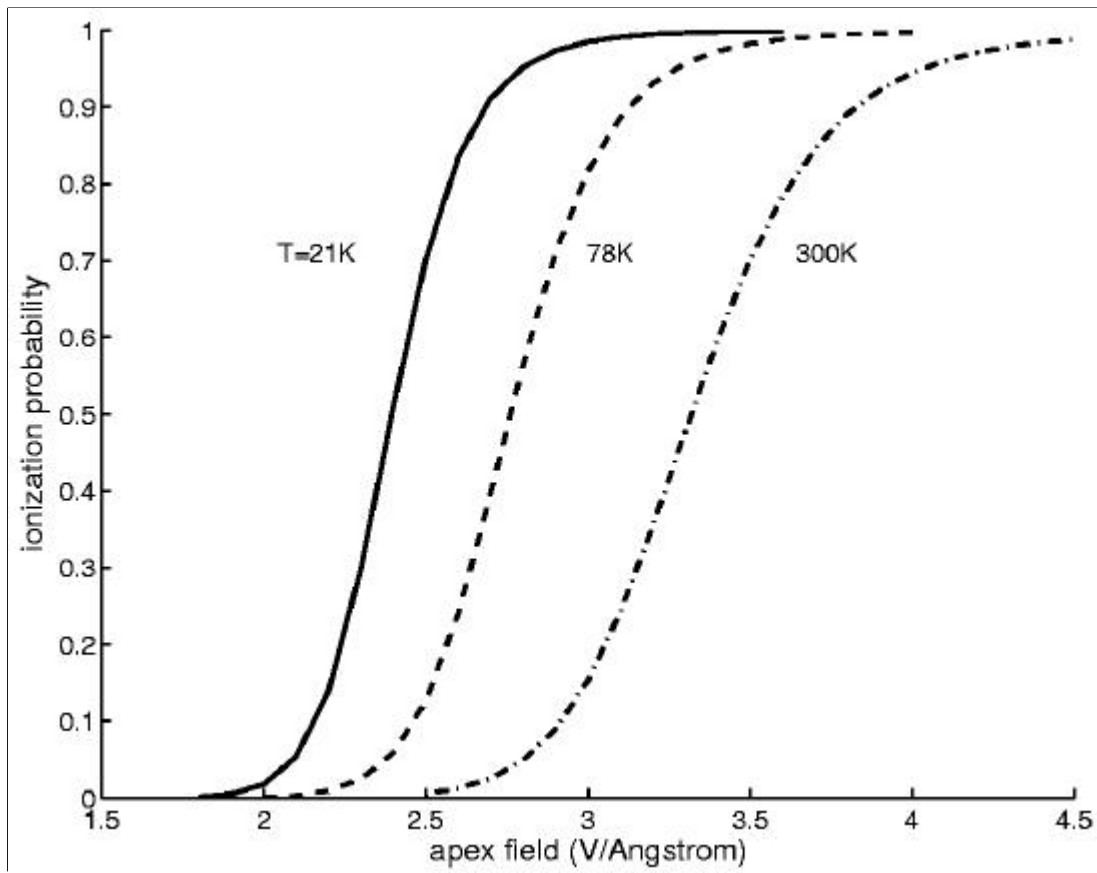
Figure 3-4 Ionization probability $\dfrac{k_i}{k_i+k_d}$ vs. emitter apex field at different tip temperature

(He gas, W tip, $r_a = 0.1\mu m$)

3.3   Result

The calculation is done for He gas and W emitter. The following parameters are chosen: $P_g = 10^{-3}$torr, $r_a = 0.1\mu$m. Moreover, set n = 0.16 ($\theta_0 = 174.8°$) and $\gamma = 2.5$ in the SOC model, and n_f is found to be 1.74.

Figure 3-5 plots log(i) vs. log(E_a) of GFIS at 78°K. The ionization zone boundary is chosen where the ionization probability is 0.5, corresponding to E = 2.8V/Å. The slope in the field-limited regime is about 30, and in the high field region it is about 4, which can be compared with the measured value 3–5[89].

Figure 3-6 shows the I-V curve at 300°K. Besides the fact that the total current drops dramatically compared with 78°K, we can also see that there is no well-defined transition region in this case, which agrees with the results obtained by Tsong and Müller[91].

The ratio i(78°K)/i(300°K) is plotted in Figure 6, which shows that both the ratio and the slope (absolute value) of the curve decrease as the field increases in the region near the best imaging field, and that at 78°K the emission current is 1–2 order of magnitudes higher than at 300°K.

Figure 3-8 shows the comparison of the calculated I-V characteristic for H_2–Ir GFIS ($T_t = 300°$K, $P_g = 10^{-3}$torr and $r_a = 0.1\mu$m) with the experimental data by Orloff and Swanson[95]. The experimental data has been recalibrated assuming that the total current is emitted within a half aperture angle of 20°–30°, corresponding to a solid angle ~ 0.5sr; the experimental data were taken using a detector with a 9msr solid angle. The agreement is fairly satisfactory.
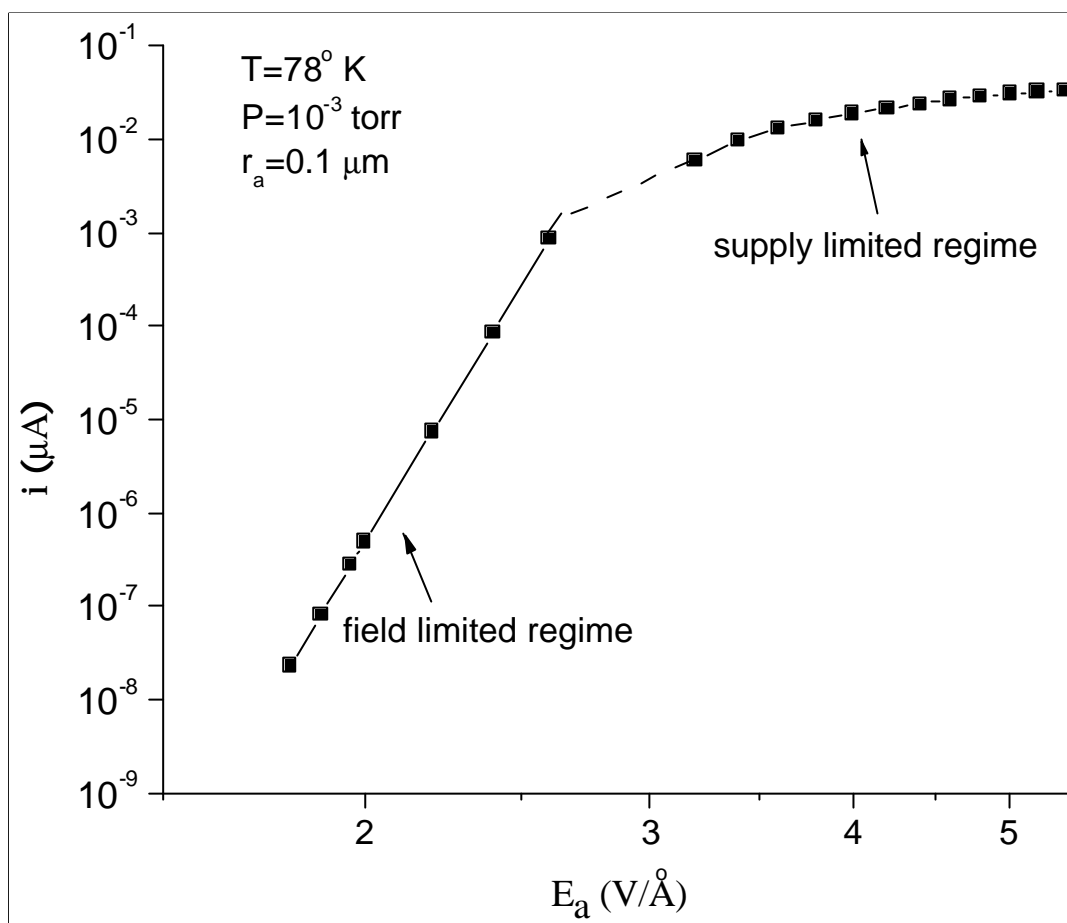
Figure 3-5 I-V characteristic of GFIS at 78°K
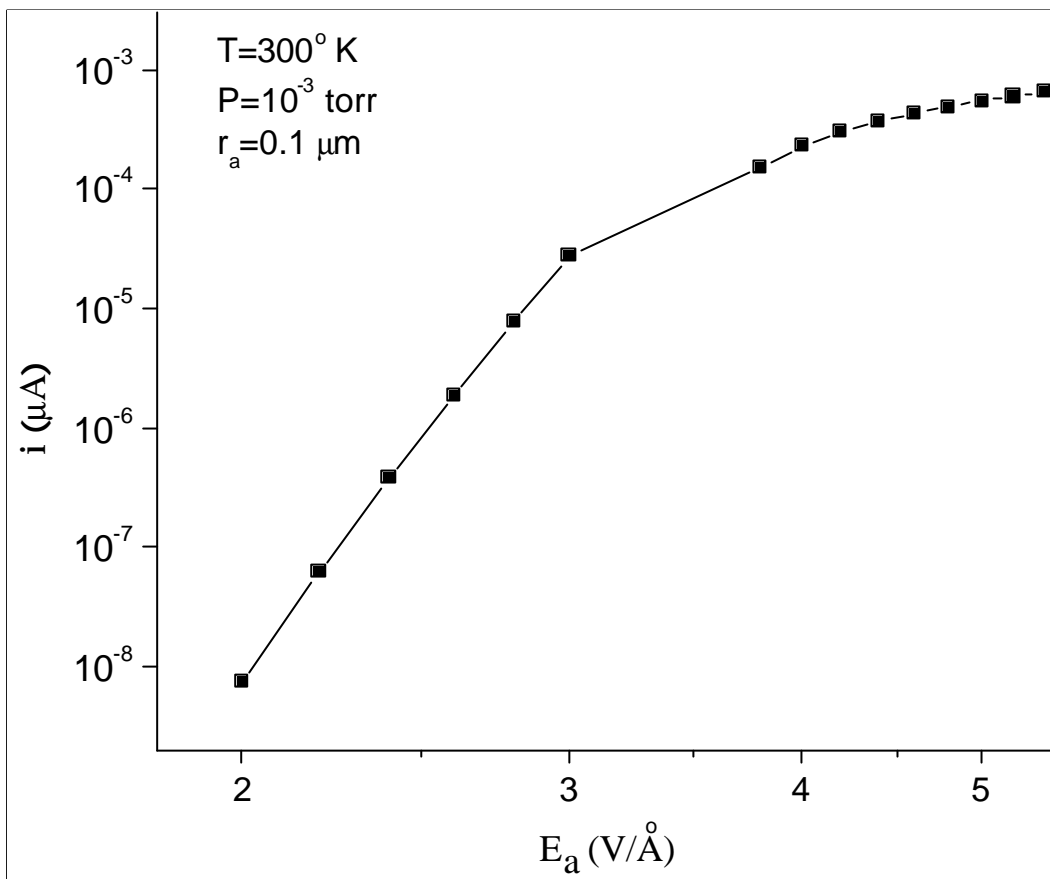
Figure 3-6 I-V characteristic at 300°K
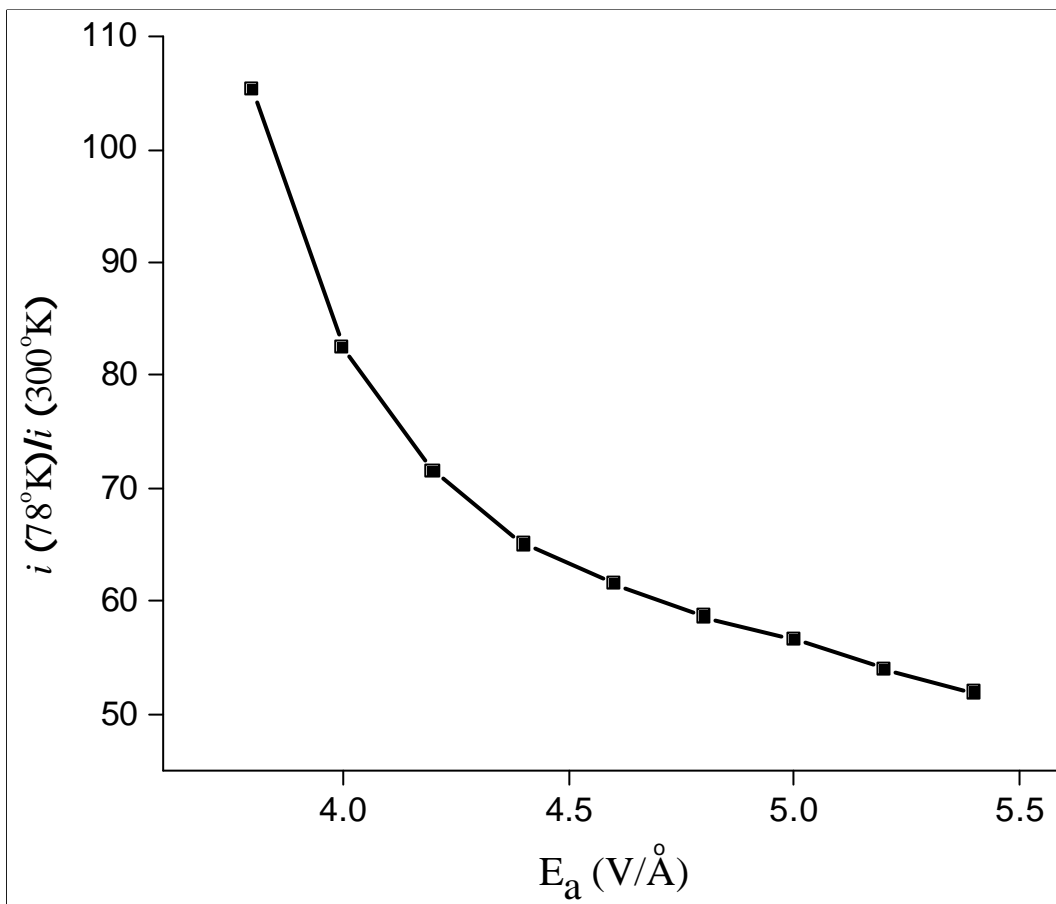
Figure 3-7 Ratio of currents at 78°K and 300°K
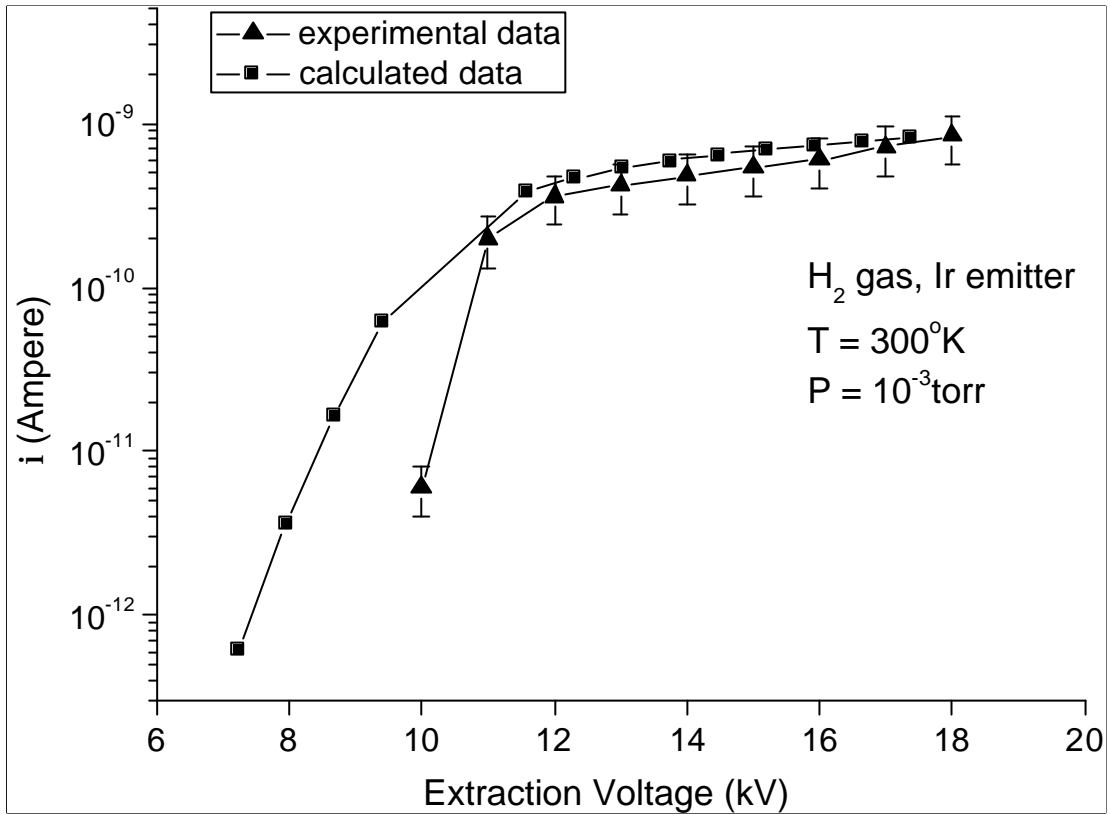
Figure 3-8 Comparison of the experimental[95] and calculated I-V characteristic of H_2–Ir GFIS at 300°K (r_a is taken to be 0.1μm). Experimental data were scaled to take into account the small solid angle of the detector (see text).

Chapter 4   Conclusion

This thesis studies the optical properties and current emission process in the diode region of GFIS.

The Gaussian optical properties are derived by solving the paraxial ray equation and the spherical and chromatic aberrations are evaluated through two alternative integrals which are appropriate for the case where the aperture is located in a field-present region (such as the diode region). It is found that the existence of critical distance plays an important role in determining the aberration coefficients, in contrast with the case of field emission cathode.

The virtual source size is derived in two alternative ways. The first one is by the well-known algorithm of addition in quadrature, which is shown to be a well approximation at small apertures where higher order aberrations can be neglected. Alternatively, the source size can be evaluated through direct ray tracing, which is applicable to all but extremely small apertures where the diffraction effect sets in. The result shows that the source size is largely determined by the emitter radius and is virtually independent of the electric field and detailed emitter geometry. In addition, as the tip temperature decreases, the source size increases due to the fact that the GFIS is dominated by the spherical aberration.

The supply mechanism is most important in understanding the current emission process. In GFIS, the gas material can be supplied in two ways, either directly from space or along the emitter shank. And the latter one dominates at high fields. This thesis presents a relatively simple model based on the gas drifting flux along the shank, irrespective of the detailed gas-surface interactions. Although a complete solution from

the first principle is absent, it is shown that the resulting I-V characteristic of He gas agrees reasonably well with the experiment.

This thesis has dealt primarily with the physics of the gas field ionization source. We believe that this source should be re-considered for FIB applications and that the work done here will be useful for that purpose. From the system designer's point of view, several factors are worth noting. The emission current depends in a complex way on the emitter area, electric field and temperature. One must note that as the electric field increases, the energy spread goes up (Figure 2-11). Moreover, charge-exchange reactions will set in and result in a longer beam tail at high field. Also, for gas species such as H_2, the energy spread is much larger than that of singly charged ions due to the mixture of singly and doubly charged states. This means there must be a limit to the electric field and therefore to the current for a given emitter radius and temperature.

As shown in Figure 3-7, the current decreases dramatically as the tip temperature increases, so that the GFIS should be operated at low, preferably cryogenic temperatures. This implies that the designer must worry about how to cool the emitter and gas to cryogenic temperature without introducing vibration. Vibration is important because with a "point source" emitter the de-magnification is usually not much (~ 0.5×), so vibration will be seen even at the few nanometer or few tens of nanometer levels.

The emission current increases approximately linearly with the emitter area (eqn. (3.34) and (3.36)) for given electric field and tip temperature. The source aberrations and virtual source size, however, also increase with the emitter radius as shown in Figure 2-8 (for He GFIS at beam-limiting aperture of 0.2msr and T = 78°K, the source size goes from 0.5nm to 4nm as the emitter radius increases from 0.1μm to 0.5μm). Besides, larger

116

emitter radius requires larger extraction voltage for a given apex field, so that there exists a trade-off between the available current vs. spot size of the ion beam under certain vacuum conditions.

References

1 J.R.Oppenheimer, *Phys. Rev.* 31, 67 (1928)

2 E.W.Mü ller, *Z. Physik* 131, 136 (1951)

3 E.W.Mü ller and K.Bahadur, *Phys. Rev.* 102, 624 (1956)

4 E.W.Mü ller, *J. Appl. Phys.* 28, 1 (1957)

5 R.Gomer, *J.Chem.Phys.* 20, 1772 (1952)

6 W.J.Tegart, *The Electrolytic and Chemical Polishing of Metals* (Pergamon Press, Oxford, 1959)

7 E.W.Mü ller and R.D.Young, *J.Appl.Phys.* 32, 2425 (1961)

8 W.R.Graham and G.Ehrlich, *Surf.Sci.* 45, 530 (1974)

9 R.Liboff, *Introductory Quantum Mechanics* (Pearson Education, 2002)

10 R.Levi-Setti, *Scanning Electron Microscopy*, 125 (1974)

11 J.Orloff and L.W.Swanson, *J.Vac.Sci.Tech.* 12, 1209 (1975)

12 J.Orloff and L.W.Swanson, *SEM*/1977, Vol.1, 57 (1977)

13 J.Orloff and L.W. Swanson, *J.Vac.Sci.Technol.* 15(3), 845 (1978)

14 J.Orloff and L.W.Swanson, *J.Appl.Phys.* 50, 6026 (1979)

15 T.T.Tsong and E.W.Mü ller, *J.Chem.Phys.* 41, 3279 (1964)

16 J.Orloff and L.W.Swanson, *J.Appl.Phys.* 50, 6026 (1979)

17 V.E.Krohn and G.R.Ringo, *Appl.Phys.Lett.* 27, 479 (1975)

18 R.L.Seliger, J.W.Ward, V.Wang and R.L.Kubena, *Appl.Phys.Lett.* 34, 310 (1979)

19 M.Bozack, L.W.Swanson and J.Orloff, *SEM*/1985, Vol.IV, 1339 (1985)

20 G.I.Taylor, *Proc.of the Roy.Soc.A* 280, 383 (1964)

21 J.Orloff, M.Utlaut and L.Swanson, *High Resolution Focused Ion Beams: FIB and Its Applications* (Kluwer Academic/Plenum Publishers, New York, 2003)

22 W.Driesel, Ch.Dietzsch and R.Mü hle, *J.Vac.Sci.Tech.B* 14, 3367 (1996)

23 G.BenAssayag, P.Sudraud and B.Jouffrey, *Ultramicroscopy* 16, 1 (1985)

24 W.Driesel and Ch.Dietzsch, *J.Vac.Sci.Tech.B* 14, 3376 (1996)

25 G.H.Jansen, *Coulomb Interactions in Particle Beams, Adv.Electron.Electron Phys., Suppl.* 21 (Academic Press, New York, 1990)

26 R.Gomer, *Appl.Phys.* 19, 365 (1979)

27 P.D.Prewett, G.L.R.Mair and S.P.Thompson, *J.Appl.Phys.D* 15, 1339 (1982)

28 N.K.Kang and L.W.Swanson, *Appl.Phys.A* 30, 95 (1983)

29 D.R.Kingham and L.W.Swanson, *Appl.Phys.A* 34, 123 (1984)

30 R.Gomer, *J.Chem.Phys.* 31, 341 (1959)

31 R.Gomer and L.W.Swanson, *J.Chem.Phys.* 38, 1613 (1963)

32 D.R.Kingham, *Surf.Sci.* 116, 273 (1982)

33 L.W.Swanson and D.R.Kingham, *Appl.Phys.A* 41, 223 (1986)

34 P.D.Prewett, L.Gowland, K.L.Aitken and C.Mahony, *Thin Solid Films* 80, 117 (1981)

35 W.M.Jr.Clark, R.L.Seliger, M.W.Utlaut, A.E.Bell, L.W.Swanson, G.A.Schwind and J.B.Jergenson, *J.Vac.Sci.Tech.B* 5, 197 (1987)

36 G.L.R.Mair, D.C.Grindrod, M.S.Mousa and R.V.Latham, *J.Phys.D: Appl.Phys.* 16, L209 (1983)

37 W.Knauer, *Optik* 59, 335 (1981)

38 J.W.Ward, R.L.Kubena and M.W.Utlaut, *J.Vac.Sci.Technol.B* 6, 2090 (1988)

39 L.W.Swanson and A.E.Bell, in *The Physics and Technology of Ion Source* (John Wiley & Sons, Inc. 1989), ed. I. G.Brown

40 L.W.Swanson, G.A.Schwind, A.E.Bell and J.E.Brady, *J.Vac.Sci.Tech.* 16, 1864 (1979)

41 P.Sudraud, J.Orloff and G.BenAssayag, *Jour.de Physique*, Coll C7, no.11, 47 C7-381 (1986)

42 V.Wang, J.W.Ward and R.L.Seliger, *J.Vac.Sci.Tech.* 19, 1158 (1981)

43 R.Levi-Setti, G.Grow and Y.L.Yang, *Scanning Electron Microscopy*, 3, 535 (1985)

44 R.Levi-Setti, J.M.Chabala and Y.L.Yang, *Ultramicroscopy*, 24, 97 (1988)

45 Application Notes A100, *Cambridge Mass Spectrometry*, Cambridge, A105 (1990)

46 P.J.Heard, P.D.Prewett and R.A.Lawes, *Microelectron.Eng.* 6, 597 (1987)

47 B.W.Ward, M.Ward, D.Edwards and N.P.Economou, *J.Vac.Sci.Technol.B* 6, 2100 (1988)

48 J.Melngailis, *J.Vac.Sci.Technol.B* 5, 469 (1987)

49 P.J.Heard and P.D.Prewett, in *Focused Ion Beams from Liquid Metal Ion Sources* (Research Studies Press, Taunton, U.K., 1991), ed. P.D.Prewett and G.L.R.Mair

50 Y.L.Lee and R.L.Kubena, *Appl.Phys.Lett.* 48, 688 (1986)

51 G.R.Hanson and B.M.Siegel, *J.Vac.Sci.Tech.* 16, 1875 (1979)

52 G.R.Hanson and B.M.Siegel, *J.Vac.Sci.Tech.* 19, 1176 (1981)

53 K.Jousten, K.Böhringer and S.Kalbitzer, *Appl.Phys.B* 46, 313 (1988)

54 Th.Miller, A.Knoblauch, Ch.Wilbertz and S.Kalbitzer, *Appl.Phys.A* 61, 99 (1995)

55 R.Börret, K.Jousten, K.Böhringer and S.Kalbitzer, *J.Phys.D: Appl. Phys.* 21, 1835 (1988)

56 S.Kalbitzer and A.Knoblauch, *Appl.Phys.A* 78, 269 (2004)

57 J.Orloff, *SPIE* 2522, 412 (1995)

58 J.Orloff, *J.Vac.Sci.Tech.B* 14, 3759 (1996)

59 M.Utlaut, in *Handbook of Charged Particle Optics* (CRC press, New York, 1997), ed. J.Orloff

60 P.Sigmund, *Phys.Rev.* 184, 383 (1969)

61 Y.Yamamura, *At.Dat.&Nuc.Dat.Tab.* 62, 149 (1996)

62 P.Sigmund, in Inelastic Ion-Surface Collisions (Academic Press, New York, 1977), ed. N.H.Tolk, J.C.Tully, W.Heiland and C.W.White

63 T.B.Johansson, R.Akselsson and S.A.E.Johansson, *Nucl.Instrum.Methods* 84, 141 (1970)

64 G.W.Grime and F.Watt, *Beam Optics of Quadrupole Probe-Forming Systems* (Adam Hilger Ltd, Bristol, 1984)

65 S.A.E.Johansson and T.B.Johansson, *Nucl.Instrum.Methods* 137, 473 (1976)

66 J.F.Mulson, Master's Thesis, The Pennsylvania State University (1961)

67 K.D.Rendulic and Z.Knor, *Surf.Sci.* 7, 205 (1967)

68 D.F.Barofsky and E.W.Mü ller, *Surf.Sci.* 10, 177 (1968)

69 P.C.Bettler and F.M.Charbonnier, *Phys.Rev.* 119, 85 (1960)

70 P.W.Hawkes and E.Kasper, *Principles of Electron Optics, Vol.1* (Academic Press, London, 1989)

71 B.Lencová and M.Lenc, *Optik*, 97(3), 121 (1994)

72 J.C.Wiesner and T.E.Everhart, *J.Appl.Phys.* 44, 2140 (1973)

73 L.Reimer, *Scanning Electron Microscopy, Springer Series in Optical Sciences*, *Vol.*45 (Springer Verlag, 1985)

74 E.W.Mü ller and T.T.Tsong, *Field Ion Microscopy: Principles and Applications* (American Elsevier Publishing Company, Inc., New York 1969)

75 H.A.M.Van Eekelen, Surf.Sci. 21, 21 (1970)

76 H.Iwasaki and S.Nakamura, Surf.Sci. 52, 588 (1975)

77 M.Born and E.Wolf, *Principles of Optics* (Pergamon Press, 1980)

78 T.E.Everhart, *J.Appl.Phys.* 38, 4944 (1967)

79 J.W.Ward and R.L.Seliger, J.Vac.Sci.Technol. 19, 1082 (1981)

80 B.Lencová, *Nucl.Instrum.Methods Phys.Res., A363* , 190, 1995

81 X.Zhu and E.Munro, J.Microsc. 179, 170 (1995)

82 N.K.Kang, J.Orloff, L.W.Swanson and D.Tuggle, *J.Vac.Sci.Technol.* 19, 1077 (1981)

83 W.R.Smythe, *Static and Dynamic Electricity* (McGraw-Hill, New York, 1950) p.208

84 L.W.Swanson and L.C.Crouser, *J.Appl.Phys.* 40, 4741 (1969)

85 K.Schwarzschild, *Gesell.Wiss.Goettingen, Nachr.Math.-Phys. Klasse* 3, 126 (1903)

86 O.Scherzer, *Z.Physik* 101, 593 (1936)

87 J.Stoer and R.Bulirsch, *Introduction to Numerical Analysis 2th ed.* (Springer-Verlag, New York 1993), Trans. by R.Bartels, W.Gautschi and C.Witzgall

88 V.K.Zworykin, G.A.Morton, E.G.Ramberg, J.Hillier and A.W.Vance, *Electron Optics And The Electron Microscope* (John Wiley & Sons, Inc., New York 1945)

89 M.J.Southon and D.G.Brandon, *Phil. Mag*. 8, 579 (1963)

90 M.J.Southon, Ph.D. Thesis (University of Cambridge, 1963)

91 T.T.Tsong and E.W.Mü ller, *J.Appl.Phys.* 37, 3065 (1966)

92 J.Orloff and L.W.Swanson, *J.Appl.Phys.* 50(9), 6026 (1979)

93 B. Halpern and R. Gomer, *J.Chem.Phys*. 51, 5709 (1969)

94 R.Gomer, *Field Emission and Field Ionization* (American Institute of Physics, New York 1993)

95 J.H.Orloff and L.W.Swanson, *J.Vac.Sci.Technol.* 12 (6), 1209(1975)